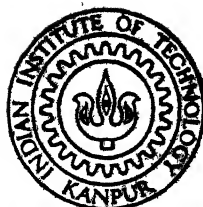


# LASER OPTOGALVANIC SPECTROSCOPY OF Sc, Nb and Re FINE AND HYPERFINE STRUCTURE STUDIES

by

RANJIT SINGH

PHY TH  
1990 PHY/1990/P  
D SI 642



PHI  
LAS

DEPARTMENT OF PHYSICS

INDIAN INSTITUTE OF TECHNOLOGY KANPUR

February, 1990

**LASER OPTOGALVANIC SPECTROSCOPY OF Sc, Nb and Re  
FINE AND HYPERFINE STRUCTURE STUDIES**

*A Thesis Submitted  
in Partial Fulfilment of the Requirements  
for the Degree of*

**DOCTOR OF PHILOSOPHY**

*by*

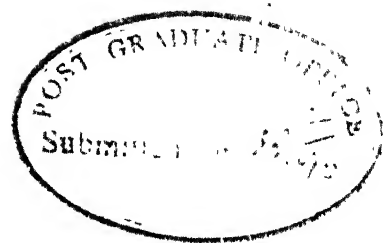
**RANJIT SINGH**

*to the*

**DEPARTMENT OF PHYSICS**

**INDIAN INSTITUTE OF TECHNOLOGY KANPUR**

*February, 1990*



## CERTIFICATE

This is to certify that the work contained in the thesis entitled, "Laser Optogalvanic Spectroscopy of Sc, Nb and Re : Fine and Hyperfine Structure Studies" has been carried out by Ranjit Singh under the supervision of Prof. G.N. Rao and me and the same has not been submitted elsewhere for a degree.

Feb 1990

*RK Thareja*  
(R.K. Thareja)

Thesis Supervisor

840511

PHY-1990-D-SIN-LAS

23 DEC 1991

CENTRAL LIBRARY

Acc. No. 112548



## SYNOPSIS

LASER OPTOGALVANIC SPECTROSCOPY OF Sc, Nb AND Re  
FINE AND HYPERFINE STRUCTURE STUDIES

Submitted in partial fulfillment of the requirements  
for the degree of

Doctor Of Philosophy

by

Ranjit Singh

to the

Department of Physics  
Indian Institute of Technology  
KANPUR — 208016 (INDIA)

In this thesis we report studies on fine and hyperfine structure of scandium, niobium and rhenium atoms, using laser optogalvanic spectroscopy. Sputtering technique in a hollow cathode discharge is employed for the production of free atoms.

Even though lot of work has been done on the investigation of hyperfine structure of transition elements, still very little information is available about the high lying metastable states and higher odd parity states. The aim of this work is to identify and study the hyperfine structure of transitions originating from these states of scandium, niobium and rhenium. These results along with the already available information on hyperfine structure of other states of these elements will provide a broadened horizon for further theoretical

analysis using effective operator formalism, which will help in understanding these complex atoms.

Chapter I introduces the subject and briefly describes the objective of the thesis. Chapter II, briefly describes the theory of fine and hyperfine structure of free atoms. Effective Operator formalism for the analysis of hyperfine structure is described, emphasising its use to get information about the electronic wave functions. Theory of isotope shift is also outlined.

Chapter III describes the experimental details. Laser optogalvanic spectroscopy, the technique used in this thesis, is discussed. To check the experimental technique used for all the fine structure investigations, a broad band optogalvanic spectrum of vanadium was recorded. Identified vanadium transitions, their level assignments and optogalvanic intensities are reported. Doppler limited high resolution experimental setup and the analysis procedure were tested using known transitions of lanthanum and niobium. Results of these test studies are compared with the known, already published work.

Chapter IV gives the results of the experimental studies performed on scandium. The optogalvanic spectrum of scandium is recorded in the range 570 – 635 nm and seventeen fine structure transitions belonging to the first spectrum of scandium are identified. Most of these transitions connect the high lying metastable states in the configuration  $3d^24s$  with the higher odd parity states in the configuration  $3d^24p$ . The hyperfine structure of some of these transitions is reported.

Chapter V gives the results of studies on fine and hyperfine structure of niobium. Thirty two transitions of Nb I are identified from the recorded optogalvanic spectrum in the R6G dye range, 570 – 635 nm. Hyperfine structure of many of these transitions is studied. Our results are compared with the previous data, wherever possible, and the new results are discussed.

Results of studies on rhenium are presented in chapter VI. Rhenium has two natural isotopes,  $^{185}\text{Re}$  and  $^{187}\text{Re}$ . Therefore, from the recorded spectra, we also get isotope shifts between these two isotopes along with the hyperfine structure. High resolution spectra of six transition are reported. Isotope shifts in all these transitions, between  $^{185}\text{Re}$  and  $^{187}\text{Re}$ , are reported. Hyperfine coupling constants, A and B, for all the levels of both the isotopes involved in these transitions are reported.

In conclusion, fine structure spectra of scandium and niobium recorded, in the range 570 – 635 nm, using laser optogalvanic spectroscopy, is analyzed and identified lines are reported along with their level assignments and the optogalvanic intensities. Hyperfine structure studies on a large number of transitions of Sc, Nb and Re are performed and resultant A and B parameters for all the levels involved are reported. Isotope shifts between  $^{185}\text{Re}$  and  $^{187}\text{Re}$ , in six transitions, are reported. These results along with the already available results from the literature will provide a broad base for the further theoretical analysis to get more information about the electronic states of these atoms.

DEDICATED  
TO  
MY LATE MOTHER

## ACKNOWLEDGEMENT

Herewith I would like to express my deep gratitude to many people who gave me their support during the years I worked on this thesis.

I am geateful to Prof. G.N. Rao for interducing me to the field and giving the opportunity to work with the state of the art equipment in the lab. I express my gratitute to Dr. R.K. Thareja whose untiring efforts and guidance helped me in completing this work. His confidence and enthusiasm provided a precious support. Working with him will be a pleasant memory in the years to come.

I have derived great pleasure in working with my lab seniors Rama and Govind. I learnt a lot not only about experimentation but also about the general fields of lasers and spectroscopy from them. My colleages in the lab, Dr. Pramila, Reddy, Ashish, Krishna and Abhay deserve my appriciation for their help in my work.

I must thank Dr. B.P. Singh and Dr. Bansi Lal for fruitful discussions and general help. A special word of thanks goes to my fellow 'LIGHT TALKERS' for helping and encourging my forays into the suble art of scientific communication.

Amit, Alok, Divaker, Prasad, Ravi, Razee, Sanjay and Srini helped in my work and provide the necessary social stimulus which made many happy moments. S. Jagir Singh and family, Ranjit, Beena, Usha and Little Minnie have given me many pleasant memories. I am thankful to Ajay, Arika, Pushpa, Rita, Rekha, Satharath, Bipin and Subba Rao.

A special word of thanks are to Mr. Kuldeep Singh for his technical and general help. I acknowledge the help given by the staff of Physics and CELT offices, CELT workshop, and Glass Blowing shop.

No words can truly express my feeling of gratitude to my father and my late mother for encouraging me to move up in life. I thank my wife Ranjit for her patience and understanding.

Finally I thank one and all who have helped me directly or indirectly during my stay at IIT Kanpur.

(Ranjit Singh)

## CONTENTS

	Page
List of Tables	ix
List of Figures	x
<b>1 INTRODUCTION</b>	<b>1</b>
<b>2 THEORY OF HYPERFINE STRUCTURE AND ISOTOPE SHIFT</b>	<b>6</b>
2.1 Introduction	6
2.2 Fine and Hyperfine Structure	7
2.3 Isotope Shift	17
<b>3 EXPERIMENTAL DETAILS</b>	<b>21</b>
3.1 Introduction	21
3.2 Optogalvanic Spectroscopy	22
3.3 Production of Sputtered Vapours	26
3.4 Experimental Details	27
3.5 Test Studies	38
3.6 Data Analysis	43
<b>4 FINE AND HYPERFINE STRUCTURE OF SCANDIUM</b>	<b>47</b>
4.1 Introduction	47
4.2 Experimental	48
4.3 Results and Discussion	49
<b>5 FINE AND HYPERFINE STRUCTURE OF NIOBIUM</b>	<b>67</b>
5.1 Introduction	67
5.2 Experimental	68
5.3 Results and Discussion	72
<b>6 HYPERFINE STRUCTURE AND ISOTOPE SHIFT OF RHENIUM</b>	<b>100</b>
6.1 Introduction	100
6.2 Experimental	101
6.3 Results and Discussion	103
<b>CONCLUSIONS</b>	<b>118</b>
<b>REFERENCES</b>	<b>120</b>

## CONTENTS

	Page
List of Tables	ix
List of Figures	x
<b>1 INTRODUCTION</b>	<b>1</b>
<b>2 THEORY OF HYPERFINE STRUCTURE AND ISOTOPE SHIFT</b>	<b>6</b>
2.1 Introduction	6
2.2 Fine and Hyperfine Structure	7
2.3 Isotope Shift	17
<b>3 EXPERIMENTAL DETAILS</b>	<b>21</b>
3.1 Introduction	21
3.2 Optogalvanic Spectroscopy	22
3.3 Production of Sputtered Vapours	26
3.4 Experimental Details	27
3.5 Test Studies	38
3.6 Data Analysis	43
<b>4 FINE AND HYPERFINE STRUCTURE OF SCANDIUM</b>	<b>47</b>
4.1 Introduction	47
4.2 Experimental	48
4.3 Results and Discussion	49
<b>5 FINE AND HYPERFINE STRUCTURE OF NIOBIUM</b>	<b>67</b>
5.1 Introduction	67
5.2 Experimental	68
5.3 Results and Discussion	72
<b>6 HYPERFINE STRUCTURE AND ISOTOPE SHIFT OF RHENIUM</b>	<b>100</b>
6.1 Introduction	100
6.2 Experimental	101
6.3 Results and Discussion	103
<b>CONCLUSIONS</b>	<b>118</b>
<b>REFERENCES</b>	<b>120</b>



## LIST OF TABLES

- I Fine structure transitions of vanadium
- II Hfs constants of lanthanum and niobium
- III Fine structure transitions of scandium
- IV Hfs constants of scandium
- V Fine structure transitions of niobium
- VI Hfs constants of niobium
- VII Fine structure transitions of rhenium and the isotope shift.
- VIII Hfs constants of  $^{185}\text{Re}$
- IX Hfs constants of  $^{187}\text{Re}$

## LIST OF FIGURES

- Fig. 1. Experimental setup used for fine structure studies.
- Fig. 2. Schematic of the standing wave dye laser (Spectra Physics 375).
- Fig. 3. Schematic of the ring dye laser (Spectra Physics 380D).
- Fig. 4. Transmission curves of the intracavity devices;
- Fig. 5. Transmission curves of the reference interferometers.
- Fig. 6. Schematic of the wavemeter (Burleigh WA-20).
- Fig. 7. Experimental setup used for recording hfs spectra using laser optogalvanic spectroscopy (LOGS).
- Fig. 8. Fine structure spectrum vanadium and neon.
- Fig. 9. Hyperfine structure of La transition at 582.19 nm.
- Fig. 10. Hyperfine structure of niobium transition at 586.64 nm.
- Fig. 11. Fine structure spectrum of scandium and neon.
- Fig. 12. Energy level diagram of scandium.
- Fig. 13. Hyperfine structure of scandium transition at 571.20 nm.
- Fig. 14. Hyperfine structure of scandium transition at 598.84 nm.
- Fig. 15. Hyperfine structure of scandium transition at 602.62 nm.
- Fig. 16. Hyperfine structure of scandium transition at 614.62 nm.
- Fig. 17. Hyperfine structure of scandium transition at 602.15 nm.
- Fig. 18. Fine structure spectrum of niobium and neon.
- Fig. 19. Energy level diagram of niobium.
- Fig. 20. Hyperfine structure of niobium transition at 566.47 nm.
- Fig. 21. Hyperfine structure of niobium transition at 569.79 nm.
- Fig. 22. Hyperfine structure of niobium transition at 570.62 nm.
- Fig. 23. Hyperfine structure of niobium transition at 570.65 nm.
- Fig. 24. Hyperfine structure of niobium transition at 576.03 nm.
- Fig. 25. Hyperfine structure of niobium transition at 577.61 nm.
- Fig. 26. Hyperfine structure of niobium transition at 578.75 nm.

- Fig. 27. Hyperfine structure of niobium transition at 583.86 nm.  
Fig. 28. Hyperfine structure of niobium transition at 584.25 nm.  
Fig. 29. Hyperfine structure of niobium transition at 587.60 nm.  
Fig. 30. Energy level diagram of rhenium.  
Fig. 31. Hyperfine structure of rhenium transition at 566.75 nm.  
Fig. 32. Hyperfine structure of rhenium transition at 583.40 nm.  
Fig. 33. Hyperfine structure of rhenium transition at 5943 nm.  
Fig. 34. Hyperfine structure of rhenium transition at 577.60 nm.  
Fig. 35. Hyperfine structure of rhenium transition at 614.60 nm.  
Fig. 36. Generated spectrum of rhenium transition at 583.43 nm.

## CHAPTER I

### INTRODUCTION

Atomic spectroscopy has played an important role in understanding the electronic structure of atoms and provided a base for the development of basic quantum mechanics. Optical spectroscopy has always been an important tool for studying atomic structure. The discovery of tunable dye lasers created a revolution in the field of atomic spectroscopy by improving the resolution and sensitivity of detection by several orders of magnitude [1-6]. The narrow line width, tunability, high intensity, coherence, polarization and low divergence are few of the features of lasers which make them an ideal source of light for high resolution optical spectroscopy [7].

Hyperfine structure is known for quite some time now [8-10]. In past hyperfine structure (hfs) was studied to get the nuclear information like, nuclear moments etc. But now a days since nuclear information is available with high accuracy from the nuclear techniques like charged particle scattering [11], emphasis has shifted to get the electronic information from the study of hyperfine structure [12-13]. In this thesis, three transition elements, scandium, niobium and rhenium, were selected for the hyperfine structure study. Even though lot of work has been done

on these elements, still most of the information available is about the ground state or the low lying metastable states only. The aim of this work is to study the hyperfine structure of mainly the high lying metastable states and higher odd parity states using laser optogalvanic spectroscopy [14-15]. Fine structure studies were performed to identify the transition connecting these states.

In chapter II, the theory of fine structure, hyperfine structure and isotope shift is briefly reviewed. The effective operator formalism for the analysis of hyperfine structure is also presented.

Experimental details are given in chapter III. Problems in choosing an experimental setup are outlined. Laser Optogalvanic spectroscopy, the technique used in this thesis, is described along with the sputtering process in a hollow cathode discharge [16]. A brief working of ring dye laser, its frequency stabilization etc. and wavemeter used for dye laser wavelength monitoring is described. To test the experimental setup used for fine structure studies, broad band optogalvanic spectrum of vanadium was recorded and twelve transitions of V I were identified [17]. This spectrum is given along with all the identified lines. To test the high resolution experimental setup and the analysis procedure, the hfs spectra of one of the lanthanum transitions, at 582.19 nm and one of the niobium transitions, at 586.64 nm were recorded and analyzed [18-21]. These spectra and their results are presented along with the

description of the analysis procedure in this chapter. We observe a close agreement between our A and B values and the previously reported values.

Chapter IV gives the results of experimental studies performed on scandium. Scandium is the lightest element among all the transition elements with atomic number  $Z = 21$ , and has only one stable isotope with atomic mass number  $A = 45$ . It has nuclear spin  $I = 7/2$  nuclear magnetic moment  $\mu_I = 4.75626 \mu_N$  and nuclear quadrupole moment  $Q_I = -0.22 \text{ b}$  [22]. It has a large number of metastable states belonging to the even configurations  $3d^3$ ,  $3d^2 4s$ ,  $3d 4s^2$  [23]. Like any other transition element, scandium is also refractory in nature. Therefore, we used sputtering process in a hollow discharge for the production of free atoms for our studies. Till now hyperfine structure of scandium was studied mainly in the ground state and the low lying metastable states [24-29]. In the present work, we concentrate on the high lying metastable states and higher odd parity states. Since the atoms of interest are available in a discharge, the optogalvanic detection technique was employed. Optogalvanic spectrum of scandium was recorded in the range 575 nm to 635 nm and seventeen transitions were identified. Out of these seventeen transitions, hyperfine structure spectra of seven transitions were recorded. Most of these transitions join the high lying metastable states in the configuration  $3d^2 4s$  and higher odd parity states in the configuration  $3d^2 4p$ . A and B parameters for all the levels involved in these transitions were estimated and are reported [30].

Chapter V deals with the studies on niobium. Niobium is also a transition element with  $Z = 41$ , and has only one stable isotope with  $A = 93$ . Its nucleus has a spin  $I = 9/2$ , magnetic dipole moment  $\mu_I = 6.143 \mu_N$  [31] and electric quadrupole moment  $Q_I = -0.36 \text{ b}$  [32]. Since its nuclear magnetic dipole moment is large and electric quadrupole moment is small, it is expected to show well resolved hyperfine components. The separations between these components are quite close to those given by the interval rule. Niobium shows a dense fine structure spectrum because all the transitions originating from the large number of metastable states belonging to the configurations  $4d^5$ ,  $4d^4 5s$ ,  $4d^3 5s^2$  can be observed. Till now very little work has been done on niobium because of its refractory nature. Atomic beam magnetic resonance method could be employed only after the development of a universal evaporation technique [33-34].

Fine structure spectrum of Nb was recorded in the range 570 nm to 635 nm using optogalvanic technique. Thirty two transitions belonging to the first spectrum of Nb were identified. All these transitions along with their level assignments and optogalvanic intensity are reported. Hyperfine structure of twenty two of these transitions is studied and calculated A and B constants for all the levels involved are reported [21,35-37]. Wherever possible we compare our values with the already available data.

Chapter VI gives the results of the experimental studies performed on rhenium. Rhenium is also a transition element with

$Z = 75$ . It has two stable isotopes; one with  $A = 185$ , nuclear spin  $I = 5/2$ , nuclear magnetic dipole moment  $\mu_I = 3.1718 \mu_N$ , electric quadrupole moment  $Q_I = 2.8 \text{ b}$  and has 37.07 % natural abundance and other with  $A = 187$ , nuclear spin  $I = 5/2$ , nuclear magnetic dipole moment  $\mu_I = 3.2043 \mu_N$ , electric quadrupole moment  $Q_I = 2.6 \text{ b}$  and has 62.93 % natural abundance [22]. Since both the isotopes have same spin,  $5/2$ , and also their nuclear moments are nearly the same, therefore both of them show similar spectra. The only distinguishing factor is their relative intensities, which is proportional to their natural abundance. Unlike scandium and niobium, rhenium has a relatively large nuclear electric quadrupole moment. Therefore, in this case the separations between the various hyperfine components deviate from the interval rule. The doppler width of rhenium is relatively small owing to its large atomic mass. Therefore, most of the recorded spectra are well resolved. High resolution spectra of six transition were recorded and analyzed. Isotope shift between  $^{185}\text{Re}$  and  $^{187}\text{Re}$  in all these transitions is reported. Hyperfine coupling constants for all the levels involved, for both the isotopes are reported [38].

In conclusion optogalvanic spectra of Sc and Nb in the range 570 nm to 635 nm are recorded and the identified fine structure transitions are reported. Hyperfine coupling constants for a large number of states of Sc, Nb and Re, calculated from the recorded high resolution laser optogalvanic spectra of fine structure transitions, are reported.



## CHAPTER II

# THEORY OF HYPERFINE STRUCTURE AND ISOTOPE SHIFT

### 2.1 INTRODUCTION

Hyperfine structure was first observed by Michelson [8] and was later confirmed by Fabry and Perot [9] and Lumer and Gehrke [10]. To explain the observed structure they suggested that the samples used should have a natural abundance of many isotopes, however when later on observations on the single isotope atoms also showed similar kind of structure, this explanation was discarded. Pauli [39] proposed that hyperfine structure could be due to the interaction between the magnetic moments of the nucleus and the orbital electrons. But the measurements of Schuler and Schmidt [40] showed a deviation from the interval rule, which could not be explained on the basis of Pauli's theory. Casimir [41], in 1936, showed that if an electric quadrupole interaction between the nucleus and the electrons is also considered along with the magnetic dipole interaction given by Pauli, the experimental results could be explained in good agreement with the theory. Later on Schwartz in 1955 [42] generalized the Casimir's idea including the higher order multipole interactions and relativistic effects. In 1965 Sanders and Beck [43] gave a new formalism called the effective operator formalism for the analysis of the hfs data.

Hyperfine structure theory and the experimental results for single electron and many electron atoms are reviewed by Armstrong [12], Lindgren and Rosen [13], Childs [44], Olsson and Rosen [45] and Büttgenbach [46]. In the following section a brief theory of hfs is presented.

## 2.2 FINE AND HYPERFINE STRUCTURE

The first approximation in the theory of atomic structure is, nucleus is a point charge of infinite mass. This with the consideration of the electron spin gives rise to the fine structure of atomic levels. But in general nucleus has a finite mass and a finite size. Consideration of finite mass gives rise to the isotope shift (Mass shift). Further a finite size nucleus may or may not be spherically symmetric. A finite spherical shape gives rise to a shift in the electronic levels (volume shift or field shift). The isotope shift is discussed in section 2.3. However, if the nucleus is not spherically symmetric it will have a non zero spin ( $I$ ), this spin coupled with the total electronic angular moment of the atom results in hyperfine structure. Compared to coulomb interaction and the spin orbit interaction, hyperfine interaction is very weak. Hence hyperfine interaction can be considered as a perturbation to the fine structure Hamiltonian.

The total interaction Hamiltonian between the electrons and the nucleus in an atom can be expressed as a scalar product of the spherical tensors [43];  $T^k(e)$  and  $T^k(n)$ , as follows

$$\begin{aligned} H &= \sum T^k(e) \cdot T^k(n) \\ &= T^0(e) \cdot T^0(n) + \sum T^k(e) \cdot T^k(n) \\ &= H_{fs} + H_{hfs} \end{aligned} \quad (1)$$

where  $T^k(e)$  and  $T^k(n)$  are spherical tensors representing the electronic and nuclear part of the interaction. Nuclear wave functions with a definite parity would yield only even electric and odd magnetic moments. Thus even  $k$  gives electric and odd  $k$  gives magnetic part of the interaction. The monopole term ( $k = 0$ ) represents the coulomb interaction between the electrons and the spherical part of the nuclear charge distribution. Hamiltonian  $H$  for the monopole interaction can be written as

$$H = \frac{1}{2m_e} \sum_i p_i^2 - \sum_i \frac{ze^2}{r_i} + \sum_{i,j} \frac{e^2}{|r_i - r_j|} + \sum_i \epsilon_i \cdot e_i \cdot s_i \quad (2)$$

where  $p_i$  is the moment of the  $i$ th electron and  $m_e$  and  $e$  are the mass and the charge of the electron respectively; the summation is over all the electrons. The first term in eqn (2) represents the kinetic energy operator; second, the monopole electrostatic interaction between the nucleus and the electrons; third term, the electron - electron repulsion and the last term represents the

spin orbit interaction.  $l_i$  and  $s_i$  are respectively the orbital and the spin angular momenta of the  $i$ th electron and  $\epsilon_i$  is the spin orbit interaction constant. In the fine structure, orbital angular momentum and the spin of the electron couple to give total angular momentum ( $J$ ).

#### MAGNETIC DIPOLE INTERACTION

It is the interaction between the nuclear magnetic dipole moment  $\vec{\mu}_I$  and the magnetic field  $\vec{H}_J(0)$  produced by the extra nuclear electrons at the nuclear site. The Hamiltonian for the magnetic dipole interaction can be written as

$$H_M = -\vec{\mu}_I \cdot \vec{H}_J(0) \quad (3)$$

where  $\mu_I = -\mu_N g_I I = \frac{\mu_I}{I} I$ , where  $\mu_N$  is the nuclear magneton and  $g_I$  the nuclear  $g$ -factor. The magnetic field at the nucleus is produced by both the orbital motion and the spin of the electron and is linearly dependent on the total angular momentum  $\vec{J}$ , given as  $\vec{J} = \vec{L} + \vec{S}$ . Hence the Hamiltonian in eqn.(3) can be written as

$$H_M = h A \vec{I} \cdot \vec{J} \quad (4)$$

where  $A = - \frac{\vec{\mu}_I \cdot \vec{H}_J(0)}{h I J}$  is the magnetic dipole coupling constant.

For  $s$ -electrons ( $l=0$ ), an additional term called fermi contact

term arises because of the fact that these electrons have a non zero probability density at the nuclear site, Hamiltonian for this being given by

$$H_{FC} = a_s \vec{I} \cdot \vec{S} = a_s \vec{I} \cdot \vec{J} \quad (5)$$

where  $a_s$  is the constant depending upon  $\mu_I$  and the s-electron probability at the nucleus. This  $H_M$  is treated as a perturbation to the fine structure Hamiltonian. Wave functions are represented by  $|IJFM\rangle$ , where  $\vec{F} = \vec{I} + \vec{J}$  and takes the values  $|I - J|$ ,  $|I - J + 1|$ , .....  $|I + J|$  i.e. it has either  $2I+1$  or  $2J+1$  values depending upon whether  $I < J$  or  $I > J$ . The first order energy shifts are given by

$$\Delta E_M = \langle \gamma IJFM | H_{FIJ} | \gamma IJFM \rangle \quad (6)$$

$$= hAK/2 \quad (I > 0, J > 0) \quad (7)$$

where  $K = F(F+1) - I(I+1) - J(J+1)$ . The F level is  $2F + 1$  fold degenerate and the separation between the F levels, given by eqn. (7), follows the interval rule.

$$\Delta E(F) - \Delta E(F-1) = hAF \quad (8)$$

#### ELECTRIC QUADRUPOLE INTERACTION

The second major contribution to hyperfine Hamiltonian comes due

to the coupling between the nuclear quadrupole moment ( $\vec{Q}_I$ ) and the electric field gradient ( $\vec{q}_J$ ) due to the orbital electrons at the nuclear site. It is given by

$$H_E = \vec{Q}_I \cdot \vec{q}_J \quad (9)$$

The first order energy shift of a fine structure level  $J$  is given by

$$\Delta E = \langle IJFM | H_E | IJFM \rangle \quad (10)$$

$$= \frac{hB}{4} \frac{3/2 K(K+1) - 2I(I+1)J(J+1)}{I(2I-1)J(2J-1)}, \quad I \geq 1, J \geq 1 \quad (11)$$

This interaction vanishes when  $I = 0$  or  $I = 1/2$  i.e., when nuclear charge distribution is spherically symmetric. This also vanishes for  $S$  terms because in that case electric charge distribution is again symmetric. On combining both these contributions, the total energy shift of a hyperfine level is given by,

$$E_F = \frac{hAK}{2} + \frac{hB}{4} \frac{3/2 K(K+1) - 2I(I+1)J(J+1)}{I(2I-1)J(2J-1)} \quad (12)$$

Eqn (12) is the well known Casimir formula [41]. It can be shown from this formula that  $\sum (2F+1) E_F = 0$ . That means centre of gravity of a level  $J$  does not shift due to the hyperfine

interaction. Because of the second term in eq.(12), there is a deviation from the interval rule, defined by eq.(8).

The selection rules for the transitions between hyperfine multiplets are

$$\Delta J = 0, \pm 1, \quad \Delta F = 0, \pm 1, \quad (0 \leftrightarrow 0 \text{ is not allowed})$$

The relative intensities of transitions between the hyperfine levels are commonly derived from the sum rule, which states that the sum of intensities of all the components are proportional to the statistical weight,  $(2F+1)$ , of the levels involved.

For the transition  $J \rightarrow (J-1)$ , we have

$$\left. \begin{aligned} I_- &= \frac{I}{F} P(F).P(F-1) && \text{for } F \rightarrow (F-1) \\ I_0 &= \frac{(2F+1)}{F(F+1)} P(F).Q(F) && \text{for } F \rightarrow F \\ I_+ &= \frac{I}{F} Q(F).Q(F-1) && \text{for } (F-1) \rightarrow F \end{aligned} \right\} \quad (13)$$

whereas for the transition  $J \rightarrow J$ , we have

$$\left. \begin{aligned} I_0 &= \frac{(2F+1)}{F(F+1)} R^2(F) && \text{for } F \rightarrow F \\ I_{\pm} &= \frac{I}{F} P(F).Q(F-1) && \text{for } F \rightarrow F-1 \\ &&& \text{OR } F-1 \rightarrow F \end{aligned} \right\} \quad (14)$$

Where  $P(F) = (F+J)(F+J+1) - I(I+1)$

$Q(F) = I(I+1) - (F-J)(F-J+1)$

$R(F) = F(F+1) + J(J+1) - I(I+1)$

These intensities are listed in many books e.g. [47-49].

#### EFFECTIVE OPERATOR FORMALISM

Since velocities of the electrons near the nucleus are comparable to the velocity of light, we should consider the relativistic effects also. It can be done in two ways, either describing the electrons by relativistic Dirac wave functions and keeping  $H_{hfs}$  as such, or keeping wave function as non-relativistic and modifying the Hamiltonian to take care of the relativistic effects [43]. Since relativistic calculations are comparatively difficult,



mostly the second approach is followed. The modified Hamiltonian called the effective Hamiltonian is written as

$$H_{hfs}^{eff} = \sum_{K=1}^{\infty} T_{eff}^{(e)} \cdot T^{(n)} \quad (15)$$

It is of the same form as that of eqn (1). The hfs energy of an atomic state being given by

$$E_F = \langle IJFM | H_{hfs}^{eff} | IJFM \rangle \quad (16)$$

$$= \sum (-1)^{I+J+F} \begin{Bmatrix} I & J & F \\ J & I & K \end{Bmatrix} \langle J || T^{(e)} || J \rangle \langle 1 || T^{(n)} || 1 \rangle \quad (17)$$

where quantity in the parentheses is 6-j symbol. These symbols are tabulated by Cowan [50]. The reduced matrix elements are independent of the magnetic quantum number M. The hyperfine structure removes the degeneracy in F, F dependence is entirely contained in the 6-j coefficient and a phase factor. Equation (15) can also be written as

$$E_F = \sum_{K=1}^2 A_K M(I, J; F, K) \quad (18)$$

where  $A_K = \langle II || T^{(n)} || II \rangle \langle JJ || T^{(e)} || JJ \rangle$ . These  $A_K$ 's are related to the A and B constants in the Casimir formula (eqn. 12), through  $A_1 = A/1$  and  $A_2 = B/4$ . Solving eqn. (17) and (18) and using  $\langle II || T^{(n)} || II \rangle = \mu_I$  and  $\langle JJ || T^{(e)} || JJ \rangle = q_J$ , one gets the Casimir formula [41].

The hyperfine constants, A and B, are related to the reduced matrix elements of the effective tensor operators  $T(e)$  and  $T(e)$  through

$$A = \frac{\mu_I}{I} [J(J+1)(2J+1)]^{-1/2} \langle J \| T(e) \| J \rangle \quad (19)$$

$$B = 2eQ_I \left[ \frac{2J(2J+1)}{(2J+3)(2J+2)} \right]^{1/2} \langle J \| T(e) \| J \rangle \quad (20)$$

The effective tensor operators can explicitly be expressed as [12,13]

$$T(e) = 2\mu_o \sum_{i=1}^N [ \vec{l}_i \cdot \langle r_i^{-3} \rangle_{04} - \sqrt{10} (\vec{S}_i \cdot \vec{C}_i^2) \langle r_i^{-3} \rangle_{12} + \vec{S}_i \cdot \langle r_i^{-3} \rangle_{10} ] \quad (21)$$

$$T(e) = e \sum_{i=1}^N [ -\vec{C}_i^2 \langle r_i^{-3} \rangle_{02} + (\vec{S}_i \cdot (\vec{C}_i^4 \cdot \vec{l}_i)^3)^2 \langle r_i^{-3} \rangle_{13} + (\vec{S}_i \cdot \vec{l}_i)^2 \langle r_i^{-3} \rangle_{10} ] \quad \dots\dots\dots(22)$$

Summation is over all the electrons in the open shells,  $l_i$  and  $S_i$  are the orbital and spin angular momenta of the  $i$ th electron,  $C_q^K$  are the  $q$ th component of a tensor operator of rank  $K$  and is related to the normalized spherical tensors  $Y_q^K$  by

$$C_q^K = [4\pi/(2K+1)] Y_q^K \quad (23)$$

and  $\langle r_i^{-3} \rangle$  are the radial integrals of the type  $\int R(r) \langle 1/r_i^{-3} \rangle R(r) r^2 dr$ , where  $R(r)$  is the radial part of the electronic wave function. The radial integrals  $\langle r_i^{-3} \rangle_{04}$ ,  $\langle r_i^{-3} \rangle_{12}$

$\langle r^{-3} \rangle_{10}$ ,  $\langle r^{-3} \rangle_{02}$  represent orbital, spin dipole, Fermi contact and quadrupole interaction terms respectively. In the non relativistic limit  $\langle r^{-3} \rangle_{01} = \langle r^{-3} \rangle_{12} = \langle r^{-3} \rangle_{02} = \langle r^{-3} \rangle_{n1}$ , ( $l=0$ ) for non s-electrons and for s-electrons  $\langle r^{-3} \rangle_{10} = 4\pi \delta(r) = 0$ .

It is very difficult to calculate the above said radial integrals, therefore, they are generally interpreted as radial parameters;

$$a_{10}(1) = \frac{4}{3} \frac{\mu_0}{4\pi} \mu_B \frac{\mu_I}{I} \langle r^{-3} \rangle_{10} \quad (24a)$$

$$a_{kl}(1) = 2 \frac{\mu_0}{4\pi} \mu_B \frac{\mu_I}{I} \langle r^{-3} \rangle_{kl} \quad (24b)$$

$$b_{kl}(1) = e^2 Q_I \langle r^{-3} \rangle_{kl} \quad (24c)$$

The parameters given by eqn. (24) can be determined from the least square fit to the experimental hfs data. A parameter expression for the hfs constants, A and B, can be obtained only if we can evaluate the radial integrals appearing in these expressions, which requires accurate values of the wave functions. If we know A and B constants for at least three levels in one configuration we can calculate the radial parameters and hence radial integrals. The evaluated radial integrals can be compared with the values for the same parameters obtained from other semi empirical methods. When the fine structure constant  $\xi_j$  is known these integrals can be expressed as [51]

$$\langle r^{-3} \rangle_{kl} = 0.17114 F_{kl}(1, Z_{\text{eff}}) \frac{\xi_1}{Z_{\text{eff}} H} a_0^{-3} \quad (25)$$

$F_{kl}$  and  $H$  are relativistic Casimir correction factors, tabulated by Kopfermann [49].  $Z_{\text{eff}}$  is the effective charge number;  $Z_{\text{eff}}$  is equal to  $(Z-4)$  for p-electrons  $(Z-1)$  for d-electrons and  $(Z-35)$  for 4f-electrons [49]. The parameter corresponding to the unpaired s-electrons,  $\langle r_1^{-3}(s) \rangle$ , is correlated to the density of s-electrons at the nucleus and can be estimated as

$$\langle r_1^{-3}(s) \rangle = 4\pi |\psi_s(0)|^2 F(1/2, Z_{\text{eff}}) (1-\delta_z)(1-\epsilon) \quad (26)$$

$F, \delta$  and  $\epsilon$  are relativistic correction factors [49]. Thus we can compare the values of radial integrals obtained from hfs studies those obtained from eqn. (25) and (26) which will in turn be a test of the wave functions used to evaluate the reduced matrix elements (eqn. (19) and (20)).

### 2.3 ISOTOPE SHIFT

Bohr's theory of atomic structure suggests that the spectra of different isotopes should be mass dependent. Therefore, efforts were made to measure isotope shift. However, the experimental observations showed that predictions of Bohr's theory, which considered just the mass of the isotope, are not enough to explain the observed isotope shifts [52]. In actual practice both the

effect of finite mass and effect of finite volume of the nucleus have to be taken into account [53]. In the following section we give a brief theory of isotope shift.

#### MASS EFFECT

The first term in the fine structure Hamiltonian given by eqn. (2) gives the kinetic energy where  $M$ , the nuclear mass, is infinite; however, for a nucleus with a finite mass it becomes

$$T = \frac{p_n^2}{2M} + \sum_i \frac{p_i^2}{2m_e} \quad (27)$$

where  $\vec{p}_n$  is the momentum of the nucleus, from conservation of momentum it follows that  $\vec{p}_n = -\sum_i \vec{p}_i$ , therefore,

$$T = \frac{\sum_i p_i^2}{2M} + \frac{1}{2M} \sum_i p_i \cdot p_i + \frac{\sum_i p_i^2}{2m_e} \quad (28)$$

First and the third term in eqn. (28) can be combined by introducing  $\mu = \frac{m_e M}{m_e + M}$ , the reduced mass. Replacing  $m_e$  with  $\mu$  gives rise to a shift ( $\Delta E$ ) in the fine structure energy level,

$$\Delta E = E(\mu) - E(\infty) = -E(\infty) \frac{m_e}{m_e + M} \quad (29)$$

For a transition corresponding to a wavenumber  $\tilde{\nu}$  and two isotopes with masses  $M$  and  $M'$ , the mass shift is given by

$$\delta\tilde{\nu}_{\text{NMS}} = m_e \frac{\delta M_{\tilde{\nu}}}{MM'} \tilde{\nu} \quad (30)$$

$\delta\tilde{\nu}_{\text{NMS}}$  in eqn. (30) gives Normal Mass Shift (NMS).

The second term in eq.(28) is due to the correlation in the momenta of electrons. This gives rise to another type of shift called the Specific Mass Shift. It has the same type of  $M$  dependence as  $\delta\tilde{\nu}_{\text{NMS}}$ . It can be roughly estimated [54] as

$$\delta\tilde{\nu}_{\text{SMS}} = (0.3 \pm 0.9) \delta\tilde{\nu}_{\text{NMS}} \quad \text{for } ns \rightarrow np \text{ transition} \quad (31a)$$

$$\delta\tilde{\nu}_{\text{SMS}} = (0 \pm 0.5) \delta\tilde{\nu}_{\text{NMS}} \quad \text{for } ns^2 \rightarrow nsnp \text{ transition} \quad (31b)$$

Because of  $\frac{1}{M^2}$  dependence, mass effects will be comparatively small in heavy elements.

#### FIELD EFFECT

When a nucleus has a finite size the electrostatic potential outside the nucleus is still the same as that of a point nucleus with the same charge, but inside the nucleus it varies with the size. It may thus be seen, that the finite nuclear charge distribution changes the binding energy of the electrons through the overlap of their wave function with the nuclear volume. Since the change is noticeable inside the nucleus, the effect is

important only for s- or  $p_{1/2}$  electrons as they have non-zero wave functions at the nucleus. The field shift is related to the nuclear charge distribution [54,55], by

$$\delta \tilde{v}_{1,FS} = E_1 f(Z) \delta \langle r^2 \rangle \quad (32)$$

where  $\delta \langle r^2 \rangle$  is the change in the mean square nuclear charge radius.  $E_1$  is the electronic factor proportional to the change, during the transition, in the total non-relativistic electron charge density  $(\Delta |\psi(0)|^2)$  at the nucleus and is given by

$$E_1 = \frac{\pi a_0^3}{Z} \Delta |\psi(0)|^2, \quad (33)$$

where  $a_0$  is the Bohr radius.  $f(Z)$  in eqn. (32) accounts for the relativistic correction to the electronic wave function and hence  $\Delta |\psi(0)|^2$ , and is given by

$$f(Z) = \frac{\bar{Z} C_{unif}}{\sqrt{M} r_0^2 (M' + M)} \quad (34)$$

where  $M = \frac{M+M'}{2}$ ,  $r_0 = 1.20$  fm,  $C_{unif}$  is the theoretical isotope shift constant for a uniformly charged sphere of radius  $R = r_0 A^{1/3}$  tabulated by Babushkin [56].

Experimentally measured isotope shift can be used to calculate  $\delta \langle r^2 \rangle$  (eqn.(32)), which can be interpreted to get information about the structure of the nucleus.

## CHAPTER III

### EXPERIMENTAL DETAILS

#### 3.1 INTRODUCTION

Experimental methods employed for studying hyperfine structure (hfs) of atoms can be broadly divided into two categories [49]. One, those based on atomic beam experiments, where transitions between individual sub levels within a hyperfine structure multiplet (magnetic dipole radiation) are observed. These experiments give quite accurate values of the hyperfine parameters. But their application is limited to the study of metastable states only. In the second category are the experiments where transition between two different hfs multiplets is studied. In these experiments only emission lines are studied by interferometric techniques. Experiments employing optical absorption did not become popular mainly because of nonavailability of narrow band, tunable light sources. Development of tunable dye lasers have provided solution to this problem. They have not only simplified the old techniques but have given birth to many new spectroscopic techniques with much higher resolution and higher sensitivity [1-7]. In laser spectroscopy, generally, absorption of laser radiation by the sample is detected. Usually, this is done by monitoring the light emitted from the levels populated by laser



excitation. The technique is not convenient though sensitive. In many cases fluorescence is drowned in very high background signal and good filtering methods are needed to extract the signal [7]. In such cases other unconventional techniques are preferred. One such technique is optogalvanic detection [14,15]. This technique is convenient and sensitive, if the sample under study is in the form of a discharge. The plasma can be from electrical discharge, high frequency discharge or in the flames [14,15,57]. The high sensitivity of optogalvanic spectroscopy makes it possible to study many transitions otherwise difficult. In this technique the discharge, which is our sample, serves the purpose of the detector also. Unlike fluorescence detection here no filtering technique is required and signal to noise ratio is quite high [14].

### 3.2 OPTOGALVANIC SPECTROSCOPY

Optogalvanic spectroscopy (OGS) is based on the optogalvanic effect; the change in electrical impedance of the discharge due to variation in effective ionization rates induced by resonant absorption of radiation. Optogalvanic effect, previously known as JOSHI EFFECT [58] has been studied extensively [59-70]. Badareu et al. [65] were the first to use this effect for absorption spectroscopy. Development of tunable dye lasers started a new era in the optogalvanic spectroscopy [66].

A qualitative explanation of the optogalvanic effect is simple. But the complexity of all the phenomenon involved in the

process following the excitation and finally leading to the ionization, makes it difficult to develop a general quantitative theory. In fact several parameters, strongly dependent on the particular type of discharge, have to be taken into account. For qualitative explanation two different mechanisms are proposed [15]. According to one mechanism, the absorption of laser radiation by the constituents of the discharge perturbs the steady state populations of the bound atomic or molecular levels. Since different levels will generally have different ionization probability; absorption of radiation will give rise to a net change in the ionization rate in the discharge. This perturbation leads to a change in the current through the plasma, or equivalently a change in the impedance of the discharge. According to the second mechanism, the excitation of atoms by the laser radiation to higher electronic states perturbs the equilibrium established between the electronic temperature and the atomic excitation temperature. The super elastic collisions between the electrons and the laser excited atoms in the discharge tend to restore the equilibrium. In this process an excess amount of energy is released and the result is an increase in the electron temperature in the discharge or in other words an increase in conductivity or decrease in impedance of the discharge. Both the mechanisms explain optogalvanic effect qualitatively and their relative importance depends upon the discharge and excitation conditions.

There have been some attempts [68-69] to develop a model based on simultaneous solution of the plasma equations, rate equations and Maxwell's equations to explain optogalvanic effect quantitatively, but most of them failed to explain the observed facts. In 1979, Eraz et al. [70] presented a simplified phenomenological theory of the optogalvanic effect. The theory could explain the relative magnitudes, sign changes and time evolution of the signals in the pulsed and CW laser excitation. They defined  $\alpha$ , a multiplication factor, as the number of electrons reaching anode for each electron emitted from the cathode.  $\alpha = 1$ , corresponds to steady state,  $\alpha > 1$  ( $< 1$ ) gives rise to an increase (decrease) in the discharge current. In the small signal domain, which mostly is the case,  $\alpha = 1$ .  $d\alpha$  can be written as

$$d\alpha = \left( \frac{\partial \alpha}{\partial V} \right)_{n_i} \Delta V + \sum \left( \frac{\partial \alpha}{\partial n_i} \right)_{V, n_j, j=1} \Delta n_i \quad (35)$$

$$= 0$$

where  $V$  is the voltage across the tube,  $\Delta V$  is the change in voltage (OG signal),  $n_i$  is the population of the atoms/ions in the  $i$ th state,  $\Delta n_i$  is the change in the  $i$ th state population. Eqn.(35) can be rearranged to yield

$$\Delta V = -\beta \sum_i a_i \Delta n_i \quad (36)$$

where  $\beta = \left( \frac{\delta \alpha}{\delta V} \right)_{n_i}^{-1}$  and  $a = \left( \frac{\delta \alpha}{\delta n_i} \right)_{n_i, V}$

Qualitatively it can be shown that  $\beta$  and  $a_i$  are always positive and generally, for  $E_1 > E_j$ ,  $a_1 > a_j$ . Considering the transition between levels 1 and 2, they used the rate equations approach to arrive at

$$\Delta V = -\beta \sigma_{12} I_{12} (a_2 T_2 - a_1 T_1) (n_2 - n_1) \quad (37)$$

where  $I_{12}$  and  $\sigma_{12}$  are the resonant laser intensity and the optical cross section for the transition  $1 \rightarrow 2$ . If  $E_1 < E_2$  then  $n_1 > n_2$  and  $a_2 > a_1$ . From eqn. (37) it follows:

(1) The optogalvanic signal  $\Delta V$  is always negative unless  $a_1 T_1 > a_2 T_2$ . In general the net result of radiation absorption is to shift population towards the upper levels from where the collisional ionization takes place more easily i.e. a net increase in ionization or decrease in impedance and a negative optogalvanic signal. the reverse can also happen when the transition originates from some metastable level. All this is controlled by the relaxation times  $T_1$  and  $T_2$  which are very sensitive to the plasma conditions. A small change in the current and the buffer gas pressure may change the sign of the optogalvanic signal.

(2) In the small signal limit optogalvanic signal is proportional to  $(n_1 - n_2)$  and  $\sigma_{12} I_{12}$ .

(3) The temporal behaviour of the signal is that of  $(I_{12})$

Optogalvanic spectroscopy is used to investigate various types of discharges, e.g. thermionic diode operating in the space charge limited mode, hollow cathode discharges, positive columns, R-F discharges and flames etc. Our main interest in this thesis is in OGS of sputtered atoms in the hollow cathode discharge.

### 3.3 PRODUCTION OF SPUTTERED VAPOURS

Spectroscopy with sputtered atoms [16,67] is important because of many reasons. Firstly, production of free atoms by sputtering is much more easier as compared to thermal evaporation methods. Even highly refractory elements, as in our case, can be sputtered in hollow cathode discharge by passing only a few milliamperes of current. Secondly, even though these atoms are emitted from the cathode with high energies of the order of 10eV [16], but at gas pressures  $\sim 5-6$  torr, typical in a discharge they lose their energies due to the collisions with the buffer gas atoms. Since the buffer gas atoms have energies corresponding to the environmental temperature, the final energies of the sputtered atoms after equilibrium are quite low. Thus in turn we get much smaller Doppler widths as compared to the thermally produced atoms [16,67], hence making it possible to perform high resolution spectroscopy without using Doppler free techniques. Thirdly, in a

discharge we have population of atoms not only in ground state but also in high lying metastable states. Therefore it is possible to study transitions originating from metastable states also.

In a discharge the cathode is continuously bombarded by energetic ions accelerated in the high field of the cathode dark space or by fast neutral atoms produced by resonant charge exchange. These atoms and ions with high energies can eject atoms from the cathode surface. the process is described in detail in a review by Hannaford [16].

### 3.4 EXPERIMENTAL DETAILS

#### BROAD BAND OPTOGALVANIC SPECTROSCOPY

The experimental arrangement used for the fine structure studies performed is shown in Fig. 1. A tunable CW dye laser (Spectra Physics 375), pumped by a five watt argon ion laser (Spectra Physics 2020-05), was used. Schematic of the dye laser used is shown in Figure 2. Rhodamine 6 G dye solution in methanol and ethylene glycol (Ethandiol) was circulated at high pressure so that as it comes out of a fine nozzle it forms a fine, thin and homogeneous jet stream. This part of the dye solution is the active medium for the dye laser. The pump beam was focused by the mirror  $M_p$  on the dye jet. A folded cavity was formed by the mirrors  $M_1$  ( $f = 5$  cm),  $M_2$  ( $f = 5$  cm) and the plane output mirror  $M_3$ . A structure of three invar rods holds these mirrors in position. The wavelength tuning was achieved by a birefringent

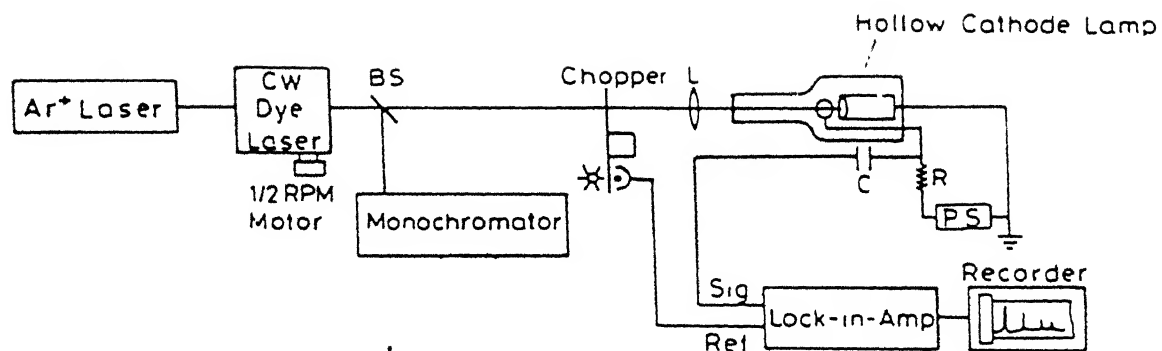


Fig. 1. Experimental setup used for fine structure studies.  
BS -beam splitter; L -lens; C -DC blocking capacitor;  
R -ballast resistor; PS -power supply.

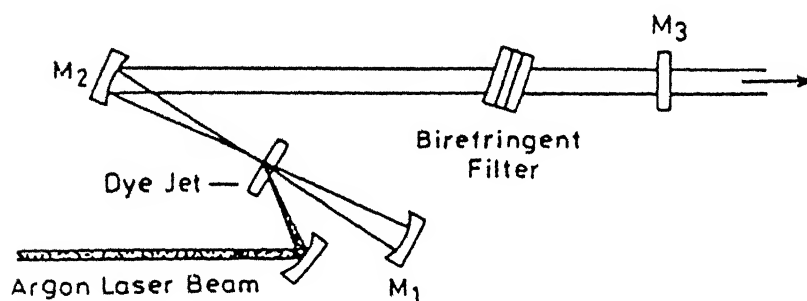


Fig. 2. Schematic of the standing wave dye laser (Spectra Physics 375).

filter. Both the filter and the jet are held at Brewster's angle to the laser beam.

We usually had more than 400 mW of output power for 3 W of the pump laser power. The output laser beam was focused into the hollow cathode lamp using a focusing lens ( $f = 15$  cm). To facilitate phase sensitive detection the dye laser beam was chopped by a mechanical chopper (Ithaco 220A). The chopping frequency was adjusted in the range 300 to 700 Hz. The discharge in the hollow cathode lamp was maintained with a regulated high voltage power supply (Aplab 7323 India). The optogalvanic signals were monitored across a  $10\text{ k}\Omega$  ballast resistor through a  $0.1\text{ }\mu\text{F}$  dc-blocking capacitor and were fed to the lock-in-amplifier (Stanford Res. Sys. 510) through a fast over voltage protection circuit. Reference signal for the lock-in-amplifier were obtained from the chopper. The lock-in-amplifier amplifies the signals appearing in phase or with a constant phase difference with the reference. This way all the noise, which is random in nature, is left out resulting in a significant increase in signal to noise ratio. The output from the lock-in amplifier was recorded by a strip chart recorder. The wave length of the dye laser was monitored by a double monochromator (Spex 1402) having a resolution of  $0.01\text{ nm}$ .

#### HIGH RESOLUTION OPTOGALVANIC SPECTROSCOPY

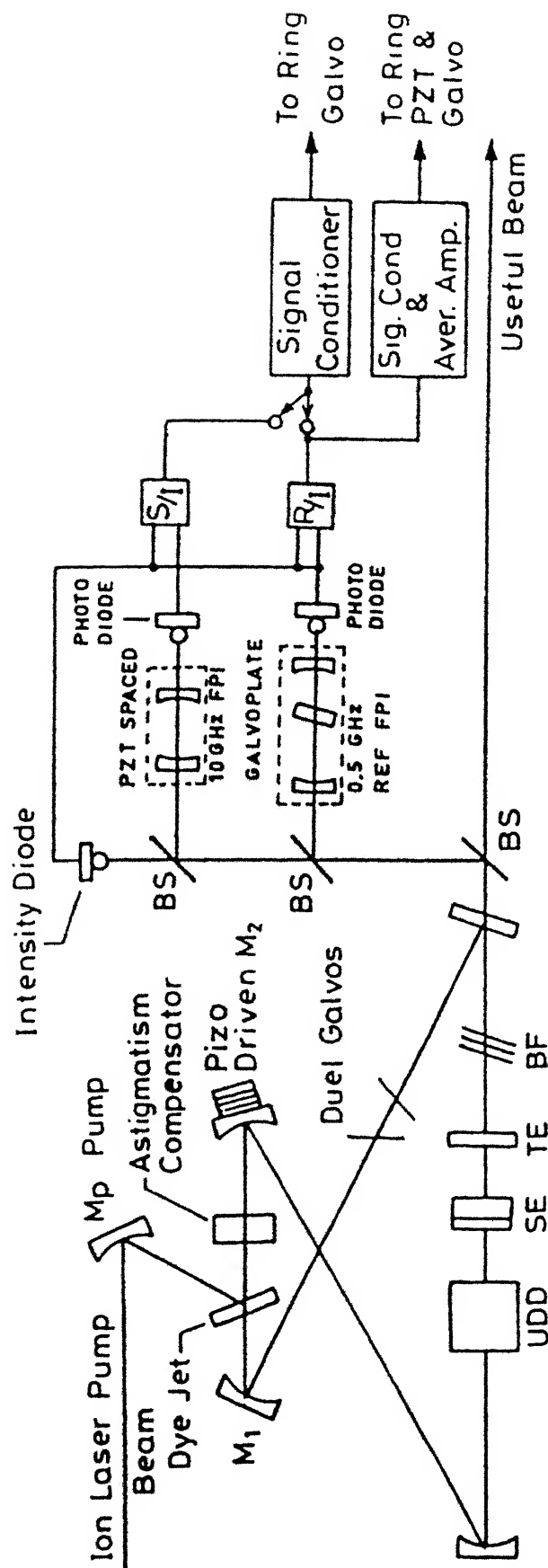
Resolution of any spectrum is decided by two factors viz. source linewidth which is inherent of the sample under study and the



instrumental line width which is a characteristic of the detection system. Here in our case source line width is mainly the Doppler width which depends upon the atomic mass, wavelength under study and the equilibrium thermal energies of the atoms. In the visible range, it is of the order of few hundred MHz to few GHz. Instrumental line width in this type of experiments is the laser line width. We can neglect this width by reducing the laser line width to a very small fraction of the Doppler width. Thus for all practical purposes the resolution is limited mainly due to the Doppler width. Therefore, the vital instrument in the experimental setup is a narrow band tunable dye laser which is stable in frequency and intensity. We used a single frequency ring dye laser (Spectra Physics 3800).

#### THE RING DYE LASER

Schematic of ring dye laser is shown in Fig. 3. This is a travelling wave dye laser. In contrast to the standing wave dye lasers this type of lasers can give much higher power output. The travelling wave configuration helps in preventing multi mode operation and hence can give better frequency stability. The pump beam, CW  $\text{Ar}^+$ , is focused onto a vertical dye jet. The jet is positioned inside the horizontal ring cavity formed by mirrors  $M_1$  ( $f = 3.5$  cm),  $M_2$  ( $f = 10$  cm),  $M_3$  ( $f = 23$  cm) and plane output mirror  $M_4$ . The cavity can support two counter propagating travelling waves. One of these is suppressed by a unidirectional device, a Faraday isolator.



UDD: Uni Directional Device

SE: Scanning Etalon

TE: Thin Etalon

BE: Birefringent Filter

BS: Beam Splitter

Fig. 3. Schematic of the ring dye laser (Spectra Physics 380D) and external reference station.

The longitudinal mode spacing of the ring cavity of the ring dye laser is about 200 MHz. Since the dye gain curve extends over several hundred Angstroms, simultaneous lasing takes place at a very large number of cavity modes. One out of these modes is selected using intra cavity devices, a birefringent filter, a thick etalon and a thin etalon. The birefringent filter selects a band of operation and helps in broad band tuning. A thick etalon with free spectral range (FSR) of 75 GHz selects one mode out of the modes already selected by the birefringent filter. To prevent the jumping of frequency of the laser to the adjacent mode, a thin etalon of 900 GHz FSR is introduced inside the cavity. The relative transmission curves of all the intra cavity elements are shown in the Fig. 4.

Frequency of a free running laser keeps changing due to many reasons, e.g. atmospheric pressure variations, acoustic and mechanical vibrations, temperature changes, convection currents and variations in the dye jet thickness. Mode hops can also be caused by extensive disturbances or bubbles passing through the dye jet. To avoid this, the frequency of the ring dye laser is locked to a fringe of an external interferometer (FSR = 0.5 GHz) which is thermally stabilized. The reference interferometer operates over the entire visible and near IR spectral regions and provides a high rate of change of transmission as a function of frequency. So any change in frequency of the laser is detected as a change in intensity which is normalized to the laser power. This change generates an error signal which is fed back to the

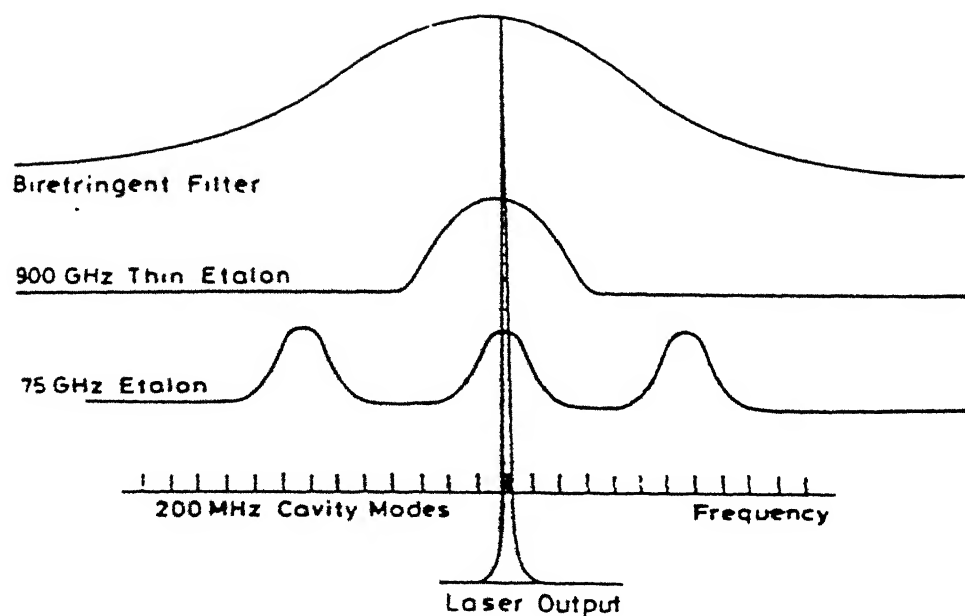


Fig. 4. Transmission curves of the intracavity devices; birefringent filter, thick etalon and thin etalon, of the ring dye laser.

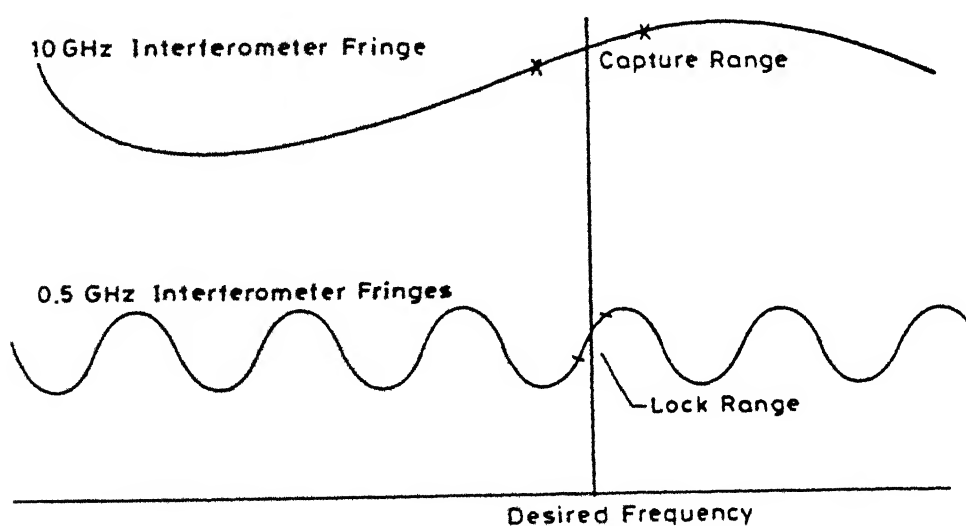


Fig. 5. Transmission curves of the reference interferometers. Locking point for the laser and their capture ranges are shown.

piezoelectrically driven mirror  $M_2$  and the dual galvoplates to correct the change in frequency. Since the cavity mode spacing is 200 MHz, a change of more than two cavity modes shifts the laser frequency, to lock to another fringe of the reference interferometer. In such situations the the control immediately goes to another interferometer (slave) with FSR of 10 GHz, the laser is returned to the original fringe. In normal circumstances this interferometer is passive. The locking point and the capture ranges of the two interferometers are shown in the Fig. 5. The stabilization system reduces the laser line width to less than 1 MHz.

The coarse wavelength tuning is achieved by using the birefringent filter. For fine tuning the dual galvoplates and the thick etalon are scanned simultaneously. With all the devices inside the cavity, the single frequency output can be scanned over a range of 30 GHz. Since this frequency is locked to an external interferometer, the actual tuning is done by scanning the reference interferometer with the help of a quartz plate inside the interferometer and the laser being dragged along. If a mode hopp occurs during the scan, both the reference and the slave interferometer momentarily stop scanning and continue soon after the frequency is brought back to the correct fringe of the reference interferometer.

### THE WAVELENGTH METER

In the initial stages of the experimental work a double monochromator was used to select the wavelength of interest. But this is very inconvenient and time consuming method. In the later stages a wavemeter (Burleigh - WA 20) was used for this purpose. The wavemeter is based on a fringe counting Michelson interferometer. This compares the unknown dye laser wavelength with the accurately known wavelength of a He-Ne laser (632.817 nm). The schematic of the wavemeter is shown in Fig. 6.

The He-Ne laser beam is split into two beams by a beam splitter (BS). Both the beams are reflected back parallel to itself by two retroreflectors fixed on a carriage which can move through a distance of about 5 cm. These reflected beams are again combined to interfere and are detected by a photo diode. As the carriage moves, the path of one of the beams is shortened and that of the other is lengthened. The interference of these two beams is detected by a photodiode and a counter counts the fringes shifted. The light beam from the dye laser follows the same path but in the opposite direction. Its interference is detected by another photo diode. The counting rate from these two photo diodes is related to the wavelength of the input laser.

### EXPERIMENTAL SETUP

A schematic of the experimental set up used is shown in Fig. 7. An 18 W argon ion laser pumps the ring dye laser. The ring dye laser usually gives more than 400 mW of single frequency output power

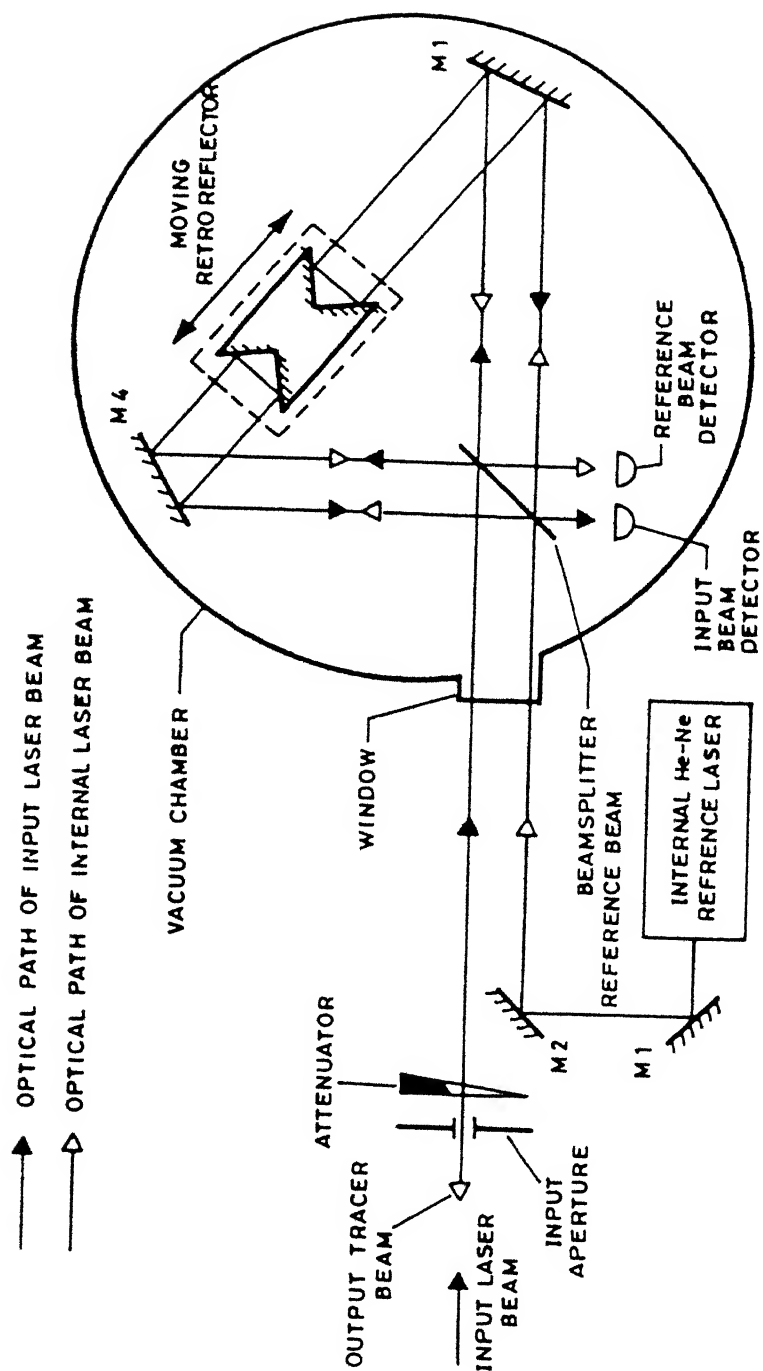
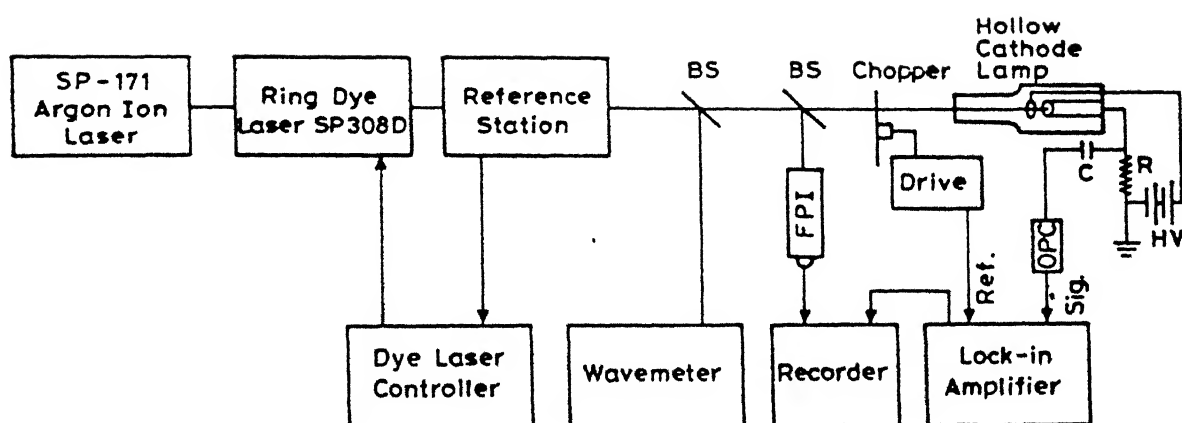


Fig. 8. Schematic of the wavemeter (Burleigh WA-20).



**Fig. 7.** Experimental setup used for recording hfs spectra using laser optogalvanic spectroscopy (LOGS).



for 4 W of pump power and can be scanned electronically over a range of 30 GHz. A wavemeter (Burleigh WA-20) was used to monitor the laser wavelength. In some of the experiments, in the early stages, a double monochromator (Spex 1402) was employed for the purpose. Frequency markers were obtained from the transmission through a 300 MHz FSR Fabry Perot interferometer (Coherent 216). Other details, the detection system etc., are similar to that used in the broad band spectroscopy work.

### 3.5 TEST STUDIES

#### OPTOGALVANIC SPECTROSCOPY OF VANADIUM

Optogalvanic spectra of V/Ne hollow cathode lamp were recorded using the setup shown in Fig. 1. The lamp was operated at 15 mA of current and chopping frequency was kept around 465 Hz. Peak laser power was 150 mW. A part of the observed spectrum is shown in Fig. 8. Some of the strong, well known Ne lines were identified and were used for calibration of the entire spectrum. Rest of the Neon and Vanadium transitions' wavelengths were calculated by interpolation. Identified vanadium lines are listed in Table I along with their optogalvanic intensities. Level assignments are taken from [17].

#### HIGH RESOLUTION OGS OF La I and Nb I

Hyperfine structure spectrum of a transition of La I, at 582.19 nm was recorded with an experimental setup shown in Fig. 7. The

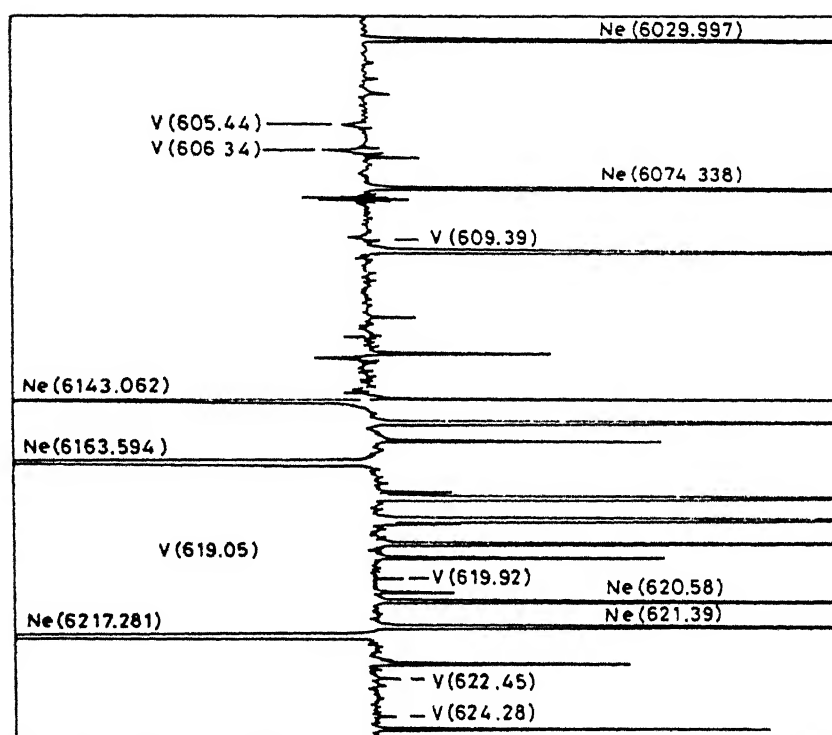


**Fig. 8.** Fine structure spectrum of vanadium and neon recorded by laser optogalvanic spectroscopy.

transitions was chosen because the hfs constants for both the levels involved in this transition are known [18,19]. Lamp was operated at a current of 10 mA, chopping frequency was around 465 Hz. and the max laser power was 100 mW. The observed spectrum of this transition is shown in Fig. 9(a). The observed line width in this transition is 1200 MHz, the corresponding atomic temperatures being 1100 K. This proves the fact that the equilibrium energy of the sputtered atoms is quite low and the optogalvanic spectroscopy is suited for high resolution work.

Niobium is one of the elements extensively studied in this thesis. One of its transitions at 586.645 nm was recorded to test our experimental setup and the analysis procedures. This line was chosen because its constants are known to a high degree of accuracy [20].

In the case of Niobium, signals are usually weak because of the following reasons. Firstly, it has a large number of metastable states and hence population is distributed among all of them. Secondly, transition probability of most of the transitions falling in the region of our interest is low. Therefore, in this case lamp was operated at relatively higher current, 20 - 25 mA, to have good signal to noise ratio. Chopping frequency and the laser power were 460 Hz and 100 mW respectively. Recorded spectrum of this transition is shown in Fig. 10(a).

La 582.19 nm

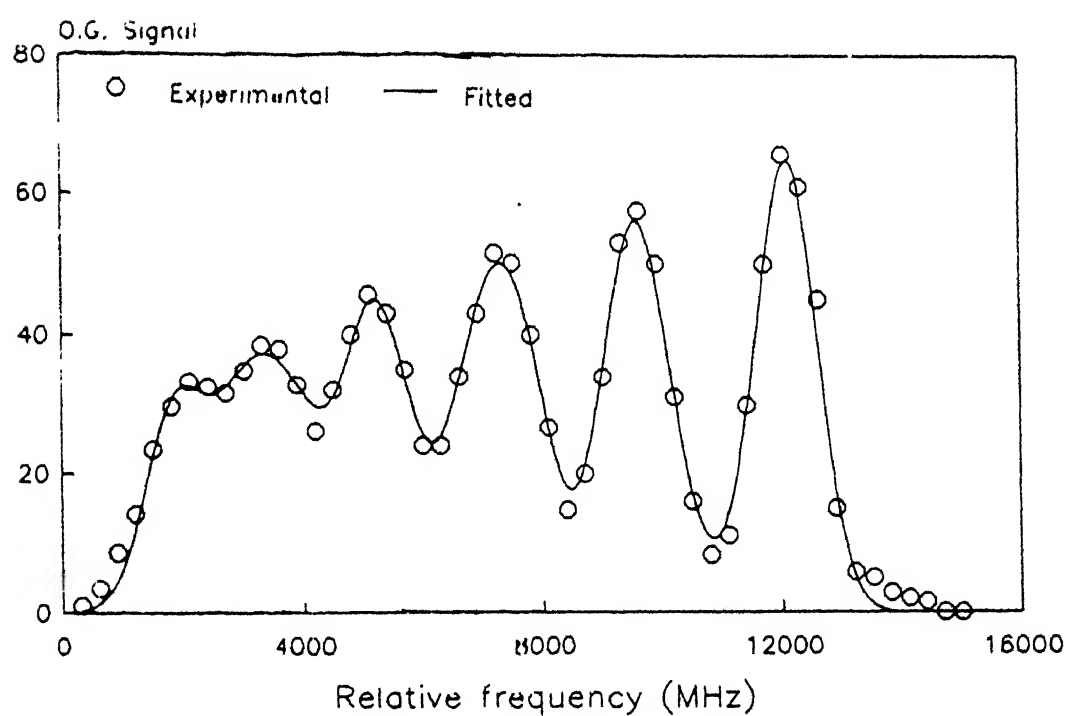
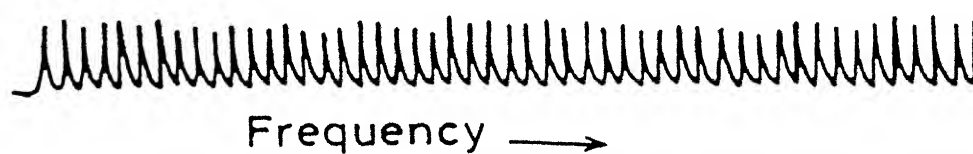
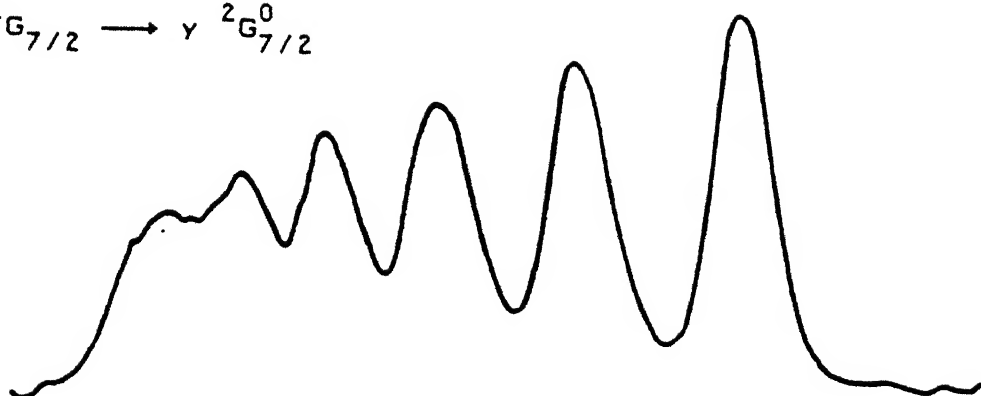


**Fig. 9.** Hyperfine structure of lanthanum transition at 582.19 nm. (a) recorded spectrum (b) computer fitted spectrum.

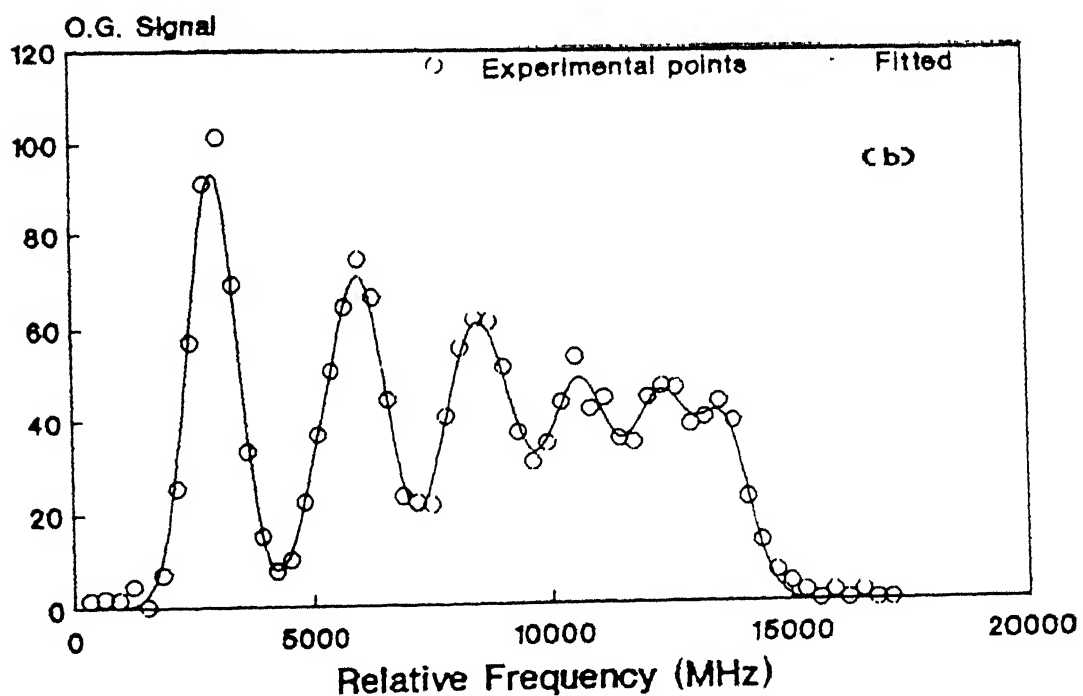
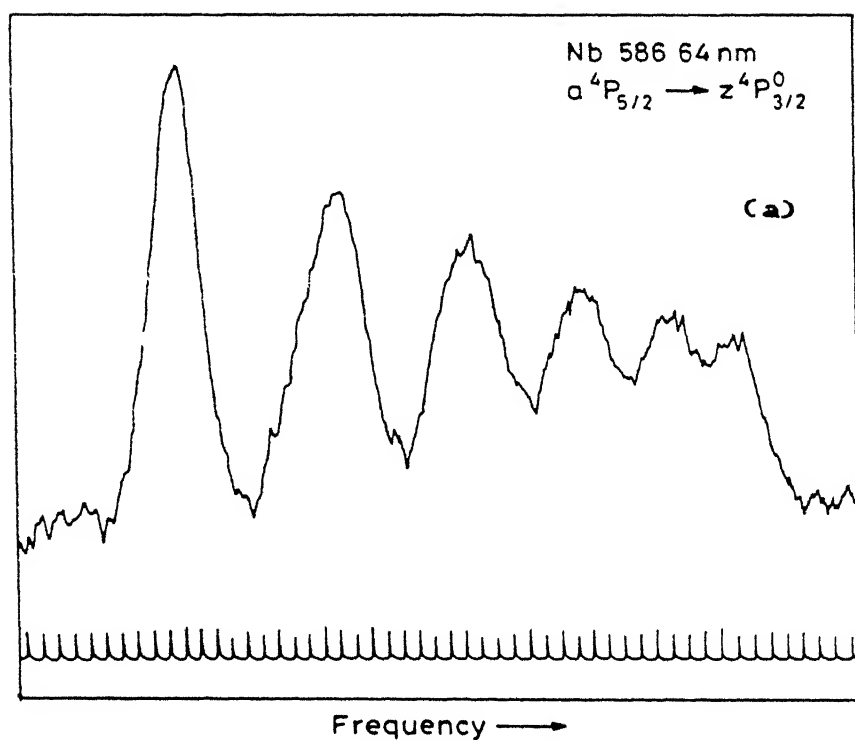


**Fig. 10.** Hyperfine structure of niobium transition at 586.64 nm.  
(a) recorded spectrum (b) computer fitted spectrum.

### 3.6 DATA ANALYSIS

Following procedure was followed for analysis of the recorded spectra. To start with various peaks are identified by comparing their relative intensities as given by eqns. 13 and 14. These peak positions are then used to calculate the initial values of the hyperfine structure constants, A and B, using a standard computer program (Numerical Algorithm Group). The calculated values of A's and B's, along with I and J's and an initial value of the linewidth, were fed to another program which calculates the peak positions and generates the whole spectrum. This generated spectrum was compared with the actually recorded one. If both the spectra match then these A's and B's were used as input for the final fitting program.

The final fitting program which uses least square minimization procedure is one of the standard routines supplied by the Numerical Algorithm Group. This program needs, I,  $J_{\text{lower}}$ ,  $J_{\text{upper}}$ , starting values of  $A_{\text{lower}}$ ,  $A_{\text{upper}}$ ,  $B_{\text{lower}}$ ,  $B_{\text{upper}}$ , Line width and the peak heights in the order they appear in the spectrum, as input. The recorded spectra were then digitized to get the signal at each and every position of the frequency marker and fed to the fitting program. The peak heights were kept as free parameters because the observed peak heights differ considerably from the expected intensities, primarily due to saturation of the

various hyperfine components [71]. Results obtained from this program for all the test studies are listed in Table II. Table II also gives the values already reported by others for comparison. It can be seen that the comparison is good. The fitted spectra of La and Nb transitions are shown in Figs. 9(b) and 10(b).

TABLE I

Observed fine structure transitions of vanadium.

Sr. No.	Wavelength (nm)	Lower Level	Upper Level	O.G. Intensity Arb. Units
1	578.62	$z^4G_{7/2}^o$	$f^4F_{5/2}$	2
		$z^4G_{9/2}^o$	$f^4F_{7/2}$	
2	587.94	$y^6F_{11/2}^o$	$e^6G_{11/2}$	5
3	601.79	$a^4P_{3/2}$	$y^4D_{3/2}^o$	8
4	605.44	$b^2G_{9/2}$	$t^4D_{7/2}^o$	-5
5	606.34	$a^4H_{7/2}$	$x^4G_{5/2}^o$	-10
6	609.39	$a^4F_{7/2}$	$z^6G_{9/2}^o$	3
7	617.03	$a^6D_{7/2}$	$z^6F_{9/2}^o$	2
8	619.05	$a^4D_{5/2}$	$z^6P_{5/2}^o$	-2
9	619.92	$a^6D_{11/2}$	$z^6D_{9/2}^o$	5
		$a^4F_{7/2}$	$z^6F_{5/2}^o$	
10	622.45	$a^6D_{3/2}$	$z^6F_{3/2}^o$	7
11	623.32	$a^6D_{5/2}$	$z^6P_{5/2}^o$	2
12	624.28	$a^6D_{1/2}$	$z^6D_{3/2}^o$	5



TABLE II

Results of the test studies as compared with the results available  
in the literature.

Element	State	Our values		Others, values		Ref.
		A(MHz)	B(MHz)	A(MHz)	B(MHz)	
La	$5d^2 6s \ a^2 G_{7/2}$	-294.0(3)	-50(25)	-289.1	-24	3
				-300.1	-	2
La	$5d^2 6p \ y^2 G_{7/2}^o$	79(3)	53	73.945	74	1
				88(4)	-	2
Nb	$4d^3 5s^2 \ a^4 P_{5/2}$	341.3(10)	-122.2	343.1670	-80.45	3
Nb	$4d^4 5p \ z^4 P_{3/2}^o$	-145.1(10)	-17.3	-137.9	-30.9	3

## CHAPTER IV

### FINE AND HYPERFINE STRUCTURE OF SCANDIUM

#### 4.1 INTRODUCTION

Fine structure studies on Scandium were first reported by Russell and Meggers [72,73]. From these results and some unpublished work of Russell, Moore [23] tabulated the Sc I atomic energy levels. The work was extended by Garton et al. [74], Neufeld et al. [75], and Ben Ahmed and Verges [76,77] to include the spectral lines observed in ultra-violet and infra-red. Racah's theoretical calculations [78] showed that Russell and Meggers had assigned one extra  $^2P$  term to the  $3d4s4p$  configuration. He suggested that this extra term might belong to  $4s^24p$  configuration rather than  $3d^24p$ . Roth [79] reported theoretical calculations for the  $(3d + 4s)^24p$  configurations and compared his results with the experimental data.

Hyperfine structure of  $a^2D_{3/2}$  and  $a^2D_{5/2}$  in the ground state configuration  $3d4s^2$  of scandium was first studied by Fricke et al. [24] using atomic beam magnetic resonance method. More accurate measurements for the same levels were reported by Childs [25]. He determined the off diagonal effects in hfs of ground state multiplet and compared his results with the theoretical predictions of Bauche-Arnoult [26]. Off diagonal hfs

studies on the ground state  $3d4s^2\ ^2D_{3/2}$  were also reported by Gebauer et al. [27]. Later on Zeiske et al. [28] used a dye laser to populate  $3d^24s\ ^4F_{5/2,7/2}$  metastable states to study hfs by ABMR method. In 1976 Ertmer and Hofer [29] reported studies on hfs of seven transitions of scandium using laser induced fluorescence combined atomic beam RF resonance.

We studied optogalvanic spectrum of scandium in the range 565 - 625 nm, 24 transition belonging to the first spectrum of Sc were observed. Hyperfine structure of seven transitions studied, is reported [30]. A and B constants for nine levels belonging to the configurations  $3d^24s$  and  $3d^24p$  are reported. Out of these, we believe, five levels are reported for the first time.

## 4.2 EXPERIMENTAL DETAILS

Scandium has large number of metastable states belonging to the configurations  $3d4s^2$ ,  $3d^24s$ ,  $3d^3$ . During the sputtering process or evaporation process all these states are populated to some extent. Therefore, each of these levels is weakly populated, making the study of these levels and transitions originating from these states difficult. To solve this problem Zeiske et al. [28], employed optical pumping method to selectively populate the levels and then applied ABMR method to study hyperfine structure. We made use of the optogalvanic detection method which is very sensitive to detect even the small number of atoms in a particular state.

Experimental setup used for the fine structure studies

reported here is as shown in Fig. 1. An argon ion laser pumped standing wave cw dye laser (Spectra Physics USA - 375) was used, which was continuously tuned by a half rpm synchronous motor over the entire dye range. The peak power given by this laser was 100 mW. It was not possible to use wavemeter in this setup because line width of this dye laser was more than 20 GHz, the maximum wave meter can handle. Therefore a double monochromator (Spex - 1402), tuned to known neon line was used to identify these lines. During all the experiments two types of lamps (Instrumentation Laboratory Inc., USA, and Westing House Electric Corporation, USA) were used. Lamp was generally operated around 10-15 mA. Laser beam was chopped at a frequency in the range 350 - 600 Hz to facilitate phase sensitive detection. Chopping frequency was adjusted to get minimum noise.

For hyperfine structure measurements the experimental setup used is as shown in Fig. 7. A wavemeter (Burleigh - WA20) was used to select the transition of interest. Frequency calibration was achieved by recording the transmission peaks of a 300 MHz FSR Fabry-Perot interferometer. The maximum power of the laser was usually around 50 mW.

#### 4.3 RESULTS AND DISCUSSION

Figure 11 shows a part of the observed scandium / neon optogalvanic spectrum. Some of the strong Neon lines were identified and used for calibration of the whole spectrum.

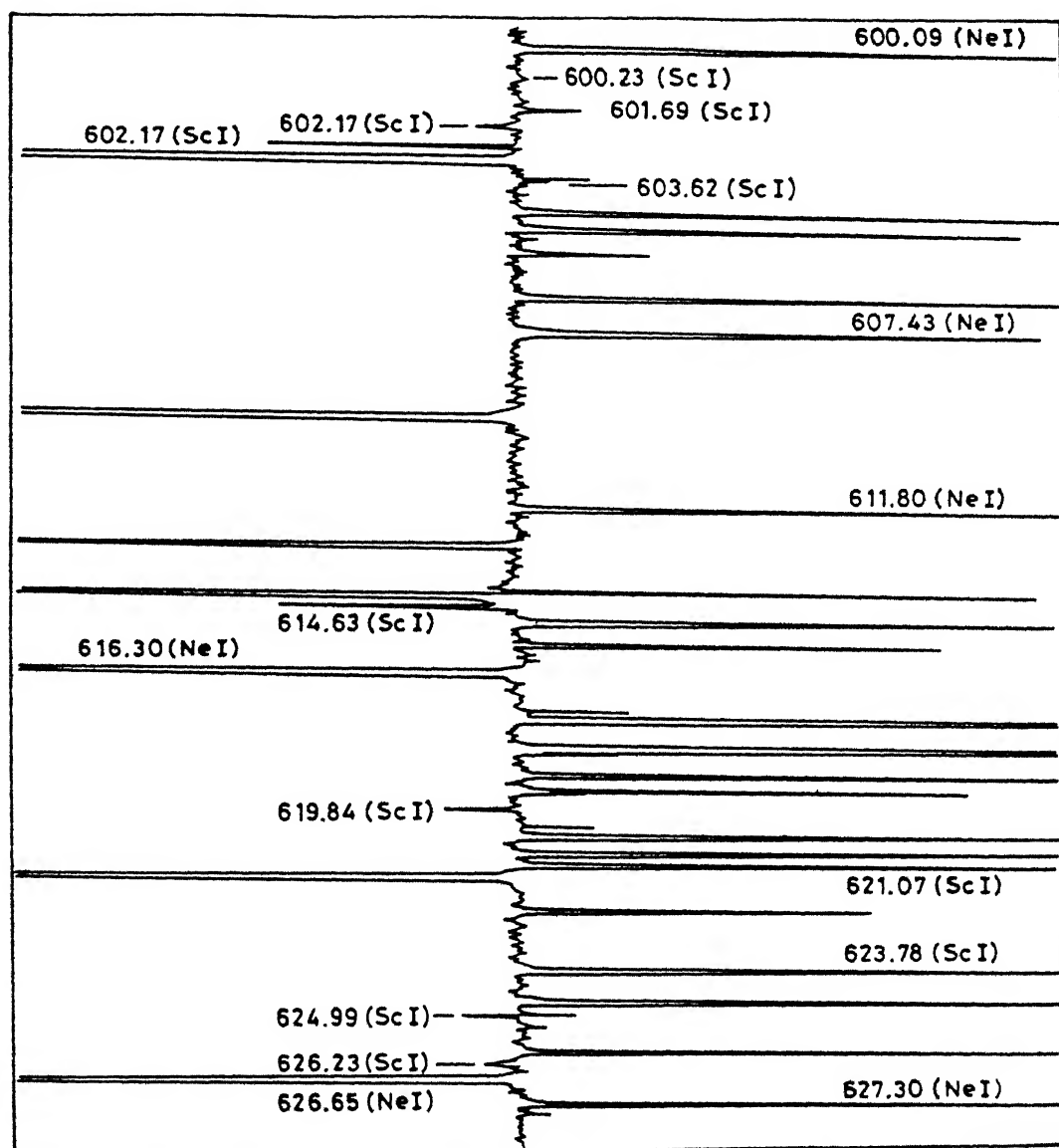


**Fig. 11.** Fine structure spectrum of scandium.

Scandium lines were identified by interpolation. Observed Scandium transitions are listed in Table III along with their relative optogalvanic intensities. It can be seen from Table III that both types of transitions i.e. giving rise to either an increase or a decrease in discharge impedance, are observed; typical of any optogalvanic spectrum. Lines marked with \* are calculated using the energy levels compiled by Moore [23]. Level assignments are either taken from [80] or are calculated from the levels given in [23].

Hyperfine structure of seven transitions, marked with \$ in Table III, was studied. Figure 12 shows a part of the fine structure diagram of scandium and the transitions for which hfs is studied. Figures 13(a) to 16(a) show typical recorded spectra of various scandium transitions. Figures 13(b) to 16(b) show the computer fitted spectra of the same transitions and the hfs energy level scheme of these transitions is shown in Figs. 13(c) to 16(c). Lower part of each figure showing the level scheme shows all the hfs components along with their relative intensities as given by eqn. 13 and 14. Most of the hfs spectra are well resolved even with the Doppler limited resolution. This is mainly because of the large nuclear magnetic dipole moment of Scandium and due to smaller Doppler width of the spectral lines of the atoms sputtered in a discharge.

Recorded spectra were analyzed using the Casimir formula [16] given by eqn. 12. Spectra were analyzed as described in section 3.6 in chapter III. It can be seen from Table III that

CENTRAL LIBRARY

112548  
Acc. No. A. 112548

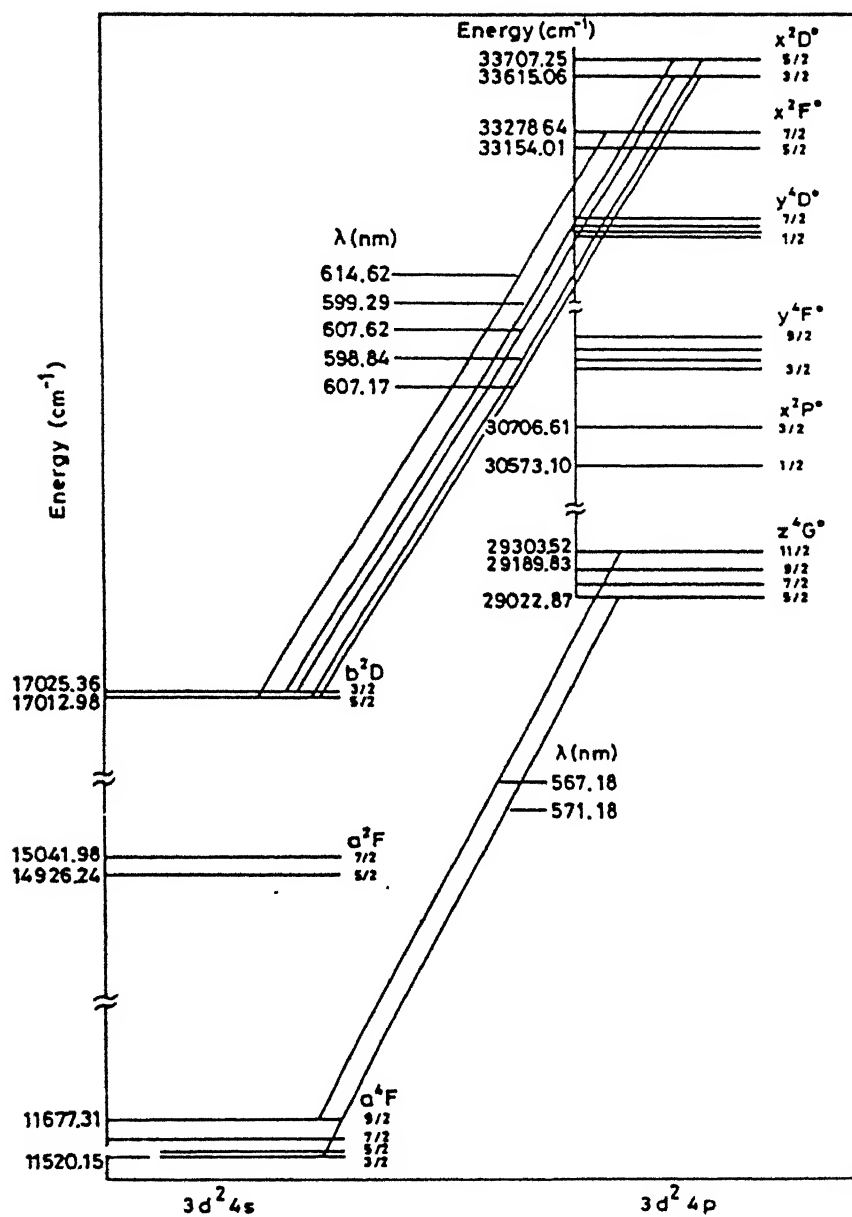


**Fig. 12.** A part of the energy level diagram of scandium, showing the transitions studied.

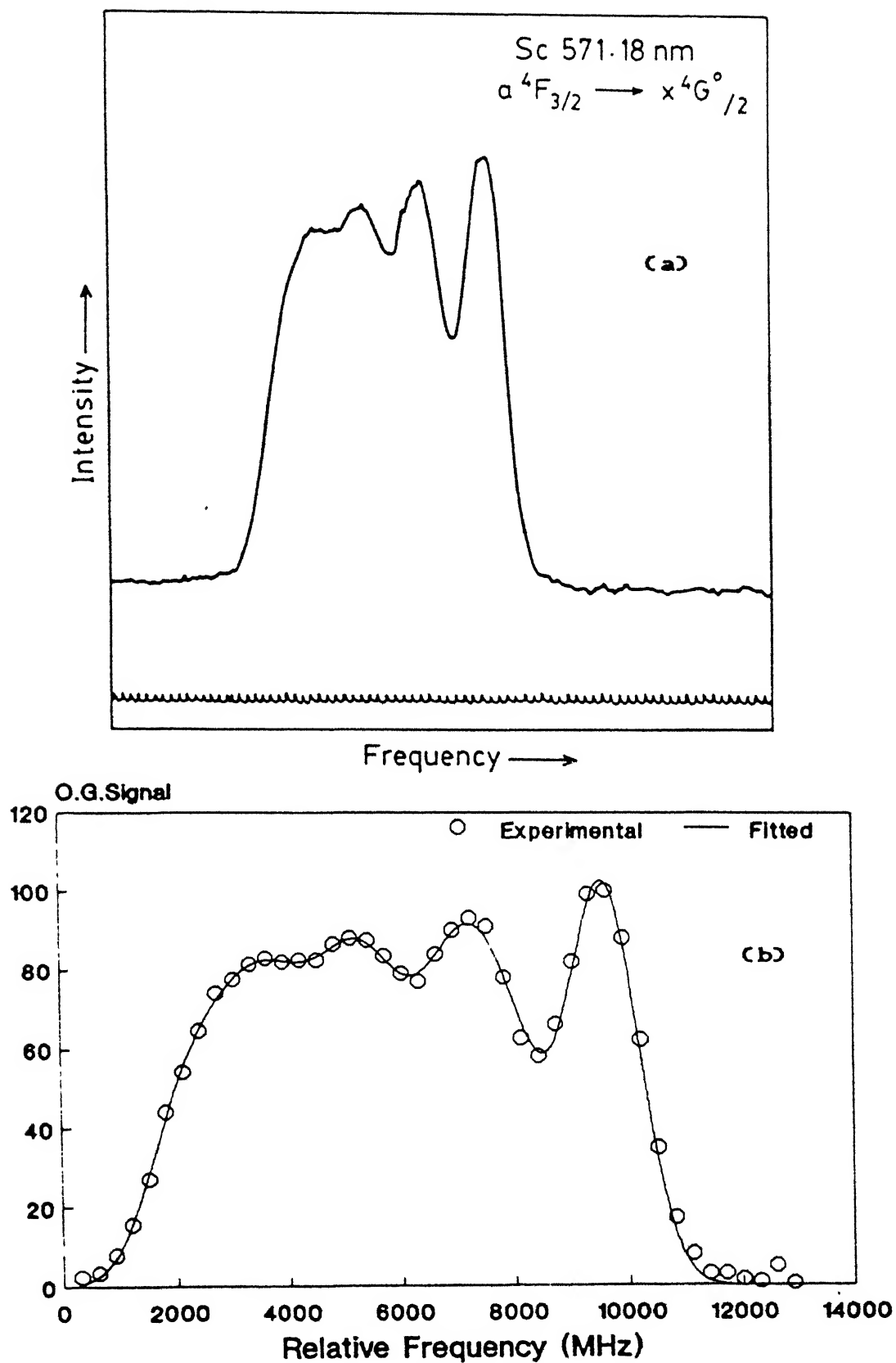


**Fig. 13.** Hyperfine structure of scandium transition at 571.20 nm. (a) recorded spectrum (b) computer fitted spectrum.



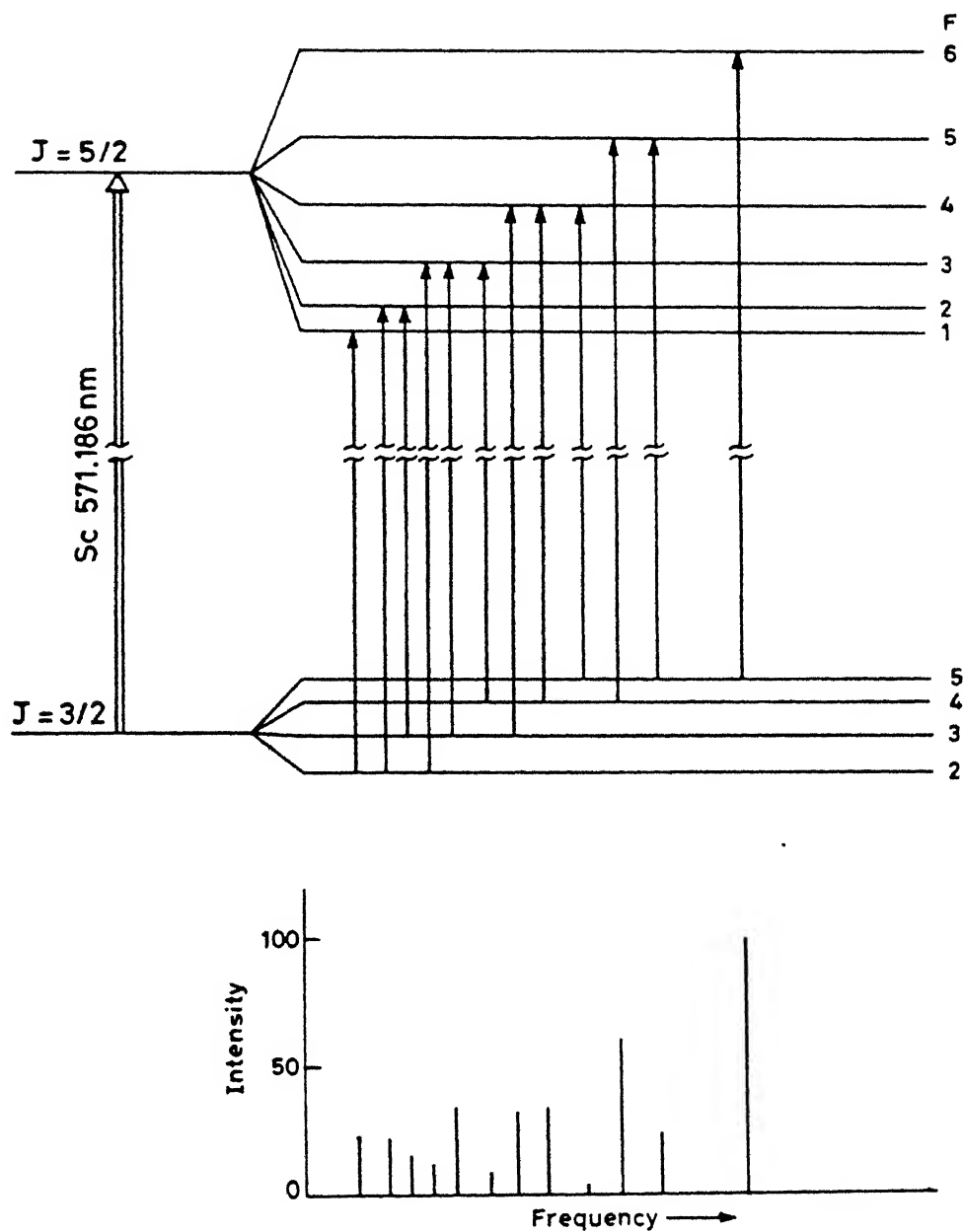
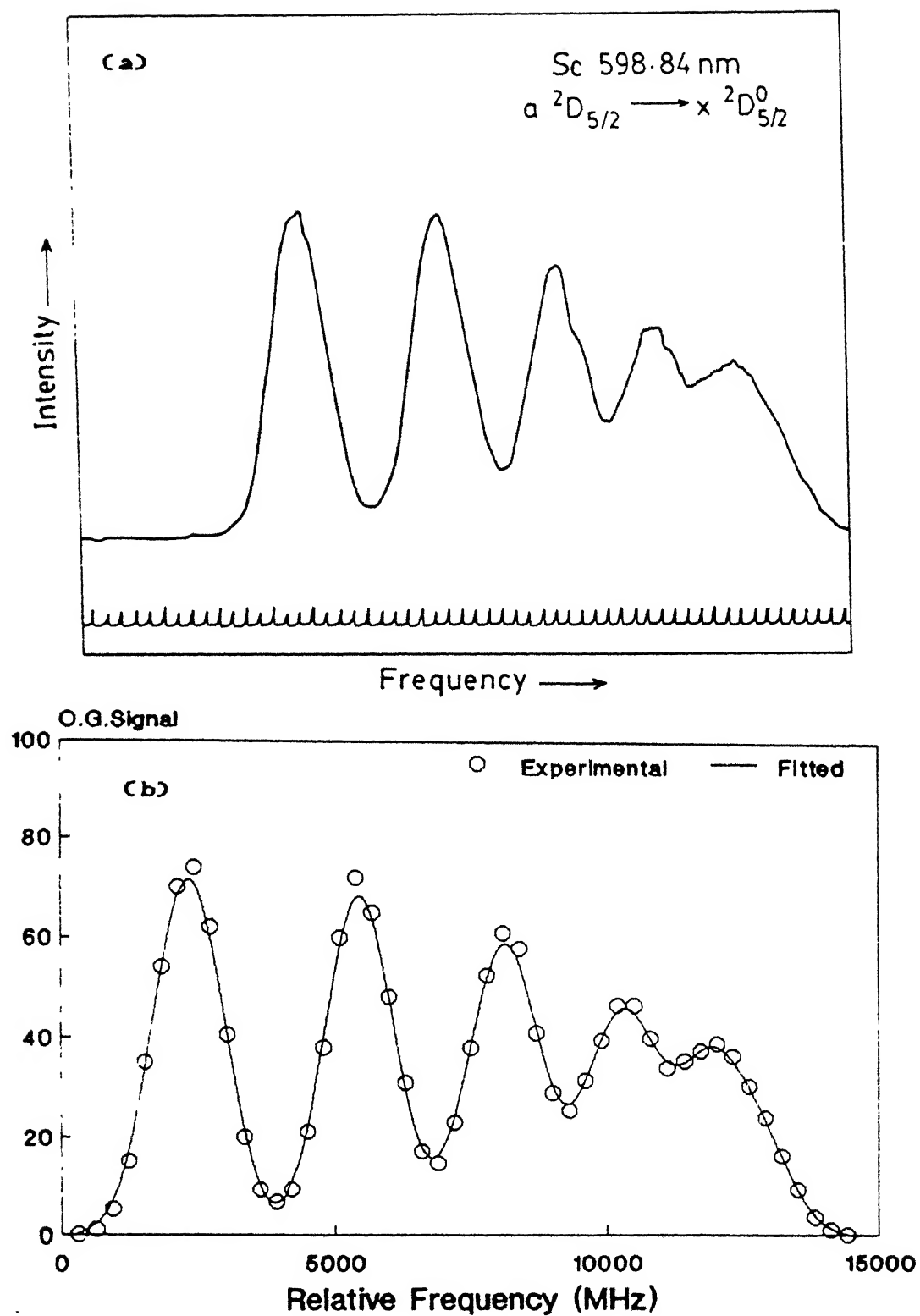
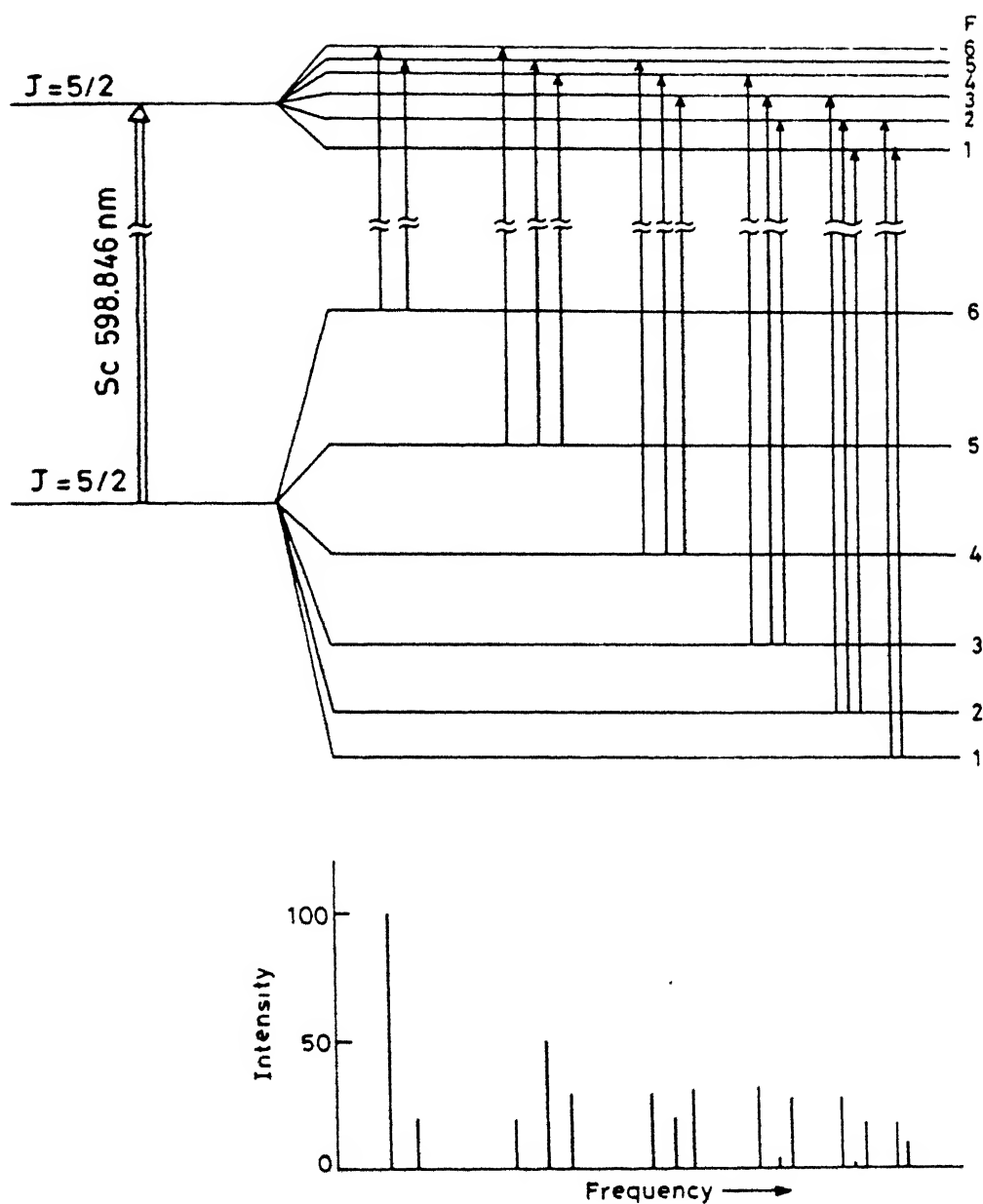


Fig. 13(c) Hfs energy level scheme of the scandium transition at 571.186 nm. Lower part of the Figure shows all the hfs components along with their relative intensities.



**Fig. 14.** Hyperfine structure of scandium transition at 598.84 nm.  
 (a) recorded spectrum (b) computer fitted spectrum.



**Fig. 14(c)** Hfs energy level scheme of the scandium transition at 598.84 nm. Lower part of the Figure shows all the hfs components along with their relative intensities.

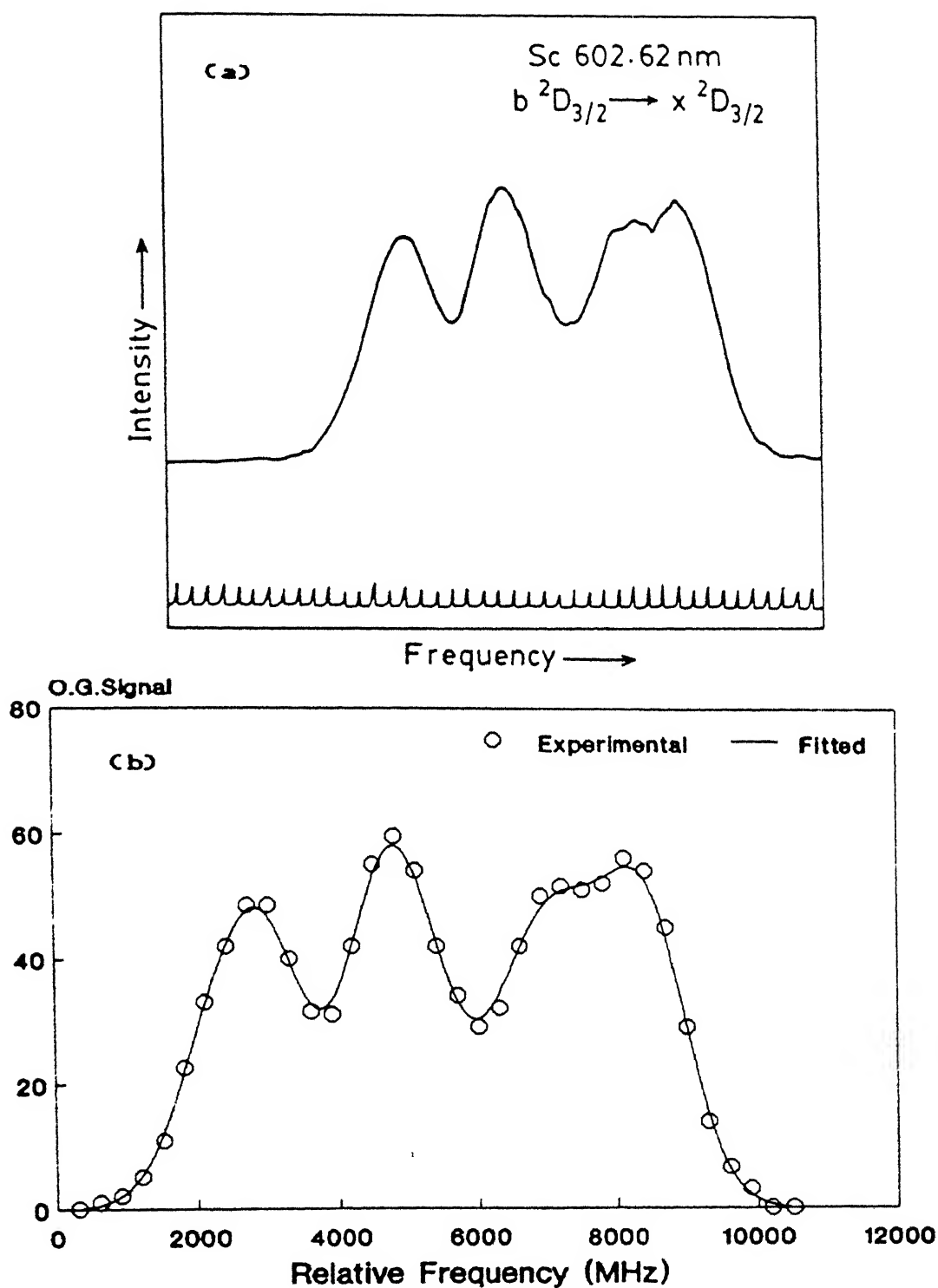


**Fig. 15.** Hyperfine structure of scandium transition at 602.62 nm.  
 (a) recorded spectrum (b) computer fitted spectrum.

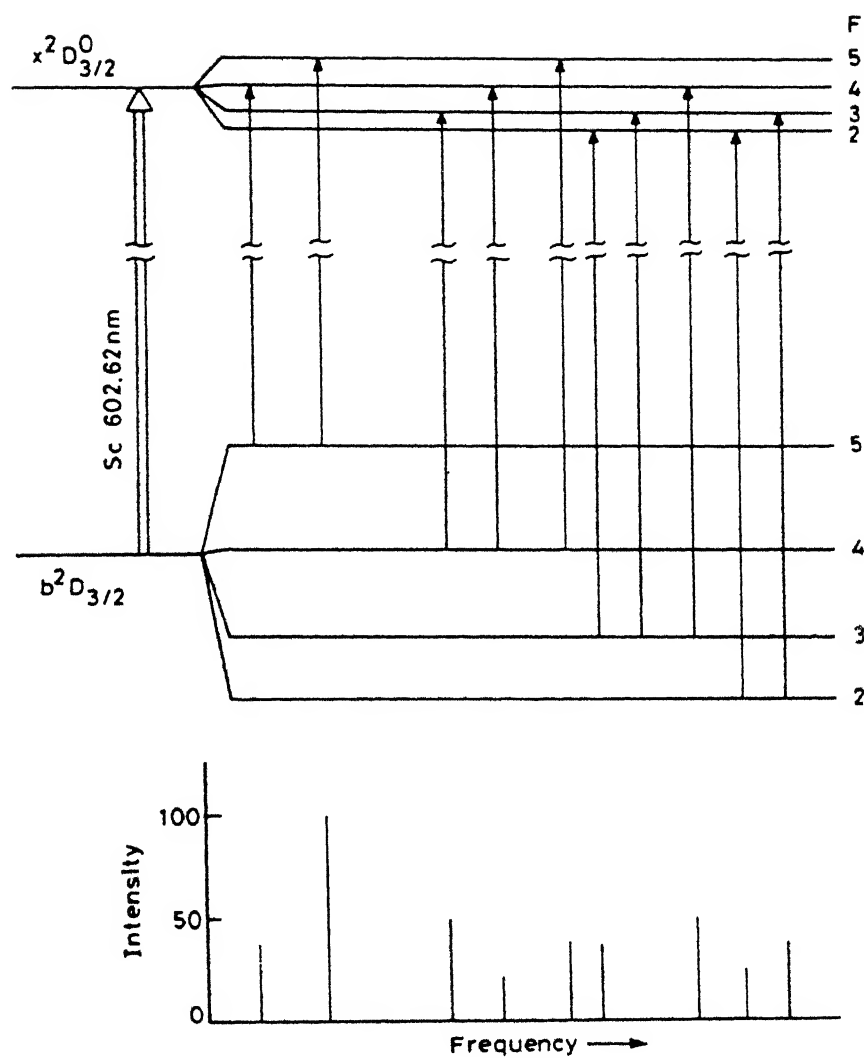


**Fig. 15(c)** Hfs energy level scheme of the scandium transition at 602.62 nm. Lower part of the Figure shows all the hfs components along with their relative intensities.

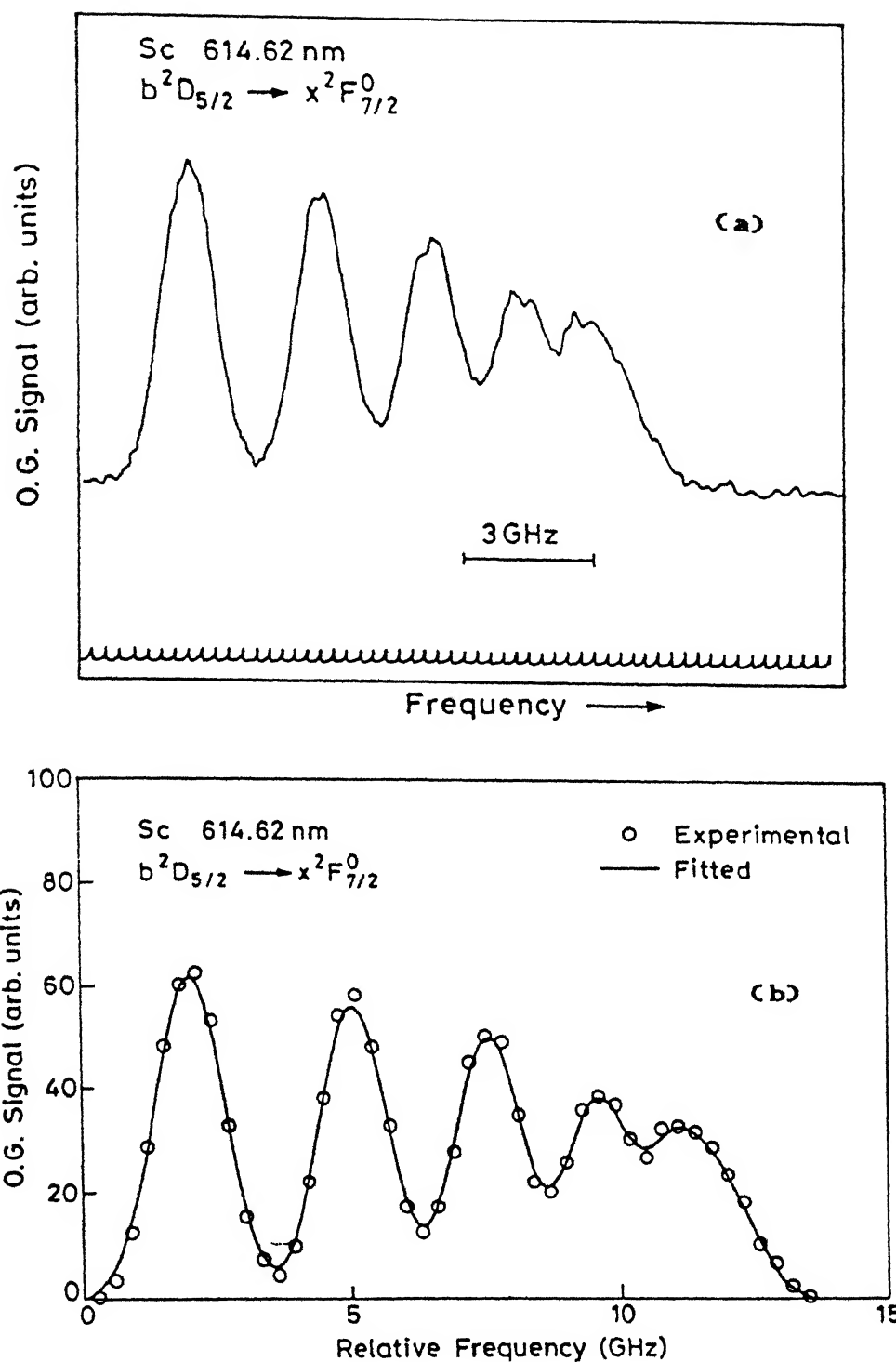


**Fig. 16.** Hyperfine structure of scandium transition at 614.62 nm.  
 (a) recorded spectrum (b) computer fitted spectrum.

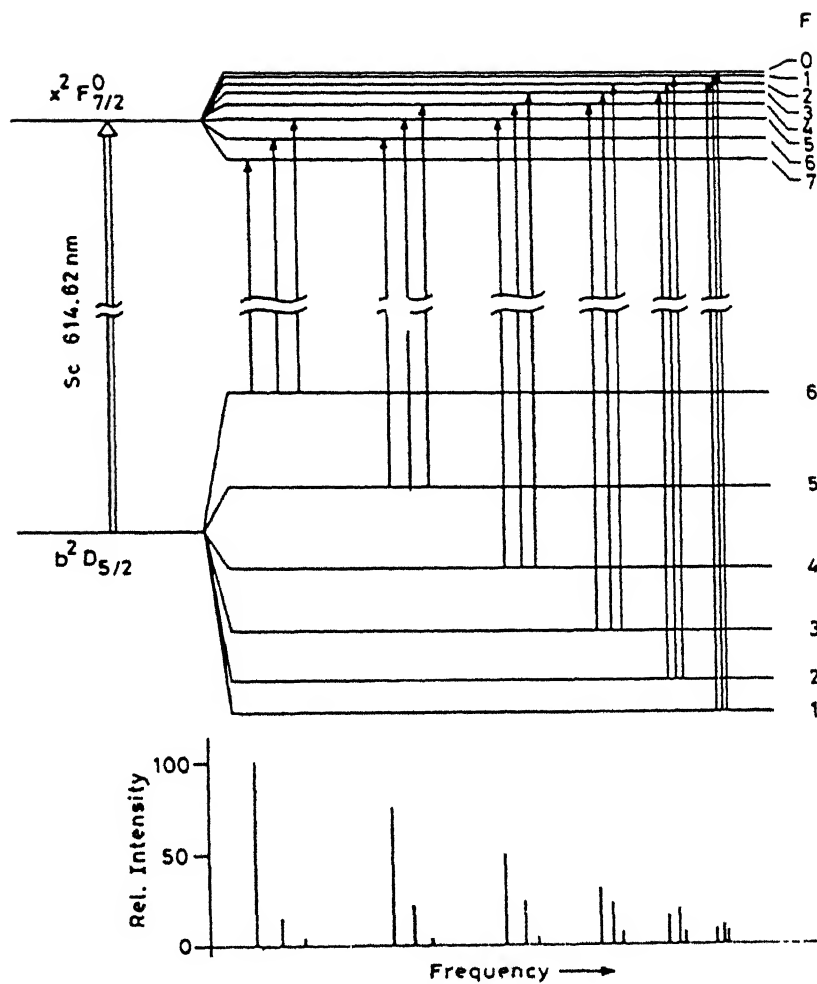


Fig. 16(c) Hfs energy level scheme of the scandium transition at 614.62 nm. Lower part of the Figure shows all the hfs components along with their relative intensities.

many of the reported transitions correspond to  $\Delta J = 0$ . For such transitions it is not possible to assign the A and B constants uniquely, because as can be seen from eqn. 14 that when  $\Delta J = 0$ , the corresponding transitions with  $\Delta F = +1$  and  $\Delta F = -1$  have the same intensity. So, if we interchange these corresponding  $\Delta F = +1$  and  $\Delta F = -1$  transitions, we get another set of A's and B's. This new set is related to the previous one. If we interchange the upper and lower level constants and change their signs we will get the other set. Therefore, if constants of one of the levels are known, either from the study of some other transition with one common level or is studied by techniques like ABMR, that of the other can be calculated uniquely. In our case all such transitions were cross checked by studying transitions with common levels.

Calculated A and B constants are given in Table IV. Already reported values, wherever applicable, are also given for comparison. It is obvious from Table II that our values compare well with those given by others. It can be seen from Table III that levels  $b^2D_{3/2}$  and  $b^2D_{5/2}$  are participating in more than one transition. In all these cases the average values from all such calculations are reported. Transitions at 598.84 nm and 602.62 nm are  $\Delta J = 0$  transitions. All such transitions were cross checked by studying other transitions with common levels.

The transition at 602.15 nm is not very well resolved. Its recorded spectrum is shown in Fig. 17(a). It is not possible to extract accurate values of A and B parameters from this spectrum alone. But as can be seen from Table I, the level  $b^2D_{5/2}$



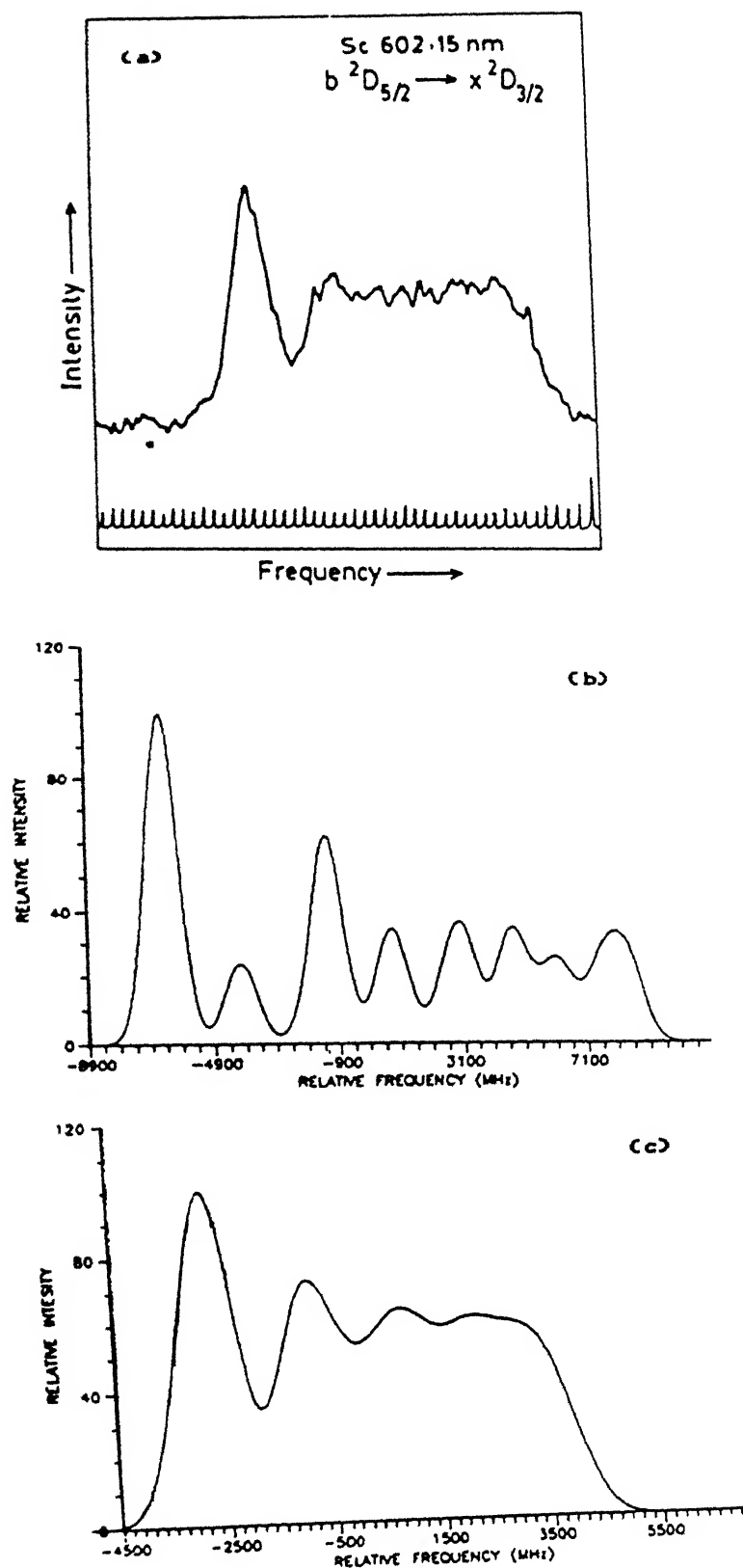


Fig. 17. Hyperfine structure of scandium transition at 602.15 nm. (a) recorded spectrum (b) and (c) generated spectra using two different sets of A and B constants.

is common to the transitions at 598.84, 602.15 and 614.62 nm and  $x^2D_{3/2}$  is common to those at 602.15 and 602.62 nm. The constants of the level  $b^2D_{5/2}$  are uniquely determined by the transition at 614.62 nm and are used in the analysis of the transitions at 602.15 and 598.84 nm. The spectrum of the transition at 602.62 being a  $\Delta J = 0$  transition, can be explained by two sets of the A and B constants namely (i)  $A_L = 596.8$ ,  $B_L = -55$ ,  $A_U = 149.2$ , and  $B_U = 100$  MHz and (ii)  $A_L = -149.2$ ,  $B_L = -100$ ,  $A_U = -596.8$ , and  $B_U = 55$  MHz. Consequently the upper level of the transition at 602.15 nm, which is common with the transition at 602.62 nm, can have two sets of values. Both of these sets were used to generate the spectrum of the transition at 602.15 nm. These spectra are shown in Figs. 17(b) and 17(c). A comparison of these spectra with that of the recorded one shows that the first set gives a spectrum which is very close to the recorded one, this fixed the upper level constants, and hence the lower level constants, of the transition at 602.62 nm. Thus even though the transition at 602.15 nm is not well resolved it helps in the analysis of the other transitions.

It was also observed that the average Doppler width of the recorded transitions is 1300 MHz which corresponds to the equilibrium atomic temperature 550 K. This low atomic temperature is due to the loss of energy during the collisions with the buffer gas atoms. That is why these spectra are well resolved even with the Doppler limited resolution.

Optogalvanic spectroscopy is well suited for high resolution studies. We have reported the hfs constants for the

nine levels in the configuration  $3d^24s$  and  $3d^24p$  of scandium. Out of this, we believe, constants for five levels are reported for the first time.

nine levels in the configuration  $3d^24s$  and  $3d^24p$  of scandium. Out of this, we believe, constants for five levels are reported for the first time.

TABLE III

Observed fine structure transitions of Sc I along with their Optogalvanic intensities and wave length in air.

Sr. No.	Wavelength (nm)	Lower level	Upper level	Intensity (arb. units)
1	567.18 <sup>\$</sup>	$a^4F_{9/2}$	$z^4G_{11/2}^o$	-
2	571.18 <sup>\$</sup>	$a^4F_{3/2}$	$z^4G_{5/2}^o$	-
3	572.41	$a^4F_{5/2}$	$z^4G_{5/2}^o$	-
4	594.53 <sup>*</sup>	$z^2P_{3/2}^o$	$e^2D_{3/2}$	saturated
5	595.79 <sup>*</sup>	$a^2P_{1/2}$	$z^4S_{3/2}^o$	3
6	596.78	$e^4D_{5/2}$	$u^2D_{3/2}^o$	77
7	596.92	$z^2F_{5/2}^o$	$g^2D_{3/2}$	-6
8	598.84 <sup>\$</sup>	$b^2D_{5/2}$	$x^2D_{5/2}^o$	-110
9	599.29 <sup>\$</sup>	$b^2D_{3/2}$	$x^2D_{5/2}^o$	3
10	602.17 <sup>\$</sup>	$b^2D_{5/2}$	$x^2D_{3/2}^o$	15
11	602.62 <sup>\$</sup>	$b^2D_{3/2}$	$x^2D_{3/2}^o$	-90
12	614.63 <sup>\$</sup>	$b^2D_{5/2}$	$x^2F_{7/2}^o$	-88
13	619.84	$b^2D_{3/2}$	$x^2F_{5/2}^o$	-27
14	621.07	$a^2D_{3/2}$	$z^2D_{3/2}^o$	saturated
15	623.98	$a^2D_{3/2}$	$z^2D_{5/2}^o$	saturated
16	624.99	$z^4P_{5/2}^o$	$e^4D_{7/2}$	20
17	626.22	$z^4P_{3/2}^o$	$e^4D_{5/2}$	-9

Table IV

Calculated A and B parameters as compared with the previously known data. Figures in parentheses are uncertainties in MHz.

Level	Energy (cm <sup>-1</sup> )	A (MHz) This Work	B (MHz) This Work	A (MHz) Others' Work [29]	B (MHz) Others' Work [29]
<b>3d<sup>2</sup>4s</b>					
a <sup>4</sup> F <sub>3/2</sub>	11520.15	-159.0(5)	-50(20)	-155	-5.16
a <sup>4</sup> F <sub>9/2</sub>	11677.31	294.3(2)	-32(23)	285.967	-15.46
b <sup>2</sup> D <sub>5/2</sub>	17012.98	425.4(4)	-0.6(30)	-	-
b <sup>2</sup> D <sub>3/2</sub>	17025.36	596.8(7)	-55(20)	-	-
<b>3d<sup>2</sup>4p</b>					
z <sup>4</sup> G <sup>o</sup> <sub>5/2</sub>	29022.87	280.5(3)	-60(30)	279.0	-
z <sup>4</sup> G <sup>o</sup> <sub>11/2</sub>	29303.52	55.0(1)	25(30)	45	-
x <sup>2</sup> D <sup>o</sup> <sub>3/2</sub>	33615.06	149.2(7)	100(25)	-	-
x <sup>2</sup> D <sup>o</sup> <sub>5/2</sub>	33707.25	-105.6(5)	2.3(20)	-	-
x <sup>2</sup> F <sup>o</sup> <sub>7/2</sub>	33278.64	-82.2(4)	-2.2(20)	-	-

## CHAPTER V

### FINE AND HYPERFINE STRUCTURE OF NIOBIUM

#### 5.1 INTRODUCTION

Since the first observation of Meggers et al. [81], in 1924, there have been several reports [82-86] on the structural analysis of niobium. The final report on the term analysis of the first and second spectrum of Niobium was published by Humphreys and Meggers in 1945 [87].

Hyperfine structure of Niobium, until now, has been studied by Ballard [88], Meeks and Fisher [89], and Murakawa [90,91], by optical methods. It was after the development of a universal evaporation technique [33,34] that ABMR method was applied to study hyperfine structure of Nb [92]. Buttegenbach, et al. [92], studied hfs of the nine levels in the multiplets  $4d^4 5s$   $^6D_{1/2-9/2}$  and  $4d^3 5s^2$   $^4F_{3/2-9/2}$ . In the next paper [32] they analyzed their data using effective operator formalism and reported a nuclear quadrupole moment = 0.36 b. Later Fraenkel, et al. [20] reported hyperfine structure studies of 17 metastable states belonging to the even parity configurations and 14 odd parity states in the high lying configurations  $4d^4 5p$  and  $4d^3 5s 5p$ .

Recently we reported hfs measurements in 12 levels [21]. Still there are lot more levels to be studied for the completion of hfs studies.

## 5.2 EXPERIMENTAL

Niobium, like any other transition element, has many metastable levels corresponding to the configurations  $4d^35s^2$ ,  $4d^45s$ ,  $4d^5$ . During the sputtering /evaporation process most of these states are populated to some extent. Moreover, niobium is one of the highly refractory metals; even at high temperatures atom density is very low. The small number of atoms thus produced are distributed among all the metastable levels. It is difficult to study these levels with the techniques like fluorescence and atomic beam magnetic resonance (ABMR). That is why, some times levels are needed to be selectively populated for the application of these techniques. However, if the detection technique is sensitive enough to detect small number of atoms in a particular state or participating in the transition starting from that state, then the population distribution becomes an advantage. Optogalvanic spectroscopy is one such technique [14,15].

Fine structure studies on Niobium were carried out using laser optogalvanic spectroscopy. The experimental setup used is shown in Fig. 1. A Niobium/Neon hollow cathode lamp (Instrumentation Laboratory Inc. USA) was used in the experiment. The lamp was operated at currents between 20-25 mA. At these



currents we could observe appreciable population of atoms not only in ground state but also in the metastable states as well. This is obvious from the signal strengths observed in the recorded optogalvanic (OG) spectra. The laser beam was chopped at a frequency around 465 Hz and OG signals were picked up across a 10k $\Omega$  ballast resistor. The spectrum was recorded over the entire dye range, 570 - 630 nm, and 39 transitions of Nb I were observed.

Figure 18 shows a part of the niobium / neon optogalvanic spectrum. Well known neon lines were identified and used for the calibration of the spectrum. A part of the energy level diagram of Nb I, along with some of the observed transitions is shown in Fig. 19. The observed transitions are listed in Table V; level are assigned based on Humphrey and Meggers [86] work.

High resolution optogalvanic spectra of niobium were recorded with an experimental setup shown in Fig. 7. The ring dye laser with a band width  $\approx$  1MHz was scanned over a range of more than 30 GHz. Most of the hyperfine structure spectra reported are within this range.

Owing to the large nuclear magnetic dipole moment and smaller Doppler width of the spectral lines, hyperfine structure patterns are fairly well resolved. Measured line width of the spectral lines was of the order of 1000 MHz from which a rough estimate of the atomic temperature was obtained to be 725 K [21]. This low atomic temperature is due to the fact that even though

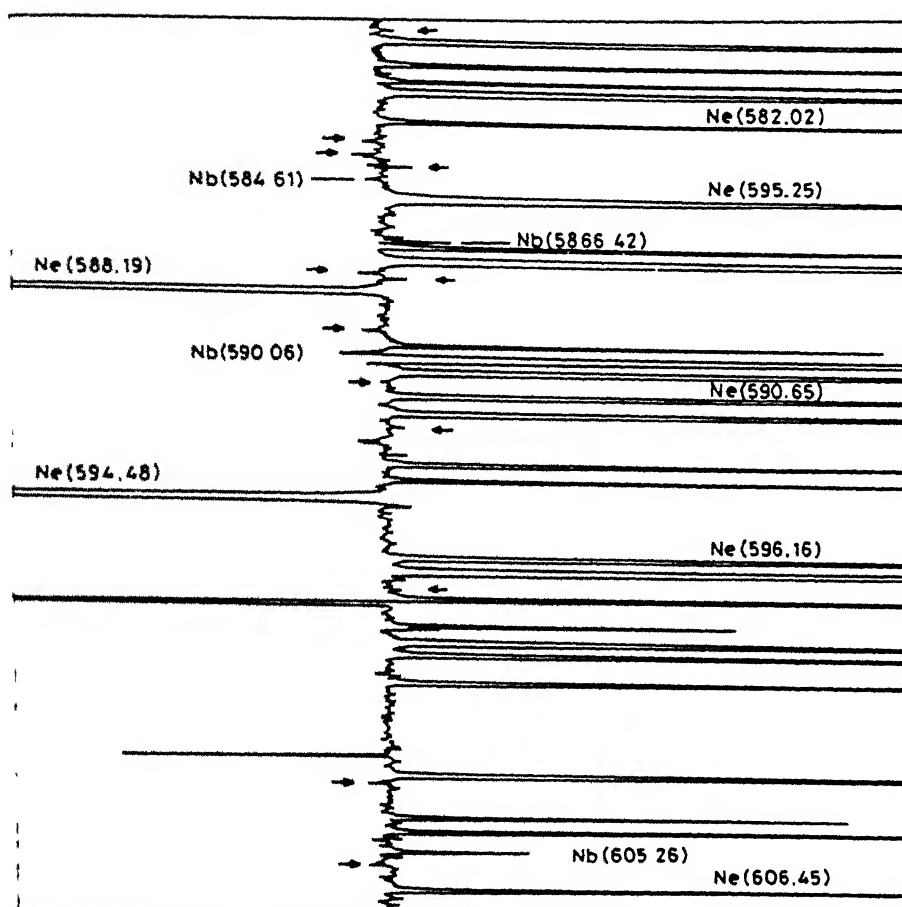


**Fig. 18.** Fine structure spectrum of niobium and neon recorded by laser optogalvanic spectroscopy.

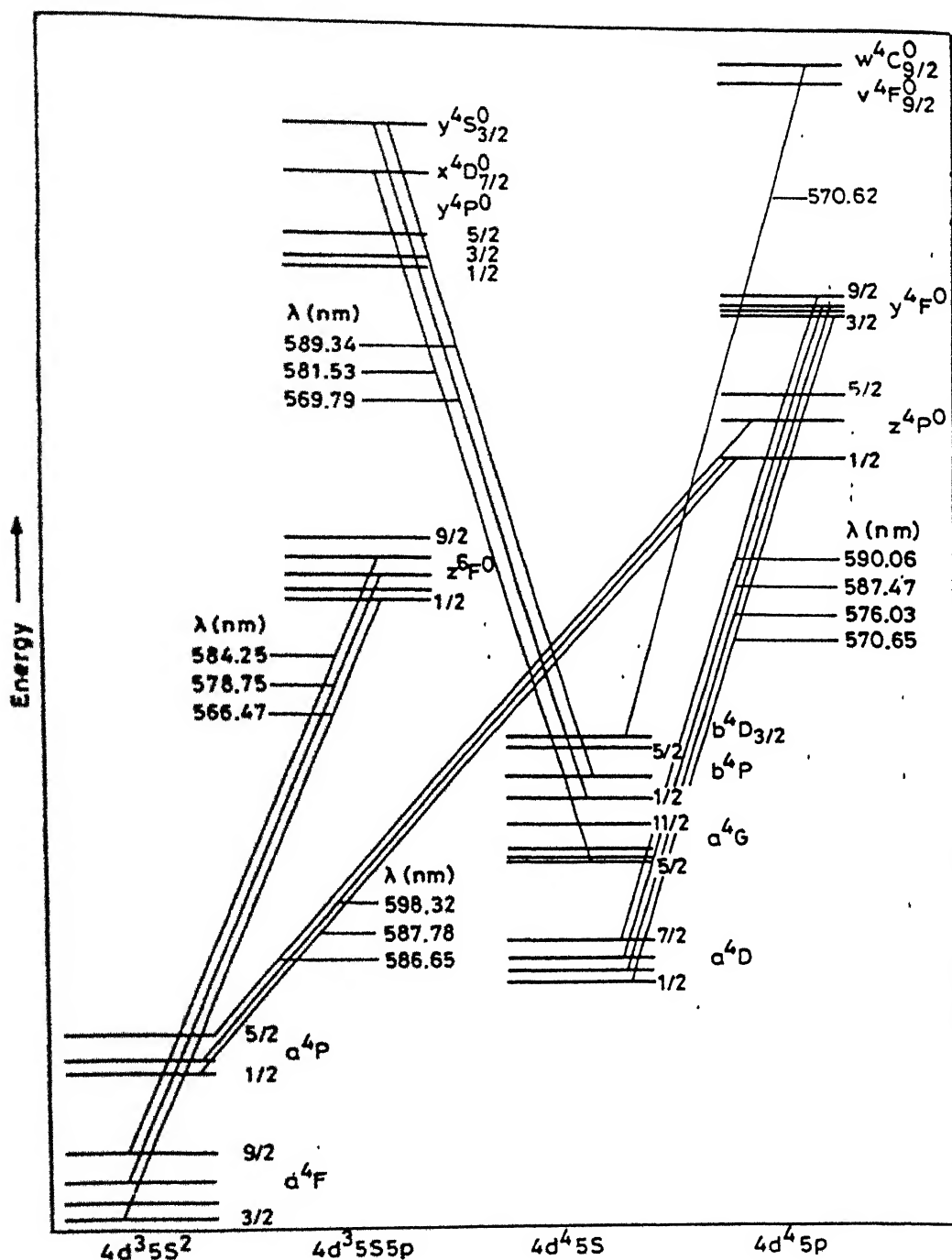


Fig. 10. A part of the energy level diagram of niobium showing the transitions studied.

these atoms are emitted with high energies, they loose energy during collisions with the buffer gas atoms, with the result their equilibrium energies are quite low.

### 5.3 RESULTS AND DISCUSSION

Table V gives the observed niobium transitions along their wavelengths in air and the relative optogalvanic intensities. Transitions of both types, giving rise to either an increase or a decrease in discharge impedance are observed, which is typical of any optogalvanic spectrum. The intensities given in Table V are not normalized to the dye laser power output. The transitions at 583.92 nm and 583.86 nm were resolved only while recording hfs spectra, otherwise we observed one broad line which appeared to be a doublet.

Hyperfine structure of 20 transitions, marked \* in Table V, was studied. Typical recorded hfs spectra are shown in Figs. 20(a) to 29(a). Figures 20(b) to 29(b) show the computer fitted spectra of the same transitions and their hfs energy level schemes are shown in Figs. 20(c) to 29(c). It can be seen that some spectra are fully resolved while others are only partially resolved. But all of them are resolved to the extent to give unambiguous values for the hyperfine constants of both the levels involved.

The recorded spectrum and the computer fitted spectrum of the transition  $a^4F_{3/2} \rightarrow z^6F_{1/2}^0$ , at 566.47 nm are shown in

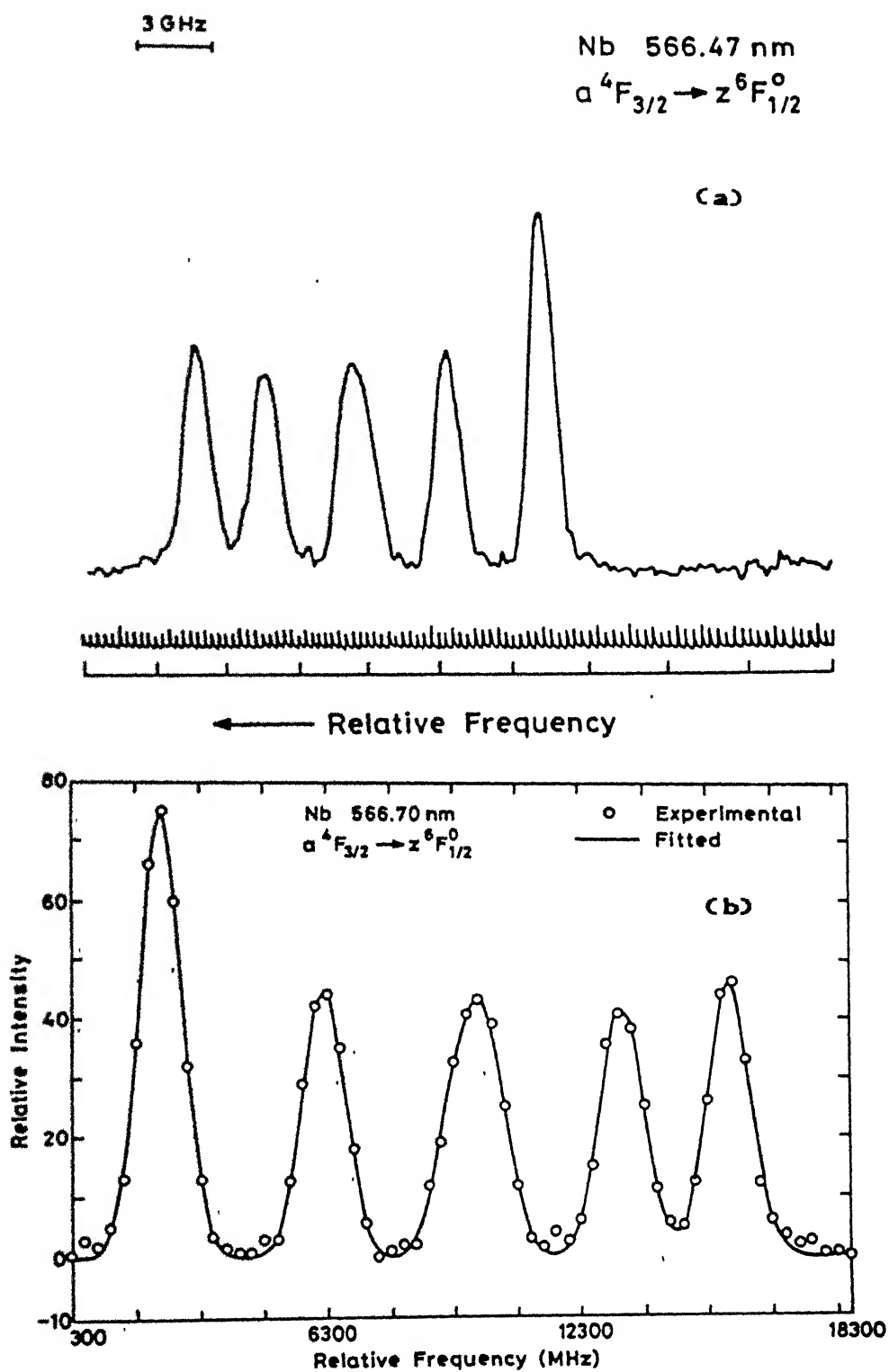


**Fig. 20.** Hyperfine structure of niobium transition at 566.47 nm.  
 (a) recorded spectrum (b) computer fitted spectrum.

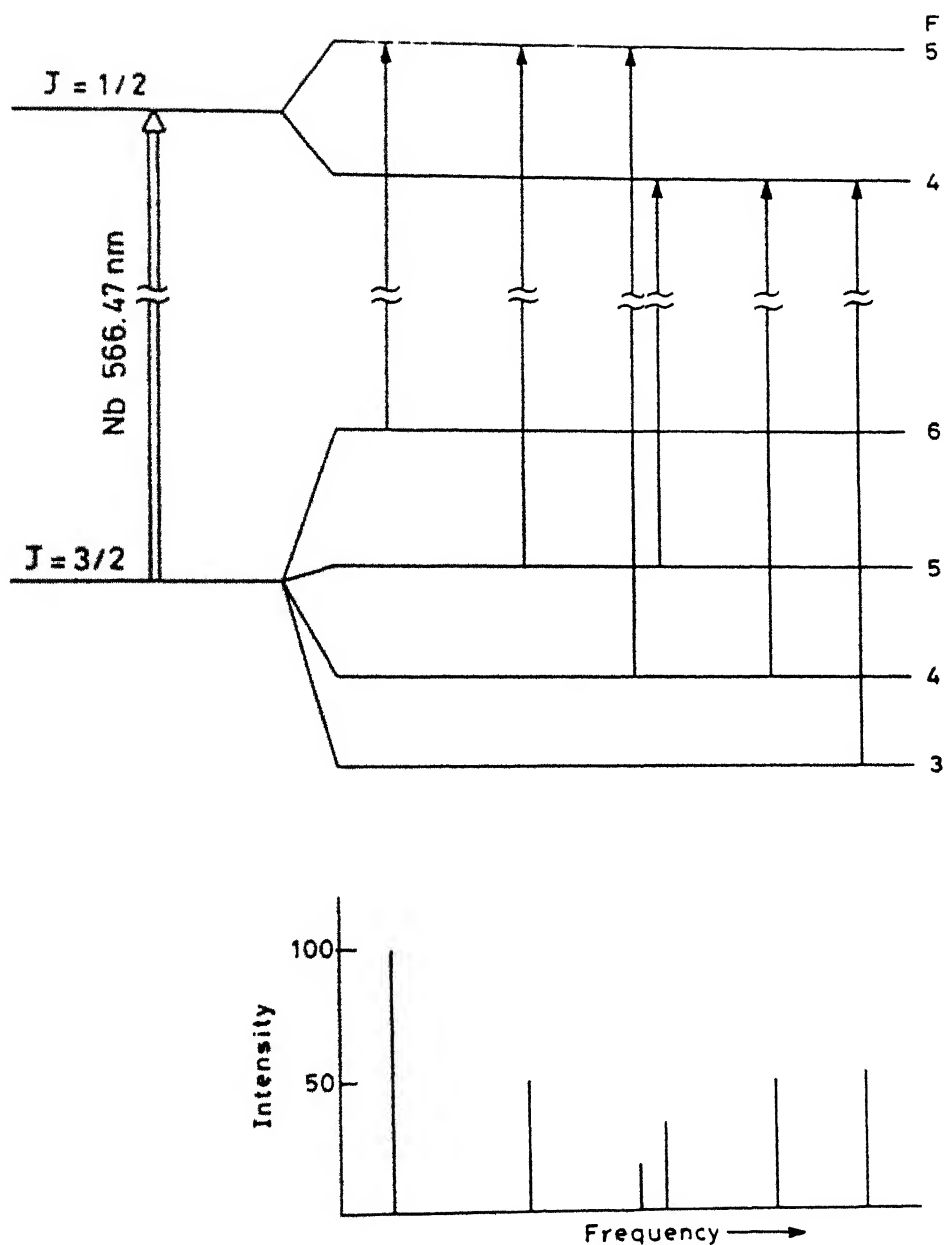


Fig. 20(c) Hfs energy level scheme of the niobium transition at 566.47 nm. Lower part of the Figure shows all the hfs components along with their relative intensities.

Figs. 20(a) and 20(b) respectively. It is obvious from the level scheme shown in Fig. 20(c) that there should be six components in all. We have observed five peaks. The central peak is a combination of two peaks. The recorded spectra of transitions ( $b^4P_{1/2} \rightarrow \gamma^4S^0_{3/2}$ ) at 569.79 nm and ( $a^4D_{1/2} \rightarrow \gamma^4F^0_{3/2}$ ) at 570.65 nm, shown in Figs. 21(a) and 23(a) respectively are fully resolved.

In Figure 21(a) only five out of six peaks of the line 569.79 nm are shown. Sixth peak, on the lower frequency (i.e. towards the left side of the spectrum) is interfering with another unknown line observed around 569.81 nm. This unknown line is not well resolved and it could not be ascertained whether this line belongs to Niobium or some other impurity present in the cathode material.

As described in the previous chapter, that for the transition with  $\Delta J = 0$ , it is not possible to give unique values of A and B parameters. In our case we cross checked all such transitions, but for one at 587.63 nm, by studying other transitions with common levels. The recorded spectrum of the transitions, ( $18332_{11/2} \rightarrow {}^2H^0_{11/2}$ ), at 587.63 nm is shown in Fig. 30(a). Figures 30(b) and 30(c) show the generated hfs spectra corresponding to the two sets of values. It can be seen that these two spectra are absolutely identical even though the hfs level structures will be totally different. It was not possible to study any other transition with one level common with the transition at 587.6 nm.

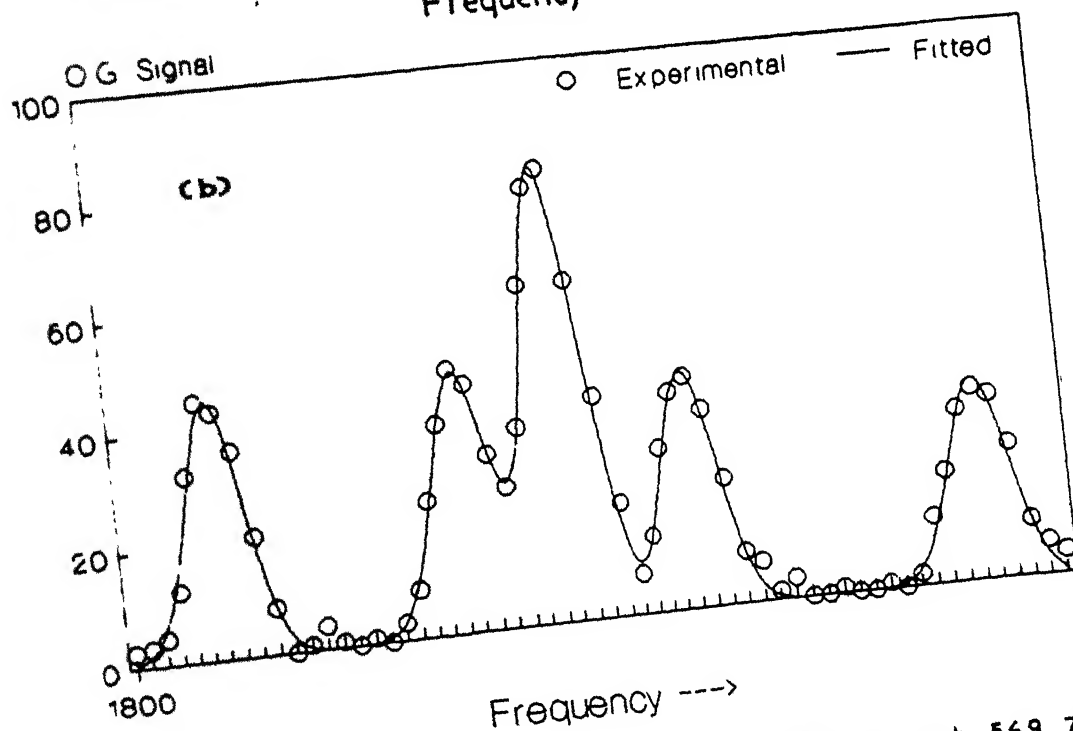
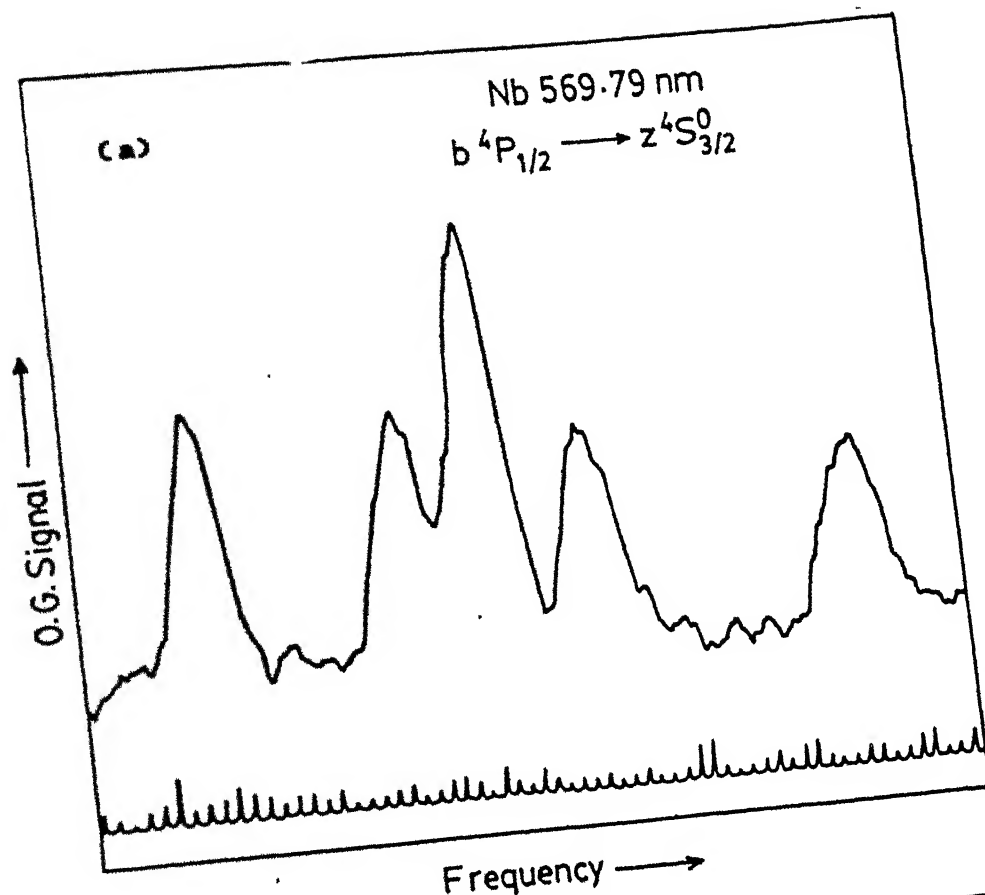
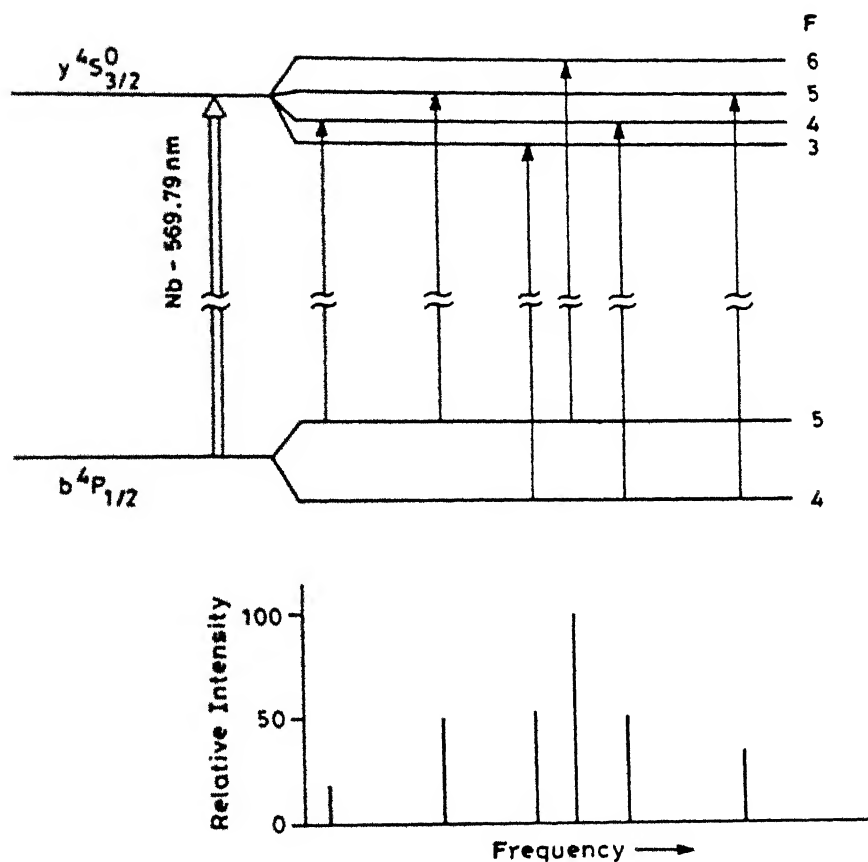


Fig. 21. Hyperfine structure of niobium transition at 569.79 nm.  
 (a) recorded spectrum (b) computer fitted spectrum.





**Fig. 21(c)** Hfs energy level scheme of the niobium transition at 569.79 nm. Lower part of the Figure shows all the hfs components along with their relative intensities.

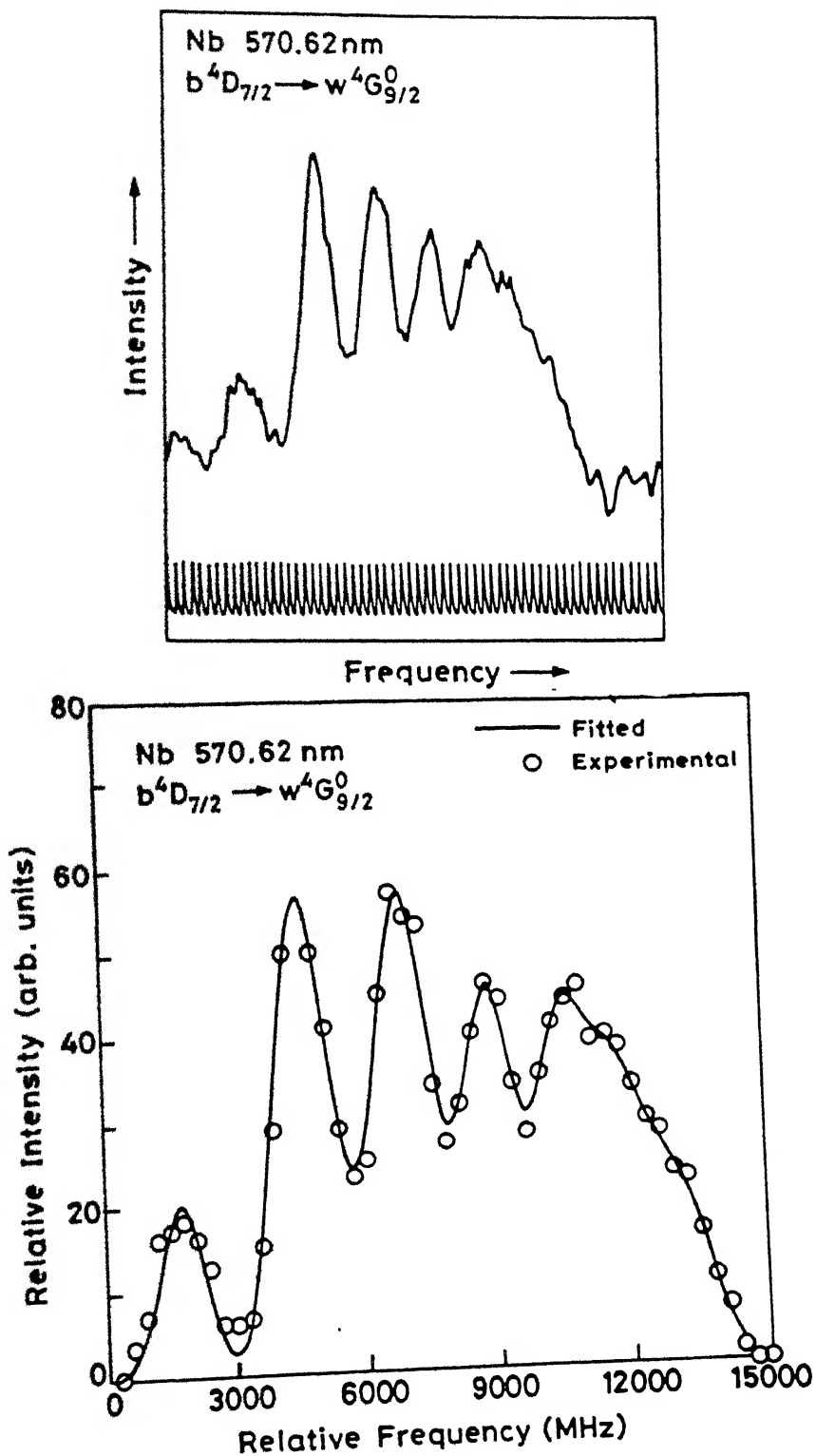


Fig. 22. Hyperfine structure of niobium transition at 570.62 nm. (a) recorded spectrum (b) computer fitted spectrum.

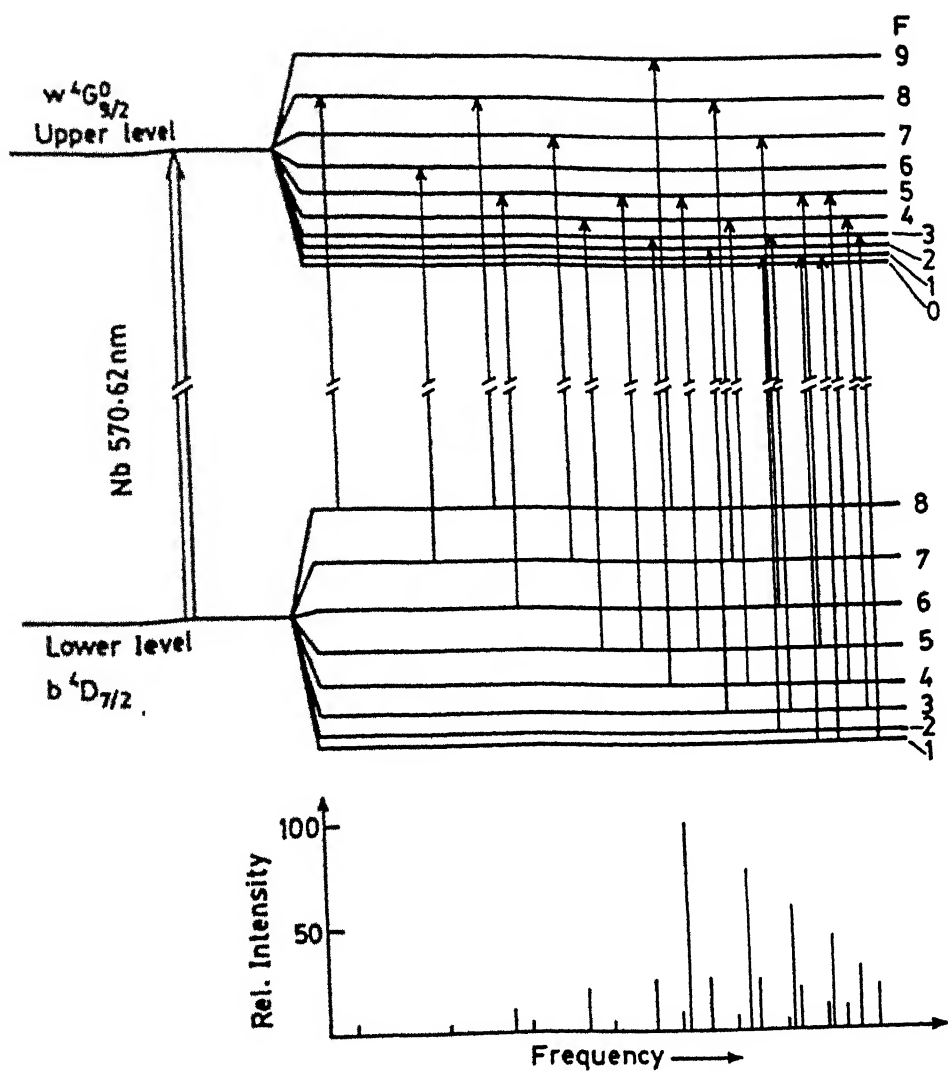
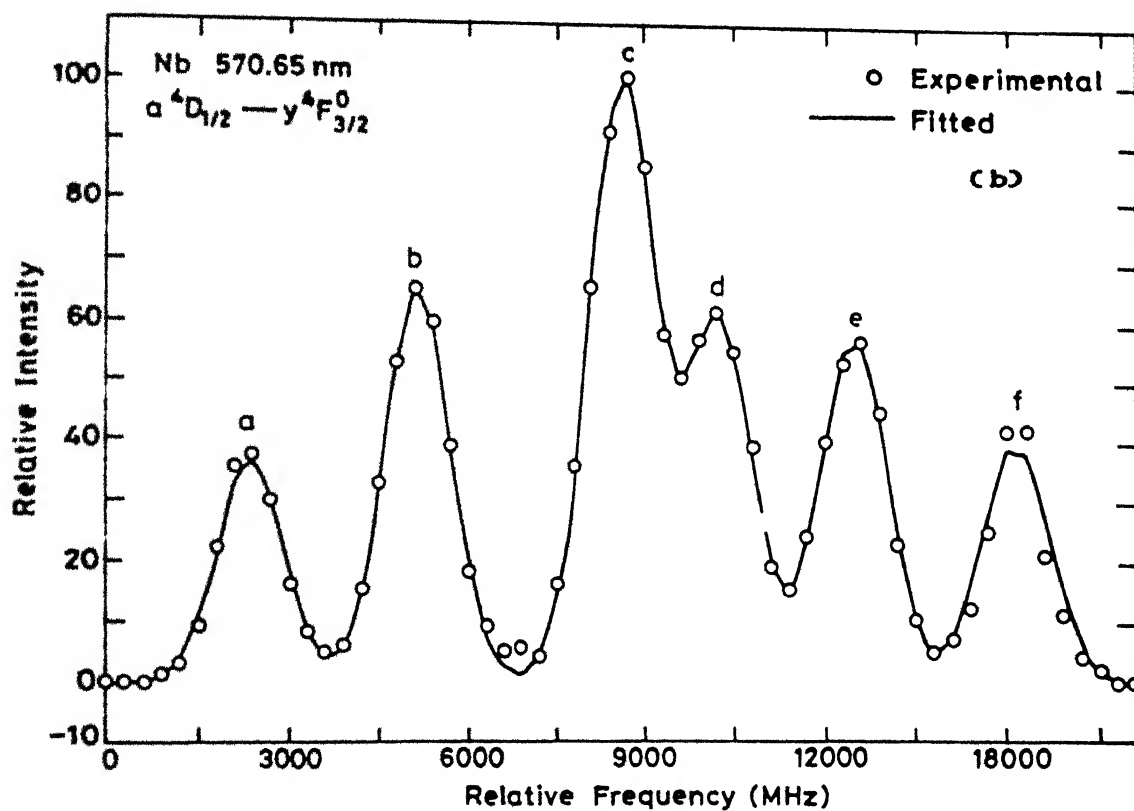
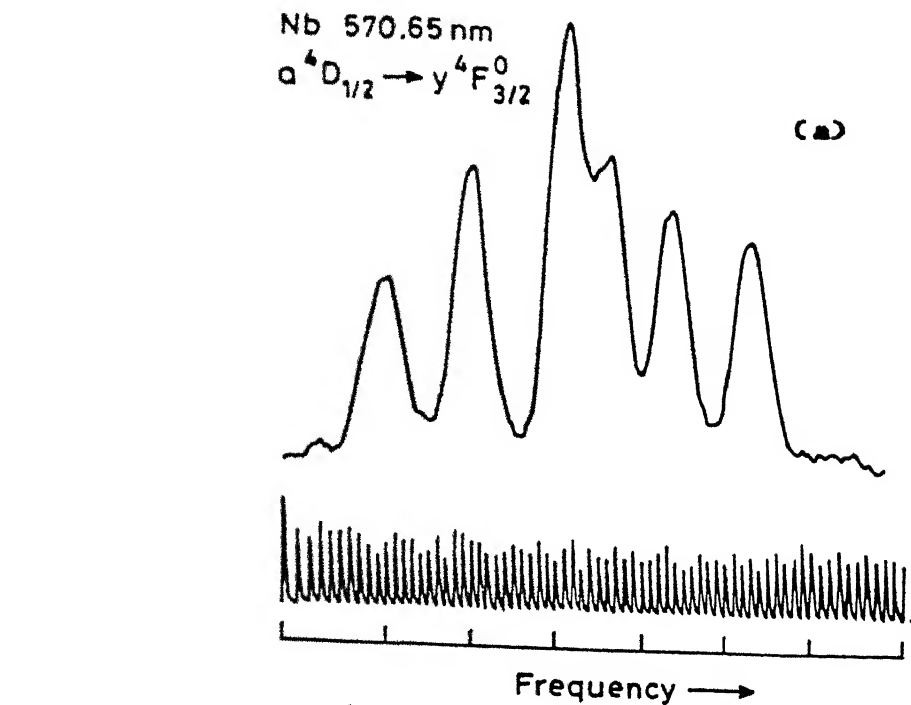


Fig. 22(c) Hfs energy level scheme of the niobium transition at 570.62 nm. Lower part of the Figure shows all the hfs components along with their relative intensities.



**Fig. 23.** Hyperfine structure of niobium transition at 570.65 nm.  
 (a) recorded spectrum (b) computer fitted spectrum.

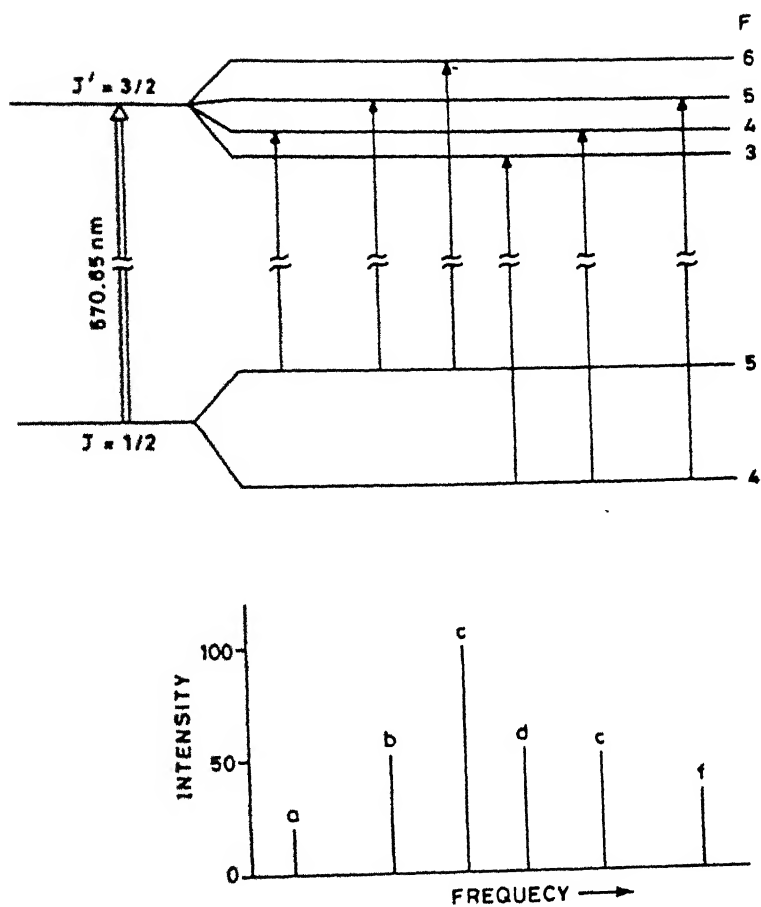
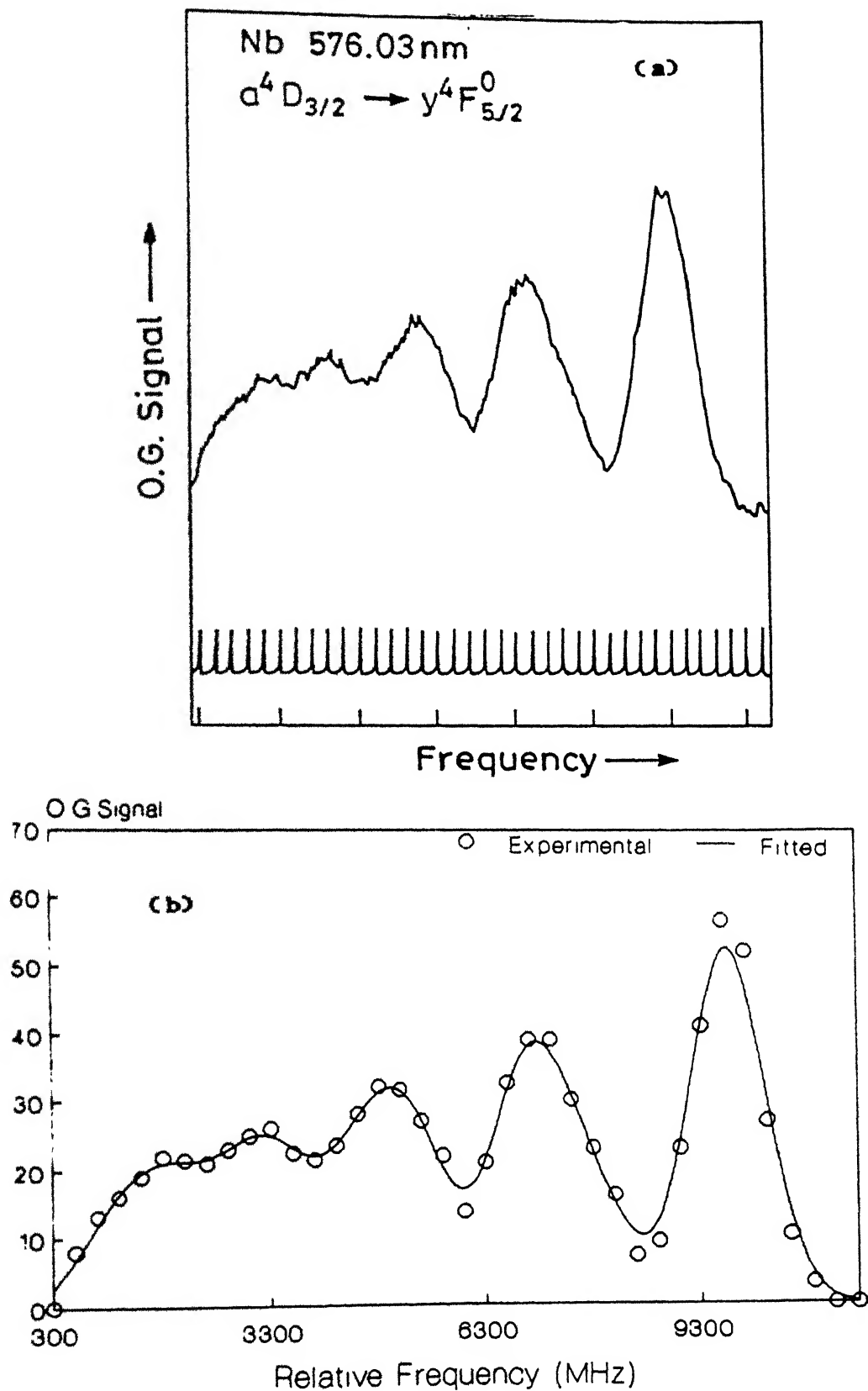


Fig. 23(c) Hfs energy level scheme of the niobium transition at 570.65 nm. Lower part of the Figure shows all the hfs components along with their relative intensities.



**Fig. 24.** Hyperfine structure of niobium transition at 576.03 nm.  
 (a) recorded spectrum (b) computer fitted spectrum.

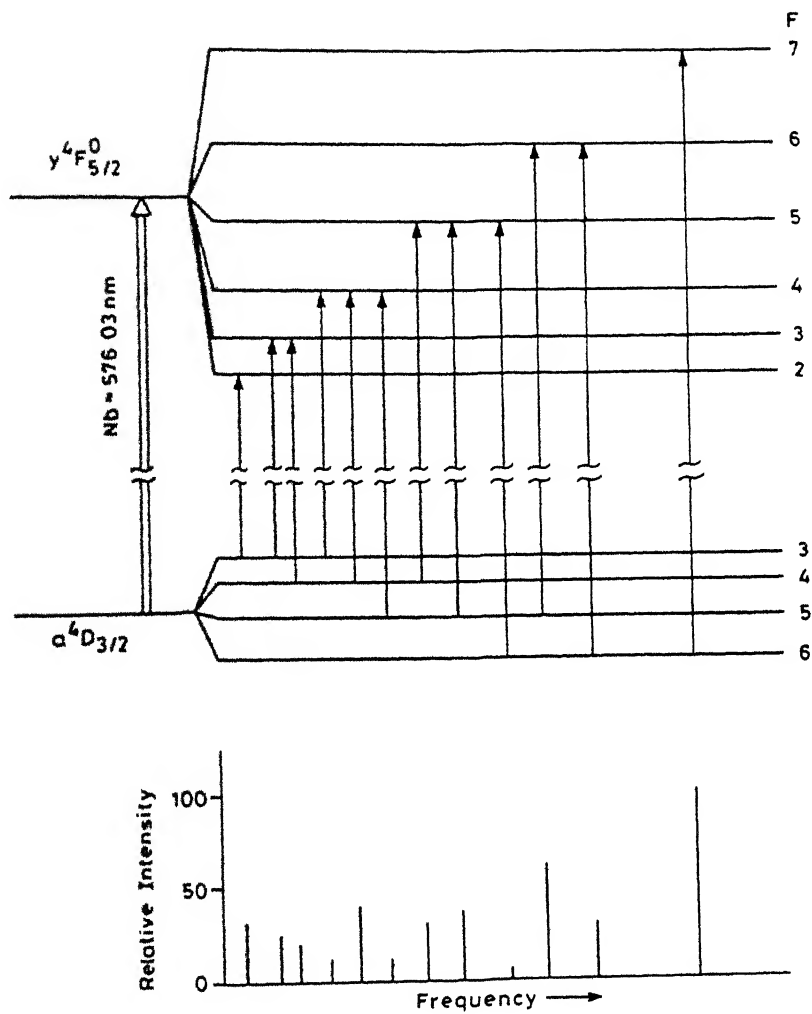
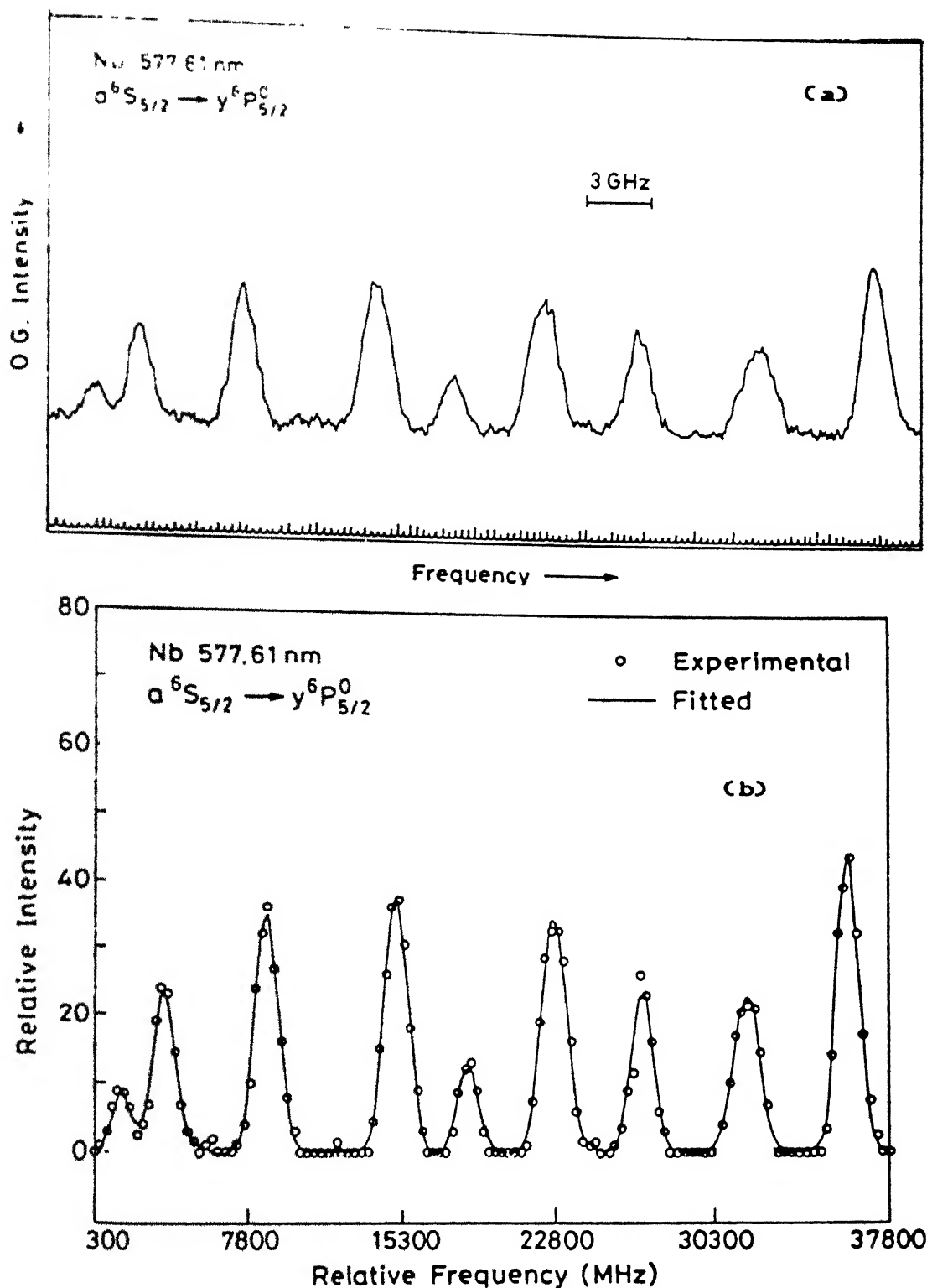
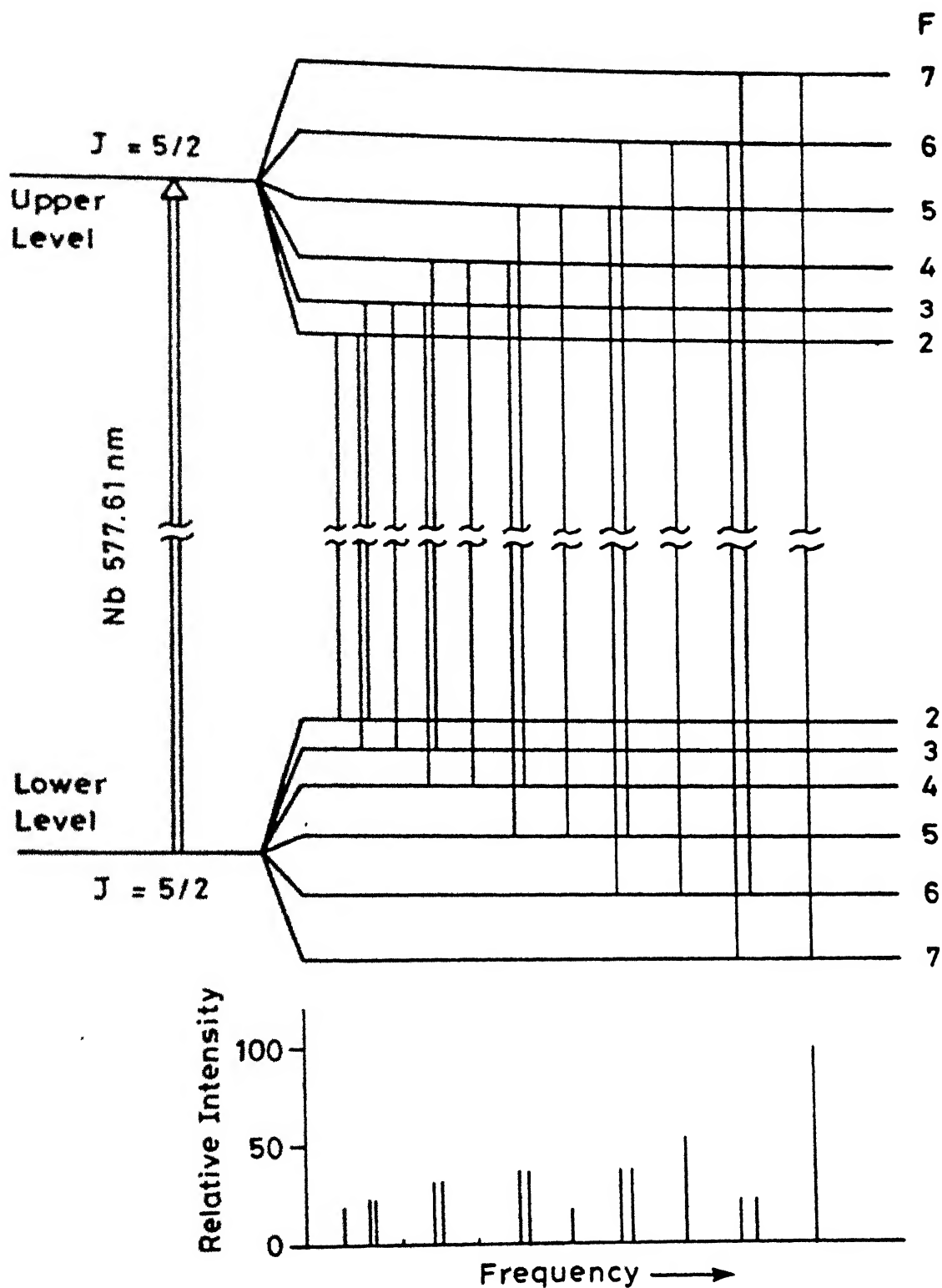


Fig. 24(c) Hfs energy level scheme of the niobium transition at 576.03 nm. Lower part of the Figure shows all the hfs components along with their relative intensities.



**Fig. 25.** Hyperfine structure of niobium transition at 577.61 nm.  
(a) recorded spectrum (b) computer fitted spectrum.





**Fig. 23(c)** Hfs energy level scheme of the niobium transition at 577.61 nm. Lower part of the Figure shows all the hfs components along with their relative intensities.

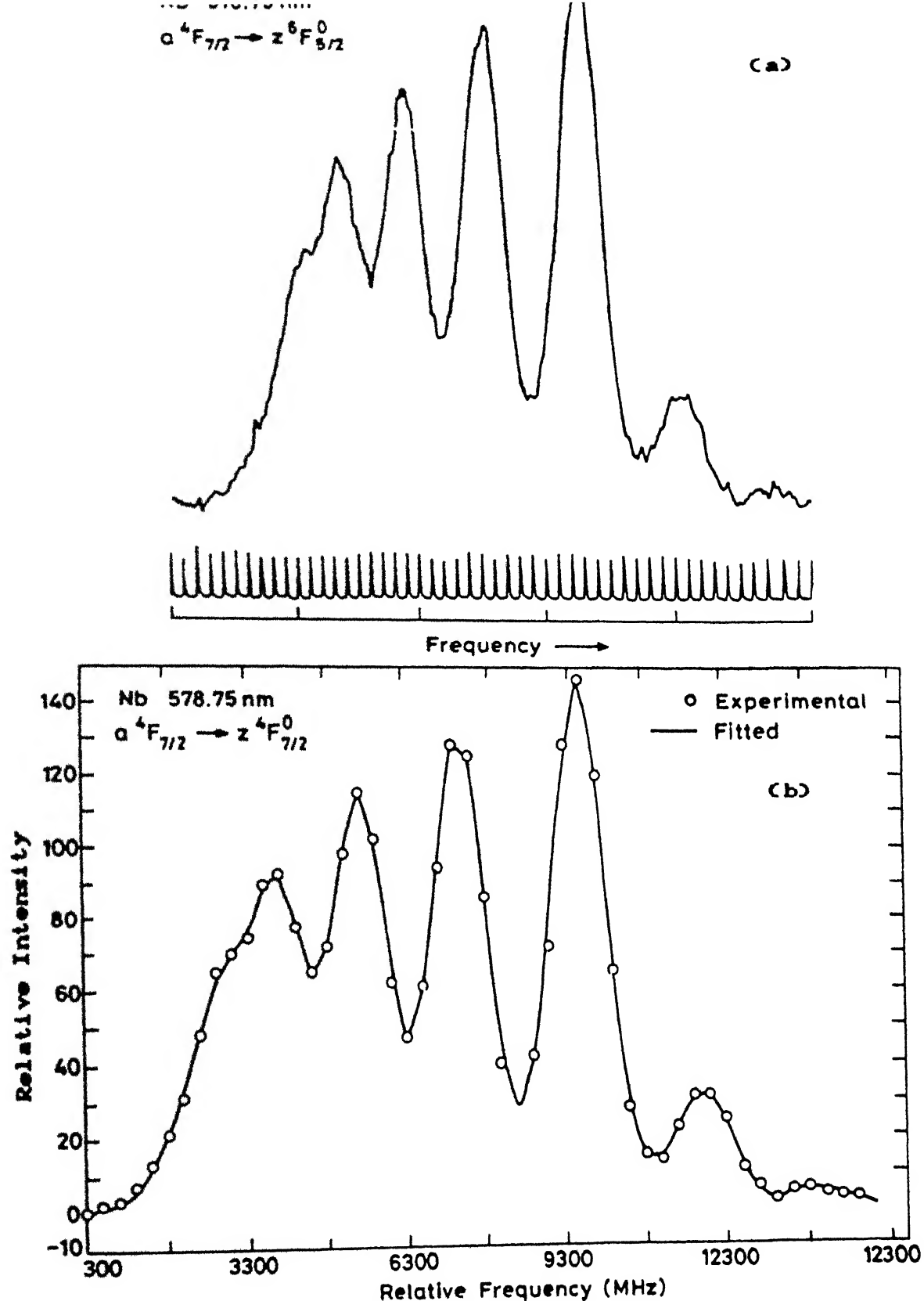


**Fig. 26.** Hyperfine structure of niobium transition at 578.75 nm.  
 (a) recorded spectrum (b) computer fitted spectrum.

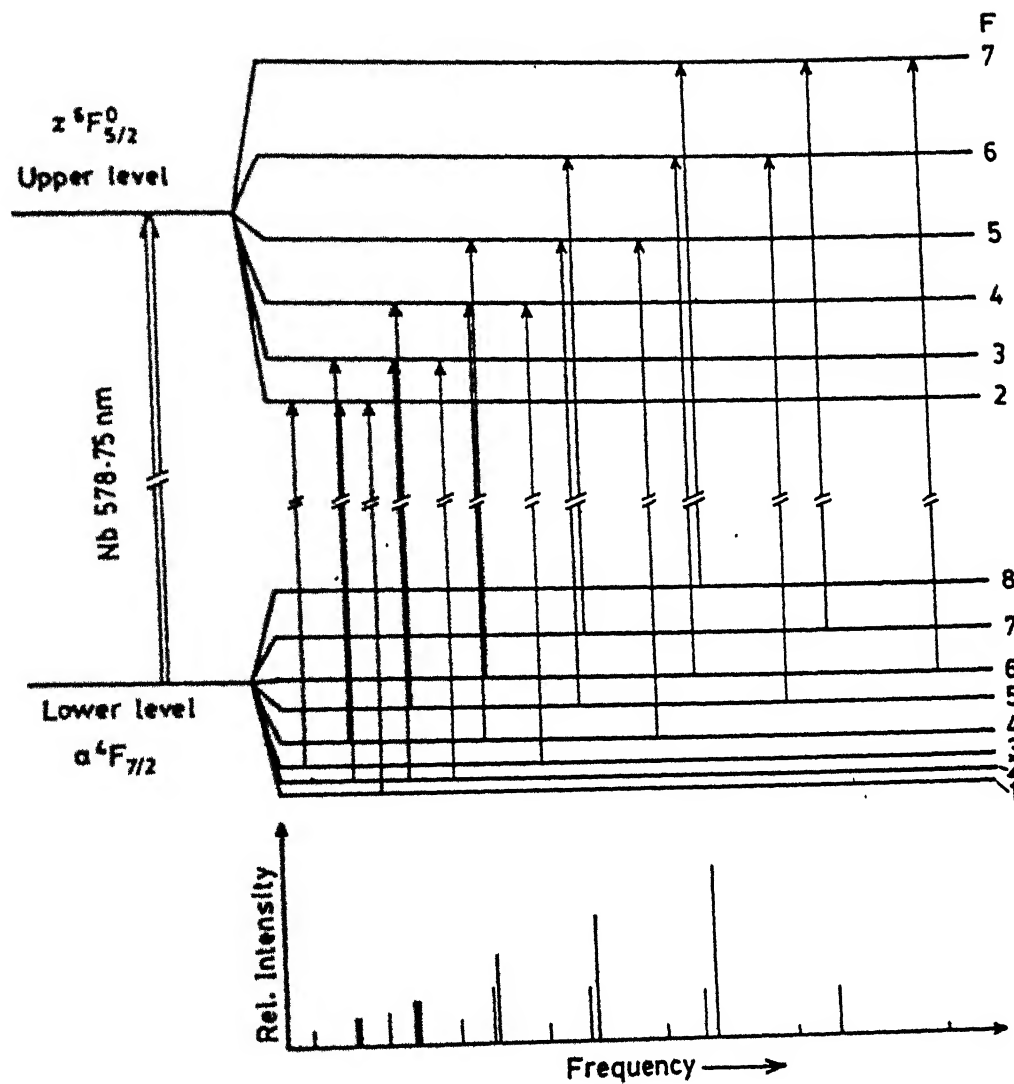
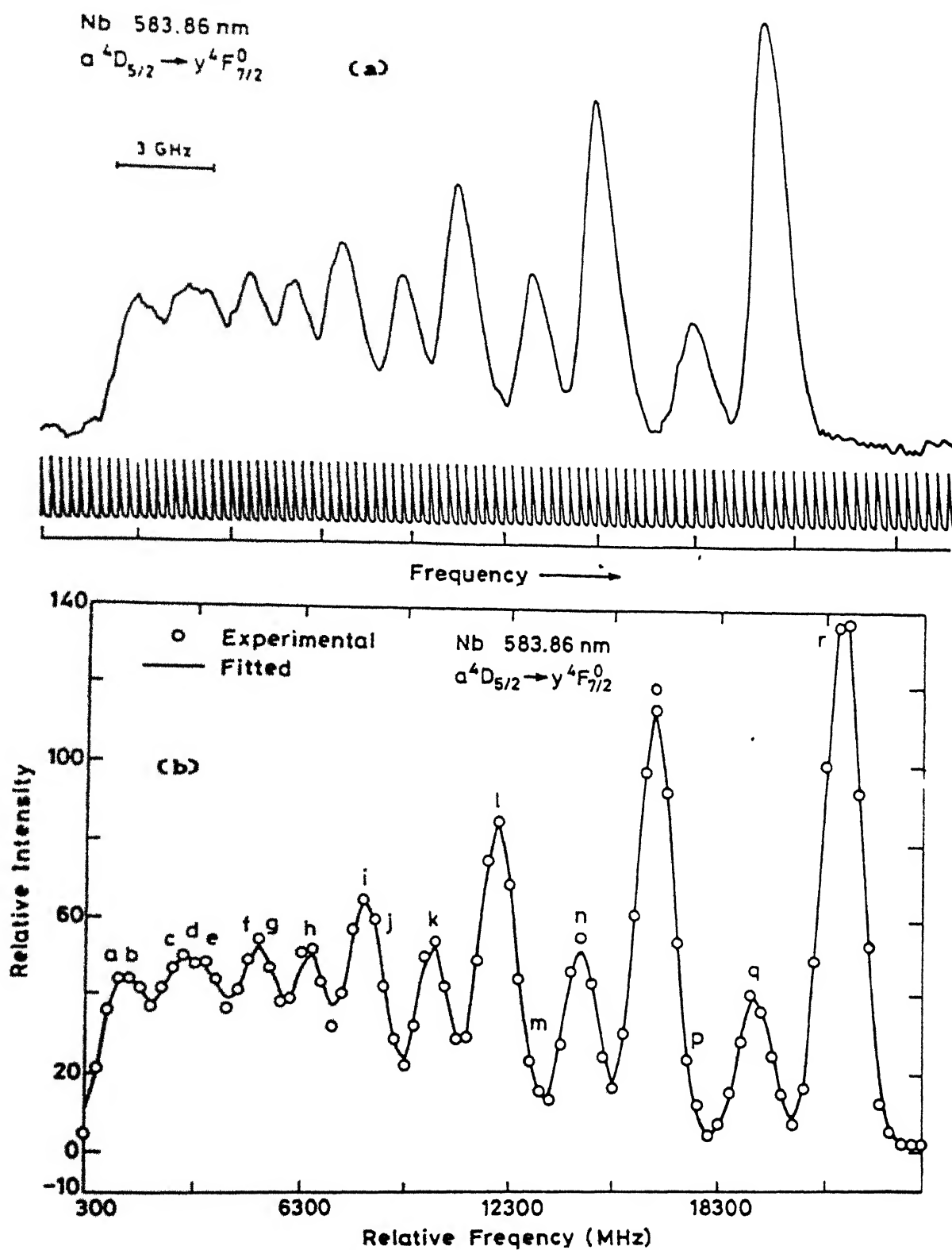


Fig. 28(c) Hfs energy level scheme of the niobium transition at 578.75 nm. Lower part of the Figure shows all the hfs components along with their relative intensities.



**Fig. 27.** Hyperfine structure of niobium transition at 583.86 nm.  
 (a) recorded spectrum (b) computer fitted spectrum.

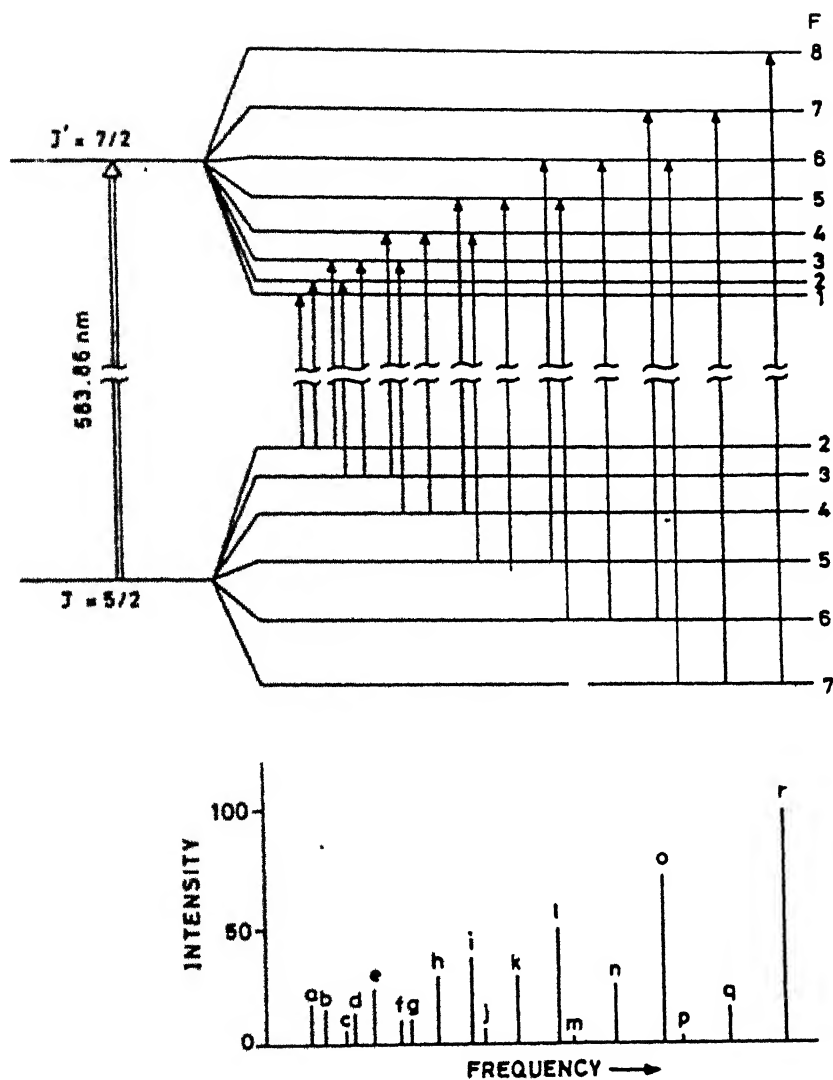
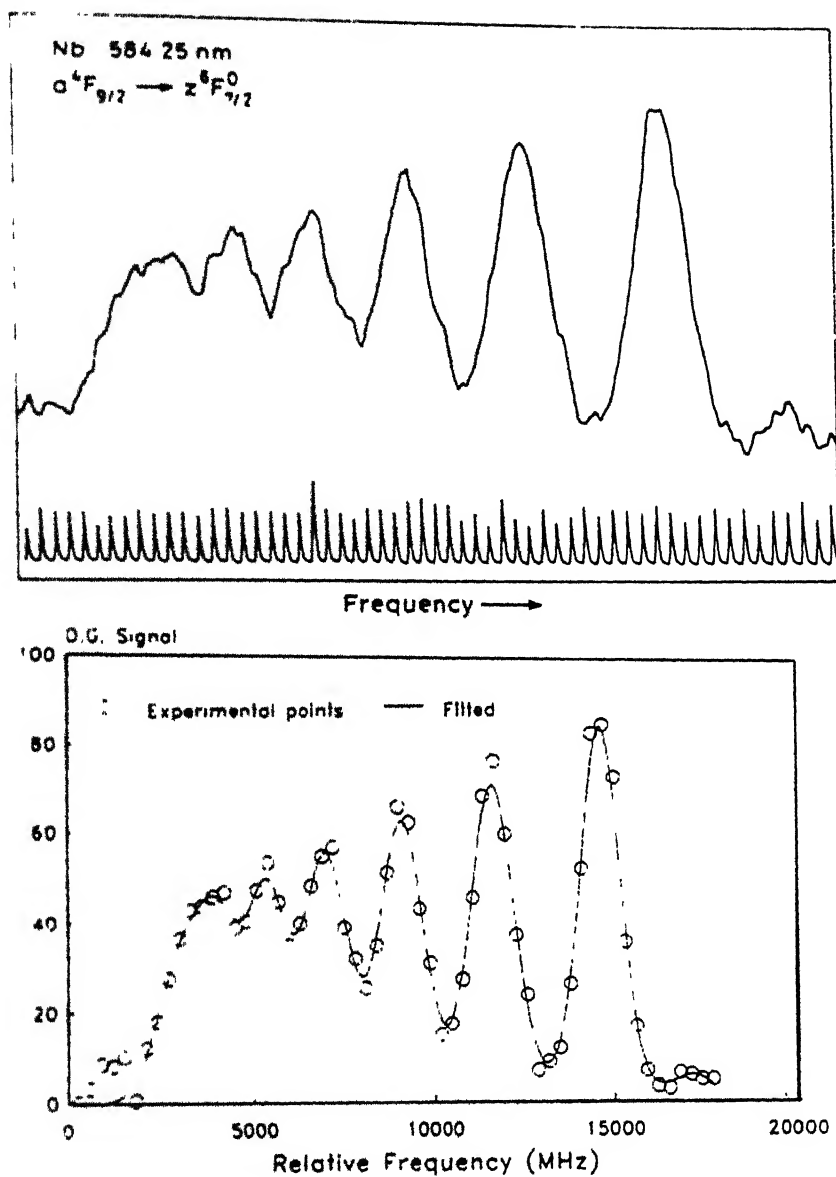
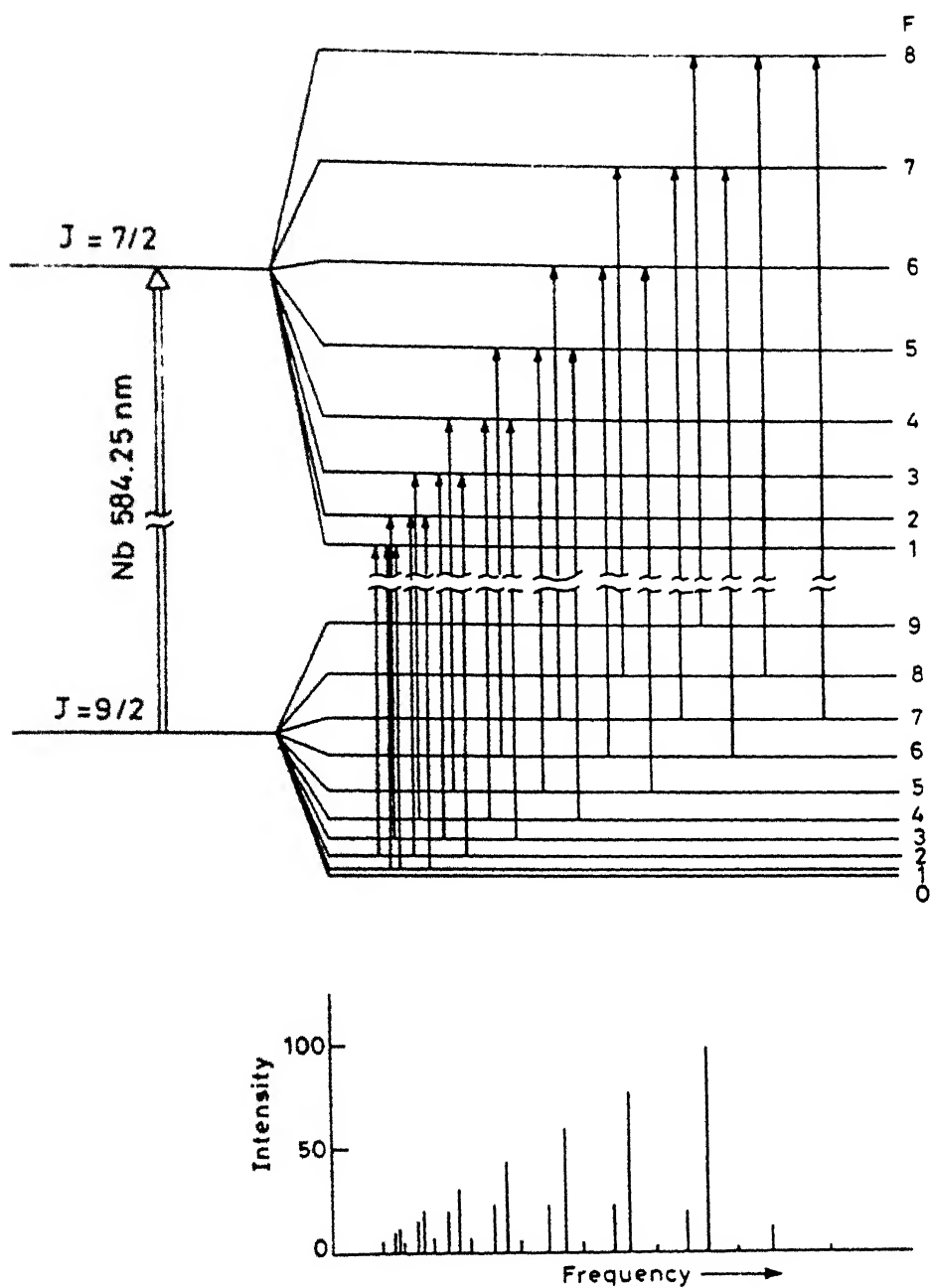


Fig. 27(c) Hfs energy level scheme of the niobium transition at 583.86 nm. Lower part of the Figure shows all the hfs components along with their relative intensities.



**Fig. 28.** Hyperfine structure of niobium transition at 584.25 nm. (a) recorded spectrum (b) computer fitted spectrum.



**Fig. 28(c)** Hfs energy level scheme of the niobium transition at 584.25 nm. Lower part of the Figure shows all the hfs components along with their relative intensities.

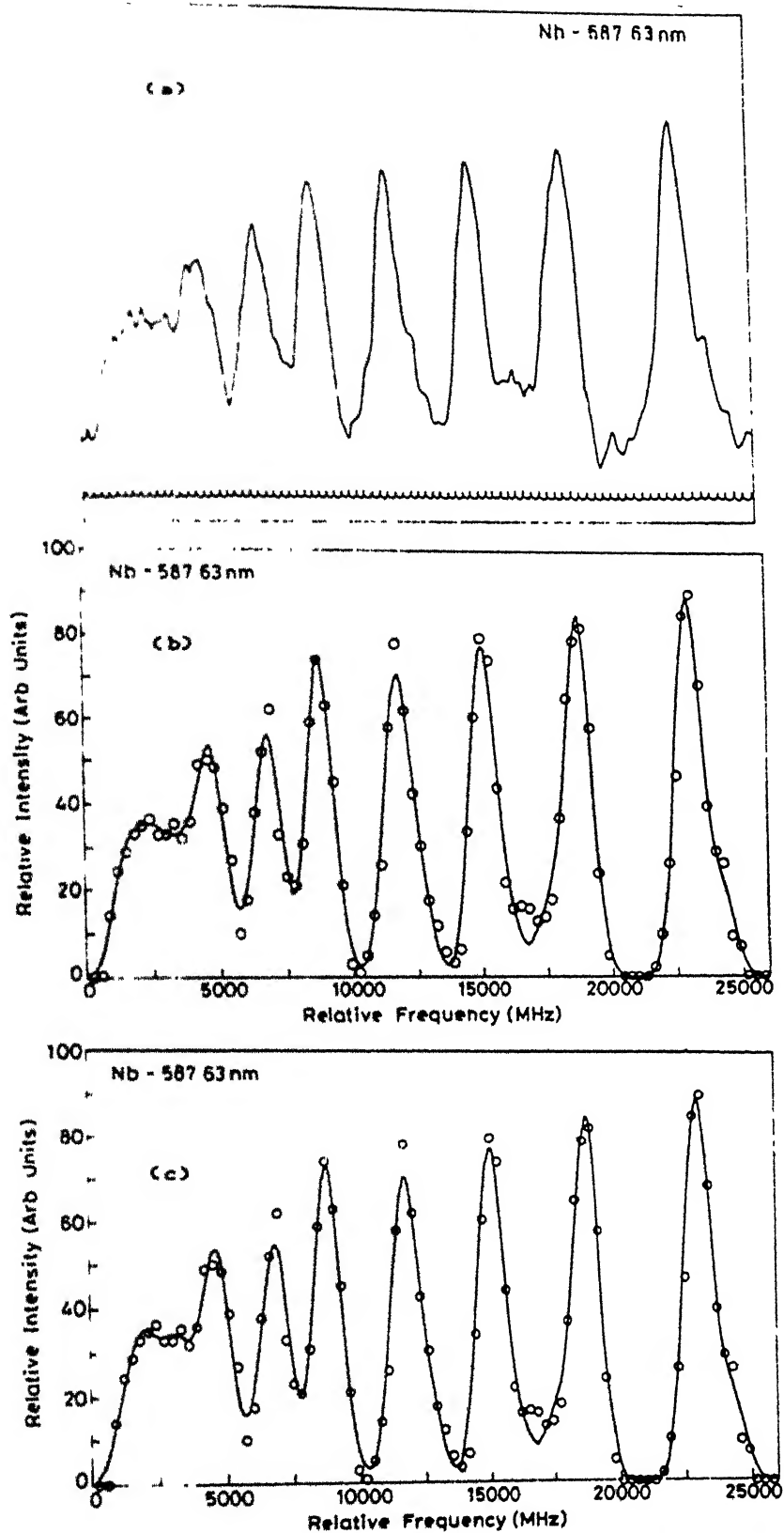


Fig. 20. Hyperfine structure of niobium transition at 587.60 nm.  
 (a) recorded spectrum (b) & (c) computer fitted spectra.



The recorded spectra are analyzed in a manner similar to that of scandium. The constants obtained from this analysis are presented in Table VI. The known constants, wherever available, are also included in the Table VI for comparison. The constants marked with \* are reported for the first time, to the best of our knowledge.

In conclusion, we demonstrated that hyperfine structure of niobium can easily be studied using laser optogalvanic spectroscopy. Large nuclear magnetic dipole moment of this transition element gives rise to large hfs separations which can be resolved even when the resolution is limited by the Doppler broadening of the transitions. Hyperfine coupling constants,  $A$  and  $B$ , for a large number of states of niobium in the configuration  $4d^3 5s^2$ ,  $3d^4 5s$ ,  $4d^5$ ,  $4d^3 4s 4p$  and  $4d^4 4d 5p$  are reported. Most of these levels are high lying metastable states and higher odd parity states where very little information is available at present.

TABLE V

Observed fine structure transitions of niobium along with their wavelengths in air and relative O.G. intensities.

Sr No.	Wavelength (nm)	Lower Level Energy (cm <sup>-1</sup> )	Lower Level State	Upper Level Energy (cm <sup>-1</sup> )	Upper Level State	Relative Intensity
1	566.47*	1142.79	a <sup>4</sup> F <sub>3/2</sub>	18791.09	z <sup>6</sup> F <sub>1/2</sub> <sup>o</sup>	-
2	569.79*	13629.15	b <sup>4</sup> P <sub>1/2</sub>	31174.68	y <sup>4</sup> S <sub>3/2</sub> <sup>o</sup>	-
3	570.62*	15282.35	b <sup>4</sup> D <sub>7/2</sub>	32802.44	w <sup>4</sup> G <sub>9/2</sub> <sup>o</sup>	-
4	570.65*	8410.90	a <sup>4</sup> D <sub>1/2</sub>	25930.03	y <sup>4</sup> F <sub>3/2</sub> <sup>o</sup>	-
5	572.57*	18035.97	b <sup>2</sup> G <sub>9/2</sub>	35496.39	y <sup>2</sup> H <sub>9/2</sub> <sup>o</sup>	-
6	576.03*	8705.32	a <sup>4</sup> D <sub>3/2</sub>	26060.65	y <sup>4</sup> F <sub>5/2</sub> <sup>o</sup>	-
7	577.11*	15282.35	b <sup>4</sup> D <sub>7/2</sub>	32605.32	v <sup>4</sup> F <sub>9/2</sub> <sup>o</sup>	-2.5
8	577.61*	11344.70	a <sup>6</sup> S <sub>5/2</sub>	28652.66	y <sup>6</sup> P <sub>5/2</sub> <sup>o</sup>	-2.0
9	577.98	12982.38	b <sup>4</sup> F <sub>7/2</sub>	30297.23	x <sup>4</sup> F <sub>9/2</sub> <sup>o</sup>	2.0
10	578.75*	2154.11	a <sup>4</sup> F <sub>7/2</sub>	19427.90	z <sup>6</sup> F <sub>5/2</sub> <sup>o</sup>	7.0
11	579.42	12018.25	a <sup>4</sup> G <sub>5/2</sub>	29271.99	z <sup>4</sup> H <sub>7/2</sub> <sup>o</sup>	2.5
12	580.10	12136.86	a <sup>2</sup> G <sub>7/2</sub>		y <sup>4</sup> F <sub>7/2</sub> <sup>o</sup>	3.0

.....contd.

13	581.53*	12018.25	$a^4G_{5/2}$	29209.42	$x^4D_{7/2}^o$	-
14	583.49	13145.71	$b^4F_{9/2}$	30297.23	$x^4F_{9/2}^o$	-3.5
15	583.86	9043.14	$a^4D_{5/2}$	26165.79	$y^4F_{7/2}^o$	-6.5
16	583.92*	18035.92	$b^2G_{9/2}$	35156.94	$v^4G_{9/2}^o$	-6.5
17	584.25*	2805.36	$a^4F_{9/2}$	19916.69	$z^6F_{7/2}^o$	5.5
18	584.61*	11344.70	$a^6S_{5/2}$	28445.33	$y^4P_{5/2}^o$	-4.0
19	586.49	-	-	-	-	4.0
20	586.65*	5965.45	$a^4P_{5/2}$	23006.86	$z^4P_{3/2}^o$	19.0
21	587.47*	9043.14	$a^4D_{5/2}$	26060.65	$y^4F_{5/2}^o$	-
22	587.63	18332.04	$—_{11/2}$	35344.86	$y^2H_{11/2}^o$	-5.0
23	587.78*	4998.17	$a^4P_{1/2}$	22006.74	$z^4P_{1/2}^o$	5.0
24	589.34*	14211.30	$b^4P_{3/2}$	31174.65	$y^4S_{3/2}^o$	-4.5
25	590.06*	9497.52	$a^4D_{7/2}$	26440.33	$y^4F_{9/2}^o$	-10.0
26	590.38*	11344.70	$a^6S_{5/2}$	28278.25	$y^6P_{3/2}^o$	-5.0
27	591.05	12357.70	$a^4G_{9/2}$	29271.99	$z^4H_{7/2}^o$	-1.5
28	592.43	10922.74	$a^4H_{7/2}$	27797.44	$z^2F_{5/2}^o$	3.0

.....contd.

29	592.74	15467.08	$b^4D_{5/2}$	32333.18	$w^4F^o_{7/2}$	-6.5
30	592.82	11344.70	$a^6S_{5/2}$	28208.48	$z^4S^o_{3/2}$	-5.0
31	597.12	-	-	-	-	2.0
32	598.32*	5297.92	$a^4P_{3/2}$	22006.74	$z^4P^o_{1/2}$	11.0
33	598.61	13145.71	$b^4F_{9/2}$	29846.50	$z^4H^o_{11/2}$	1.5
34	599.79	9497.52	$a^4D_{7/2}$	26165.79	$y^4F^o_{7/2}$	-3.5
35	602.97	12692.12	$b^4F_{5/2}$	29271.99	$z^4H^o_{7/2}$	-4.5
36	604.87	17476.22	$b^2H_{11/2}$	34004.08	$z^2I^o_{11/2}$	3.0
37	605.26	12692.12	$b^4F_{5/2}$	29209.42	$x^4D^o_{7/2}$	31.0
38	605.66	15282.35	$b^4D_{7/2}$	31973.24	$v^4F^o_{7/2}$	-3.0
		18332.04	$—_{11/2}$	34838.33	$z^2H^o_{11/2}$	
39	606.78	10237.51	$a^2D_{5/2}$	26713.32	$x^6D^o_{3/2}$	2.0
40	622.19	8705.32	$a^4D_{3/2}$	24773.03	$z^2D^o_{5/2}$	-2.5
41	622.82	-	-	-	-	-1.5
42	625.18	18332.04	$—_{11/2}$	34323.20	$z^2I^o_{13/2}$	-4.0

TABLE - VI

Hyperfine structure constants as compared with the previous values wherever possible. Uncertainties in A's are given in the brackets in MHz and that in B's are  $\approx 35$  MHz.

Level	This work		Others	
	A(MHz)	B(MHz)	A(MHz)	B(MHz)
$4d^3 5s^2 \ a^4P_{3/2}$	495.5(6)	30	497.7569(16)	59.902(1.4)
$4d^4 5s \ a^4D_{3/2}$	-136.9(6)	-69	-143.3225(217)	-10.761(178)
$4d^4 5s \ a^4D_{7/2}$	-474.4(2)	90	-477.0373(35)	126.899(81)
$4d^5 \ a^6S_{5/2}$	-645.0(7)	-	-639.3786(79)	-0.061(92)
$*4d^4 5s \ b^4D_{7/2}$	957.3(5)	-	-	-
$4d^4 5p \ z^4P^o_{1/2}$	-273.7(13)	-	-267.3(.3)	-
$4d^4 5p \ y^4F^o_{5/2}$	261.1(3)	-	266.7(.3)	46.1(4.8)
$4d^4 5p \ y^4F^o_{9/2}$	325(2)	120	337.61(.2)	88.6(8.1)
$4d^3 5s 5p \ y^6P^o_{3/2}$	743.2(6)	19	747.1(0.8)	14.7(7.6)
$*4d^3 5s 5p \ y^6P^o_{5/2}$	746.2(6)	-154	-	-
$*4d^4 5p \ v^4F^o_{9/2}$	264.7(4)	-	-	-
$*4d^4 5p \ w^4G^o_{9/2}$	632.5(3)	16.5	-	-
$4d^3 5s^2 \ a^4F_{3/2}$	634.7(10)	30.8	644.16(54)	32.8(128)
$4d^4 5s \ a^4D_{1/2}$	2001.7(10)	-	1997.0(1)	-

.....contd.

$4d^3 5s^2 a^4 F_{7/2}$	289.5(10)	65.3	292.1939(16)	44.320(47)
$4d^4 5s a^4 D_{5/2}$	-408.6(10)	38.9	-407.8606(43)	35.060(75)
$4d^3 5s^2 a^4 F_{9/2}$	279.4(10)	64.7	269.6299(76)	64.805(130)
$3d^3 5s^2 a^4 P_{5/2}$	341.3(10)	-122.2	343.1670(5)	-80.454(9)
$*4d^3 5s 5p z^6 F_{1/2}^O$	-779.6(10)	-	-	-
$*4d^4 5p y^4 F_{3/2}^O$	559.6(10)	100.5	557.4(.5)	57.5(4.0)
$*4d^3 5s 5p z^6 F_{5/2}^O$	654.7(10)	7.0	-	-
$*4d^4 5p y^4 F_{7/2}^O$	299.6(10)	96.4	-	-
$*4d^3 5s 5p z^6 F_{7/2}^O$	680.6(10)	-277.7	-	-
$4d^4 5p z^4 P_{3/2}^O$	-145.1(10)	-17.3	-137.9(.4)	-30.9(3.7)
$*4d^4 5s b^2 G_{9/2}$	707.8	18	-	-
$*4d^4 5s b^4 P_{1/2}$	2906.3	8.8	-	-
$4d^3 5s^2 a^4 P_{1/2}$	537.4(8)	-	540.1	-
$*4d^4 5s a^4 G_{5/2}$	-161.2	-	-	-
$*4d^4 5s b^4 P_{3/2}$	-786.97	-100	-	-

.....contd.

---

$*4d^4 5s \ x^4D_{5/2}$	-350.0	36.5	-
$*4d^4 4p \ v^4G^O_{9/2}$	522.7	-58	-
$*4d^3 5s 5p \ y^4P^O_{5/2}$	607.8	150	-
$*4d^3 5s 5p \ y^4S^O_{3/2}$	1047.0	8.8	-
$*4d^4 5p \ z^4P^O_{1/2}$	-270.8(6)	-	-
$*4d^3 5s 5p \ x^4D_{7/2}$	505.4	-	-
$*4d^4 5p \ y^4F^O_{5/2}$	300.0	46.1	-

---

## CHAPTER VI

### HYPERFINE STRUCTURE AND ISOTOPE SHIFT OF RHENIUM

#### 6.1 INTRODUCTION

Hyperfine structure of the ground state,  $a^6S_{5/2}$ , of rhenium was studied by Schlecht et al. [93] and Armstrong and Marrus [94] by atomic beam magnetic resonance (ABMR) technique in 1965. In the same year Hohberg et al. [95] reported hyperfine structure measurements of fifteen levels belonging to the configurations  $5d^56s^2$ ,  $5d^56s6p$ ,  $5d^56s7s$ ,  $5d^66s$ ,  $5d^66p$ , and  $5d^46s^26p$ , using Fabry-Perot interferometer and a spectrograph. In 1979, Bucholz et al. [96] presented some studies on isotope shift between the two natural isotopes, 185 and 187, of rhenium and used this data for the configuration identification. Buttgenbach et al. [97] studied hyperfine structure of  $^{185}\text{Re}$  and  $^{187}\text{Re}$  in the states  $5d^56s^2 \ ^6S_{5/2}$  and  $^4P_{5/2}$  using ABMR method. They also reported hyperfine structure measurements in the states  $5d^56s^2 \ ^4G_{5/2}$  and  $5d^66s \ ^6D_{9/2}$  of  $^{187}\text{Re}$ . In 1982, Bürger et al. [98] reported results of extensive studies performed on rhenium. They recorded high resolution spectra of fourteen transitions starting from the metastable states of rhenium belonging to the configurations  $(5d + 6s)^7$ , by laser induced fluorescence in an atomic beam. From this



spectra. they deduced isotope shifts for all the transitions and hyperfine coupling constants for thirteen metastable and nine excited states. In addition, they employed ABMR method coupled with the laser induced state selective detection of metastable states to study hyperfine structure of five metastable states.

In the present work high resolution optogalvanic spectra of six transitions of rhenium are reported. Isotope shift between  $^{185}\text{Re}$  and  $^{187}\text{Re}$  is reported for all the six transitions. Hyperfine coupling constants, A and B, for both the isotopes are reported for all the levels involved in the transitions [38].

## 6.2 EXPERIMENTAL

Experimental setup shown in Fig. 7 was used for the hyperfine structure and isotope shift studies. The ring dye laser which usually gave a line width of 1 MHz, and could be tuned electronically over a range of 30 GHz, was used for excitation of the rhenium atoms present in the discharge. A rhenium / neon hollow cathode discharge lamp (Instrumentation Laboratory Inc. USA) was used for the purpose. The lamp was usually operated at 15 mA of current. The frequency calibration was achieved by recording the transmission peaks of a 300 MHz FSR Fabry-Perot interferometer. The maximum output power of the dye laser was 150 mW. Chopping frequency was adjusted in the range 300 to 700 Hz, to get the minimum noise.

### 6.3 RESULTS AND DISCUSSION

High resolution optogalvanic spectra of six transitions of rhenium, lying in the range 560 - 620 nm, were recorded. All these transitions along with their level assignments are given in Table VII. The level assignments are taken from Klinkenberg et al. [97]. Figure 30 shows a part of the fine structure level diagram of rhenium and the transitions studied. Recorded spectra were analyzed following the procedure similar to the one described in section 3.6 chapter III. The only difference was that the computer programs were modified to include both the isotopes and hence number of parameters involved was doubled. Isotope shift between the two natural isotopes,  $^{185}\text{Re}$  and  $^{187}\text{Re}$ , of rhenium is given in column 5 of Table VII. In column 6 of Table VII isotope shifts reported by others are given for comparison.

Figures 31(a) to 35(a) show the recorded hyperfine structure spectra of some of the transitions. Figure 31(b) to 35(b) show the computer fitted spectra of the same transitions. Figs. 33(c) and 36(c) show the hfs energy level scheme of two transitions of  $^{185}\text{Re}$ . A similar level scheme can be drawn for  $^{187}\text{Re}$  also. Most of the recorded spectra lie within 30 GHz, the maximum scan range of the ring dye laser. However one of the transitions, at 577.62 nm, is spread over almost 50 GHz. For this transition three overlapping spectra were recorded and then joined together. The recorded spectrum of the transition at

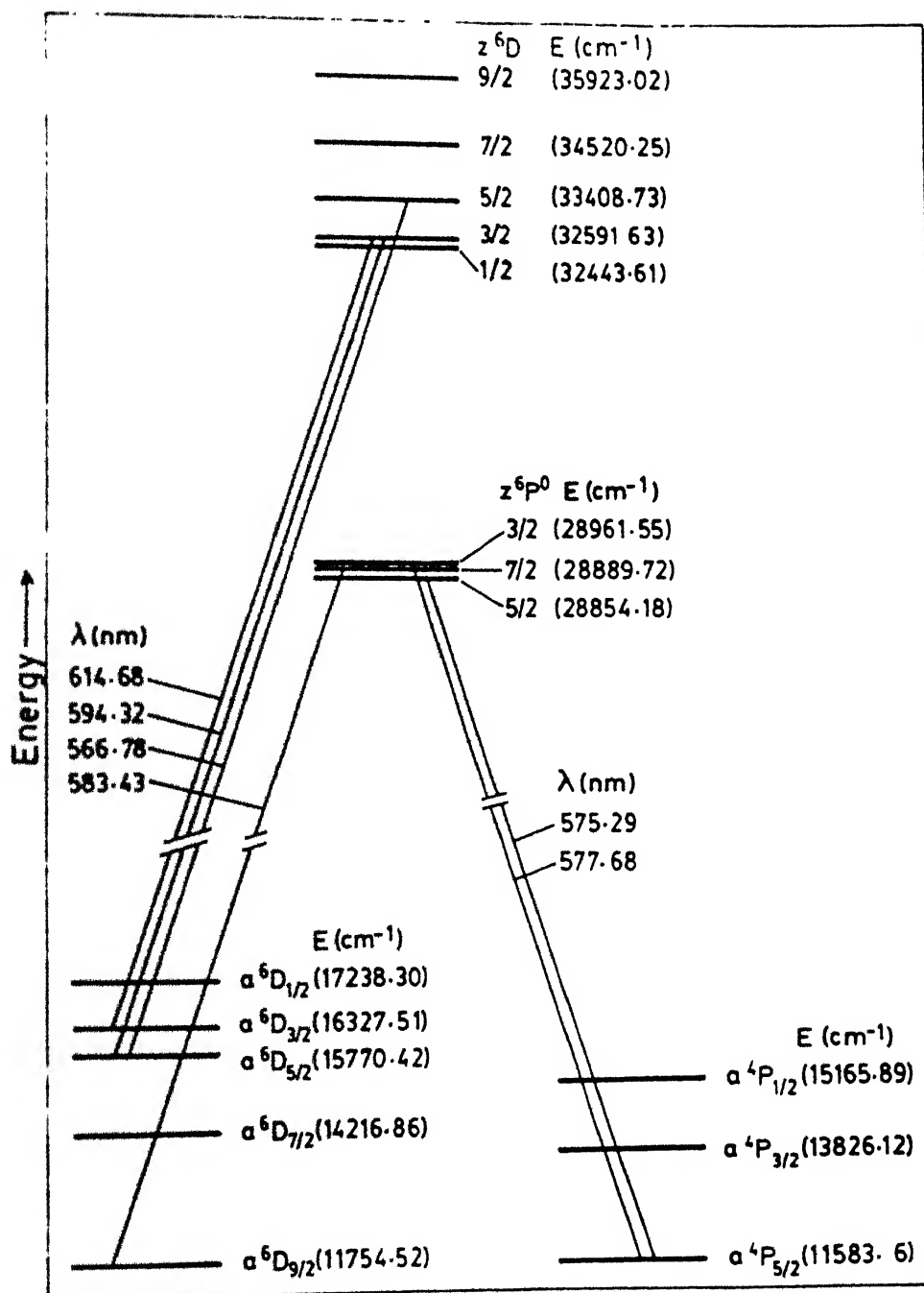
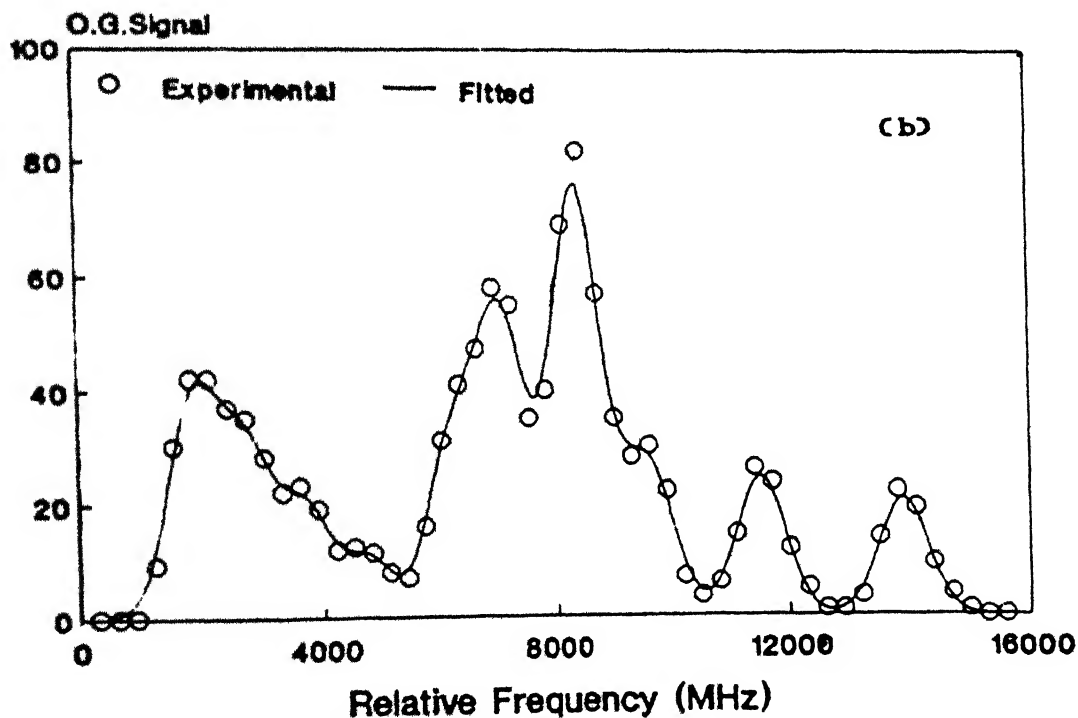
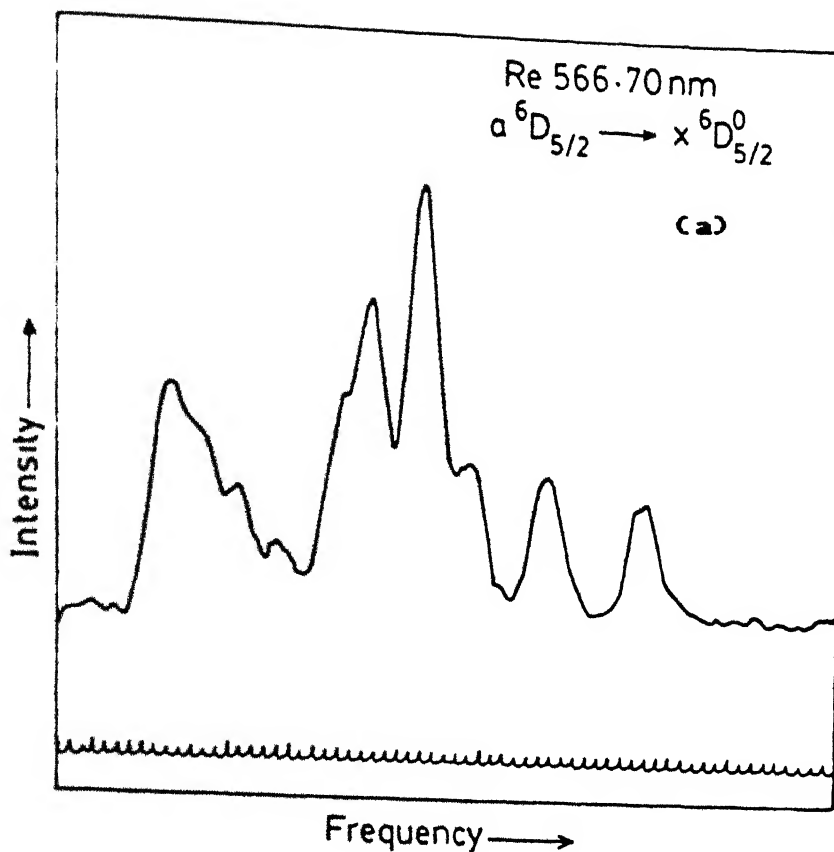
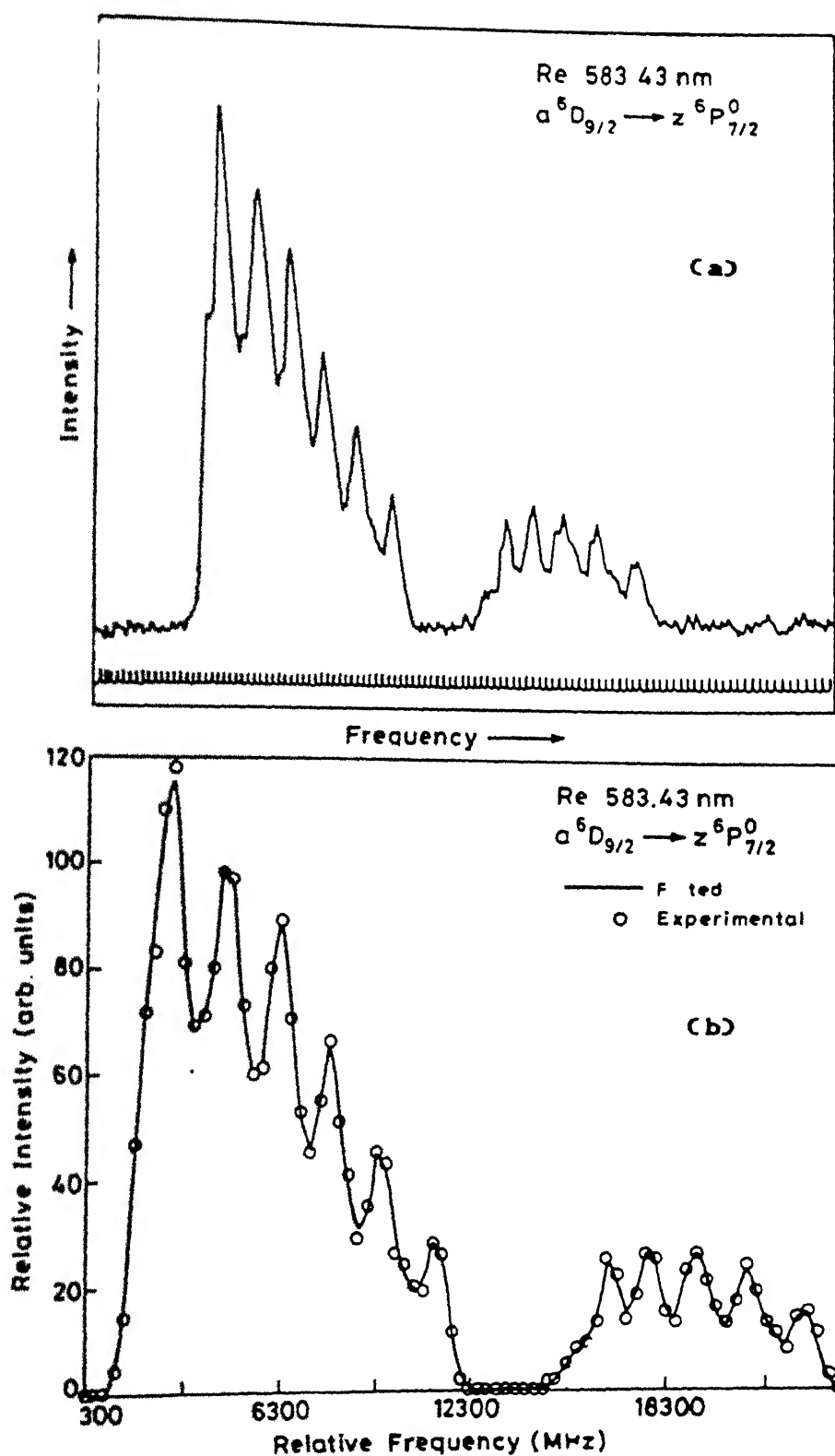


Fig. 30. A part of the energy level diagram of rhodium showing the transitions studied.



**Fig. 31.** Hyperfine structure of rhenium transition at 566.75 nm.  
 (a) recorded spectrum (b) computer fitted spectrum.



**Fig. 32.** Hyperfine structure of rhenium transition at 583.40 nm.  
(a) recorded spectrum (b) computer fitted spectrum.

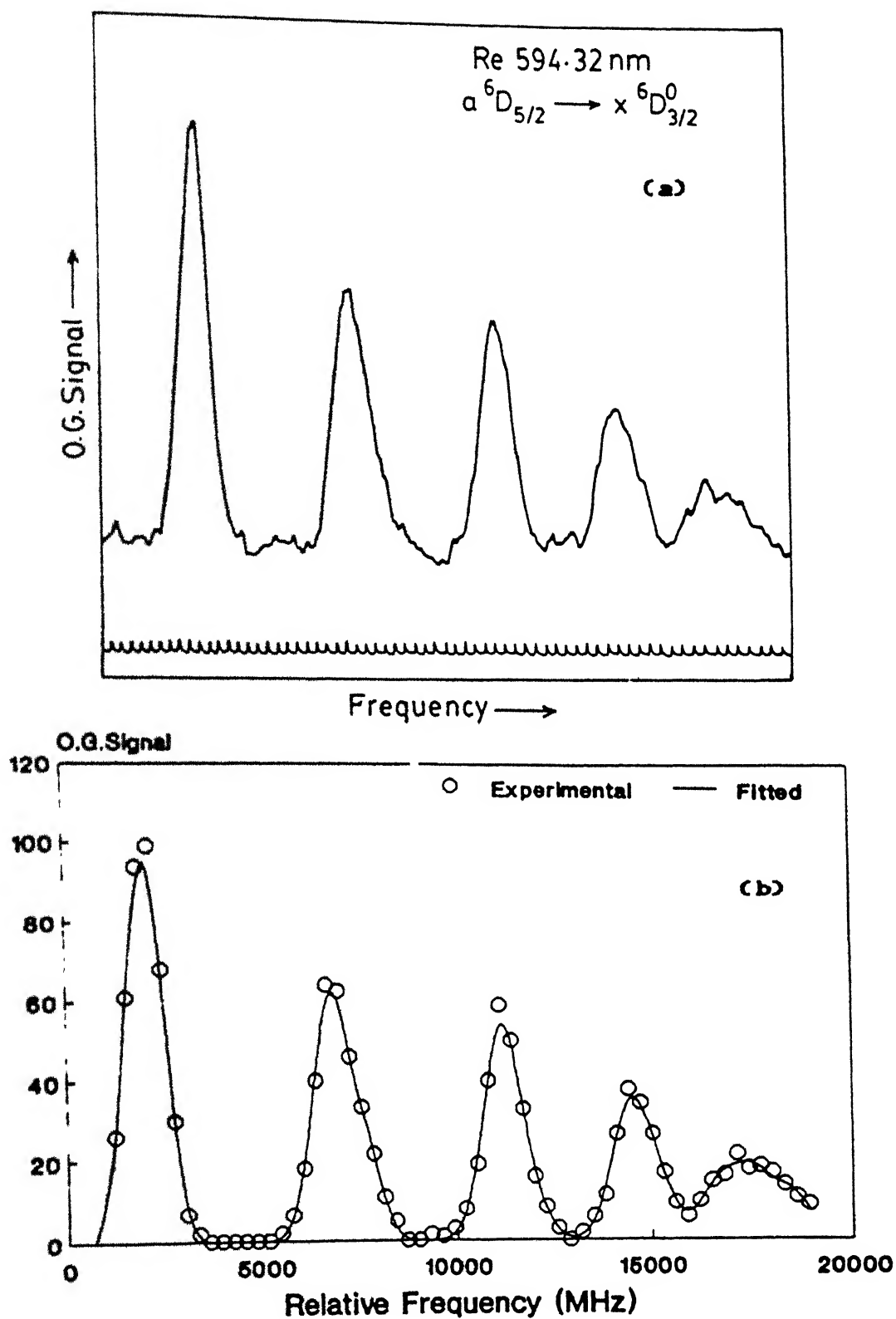


**Fig. 33.** Hyperfine structure of rhenium transition at 5943 nm.  
 (a) recorded spectrum (b) computer fitted spectrum.

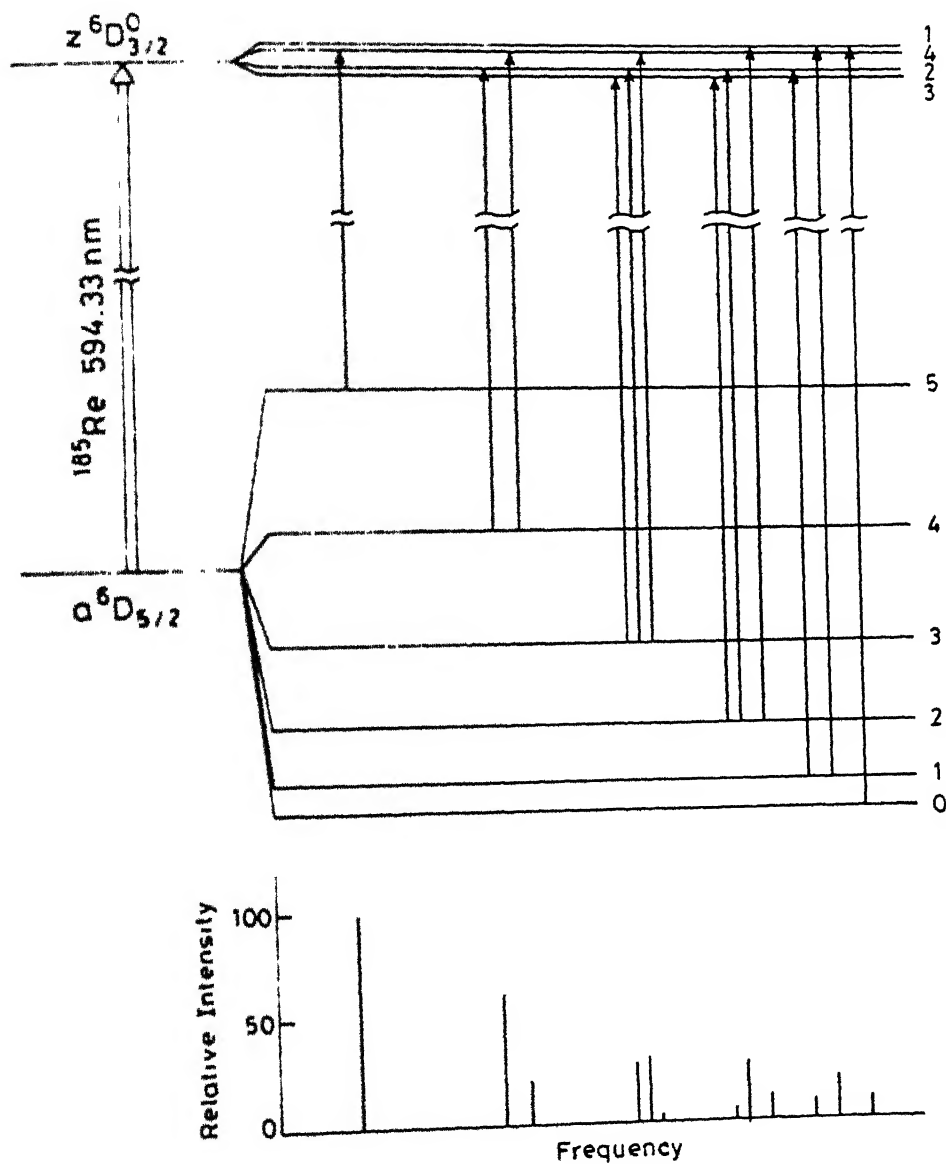


Fig. 33(c) Hfs energy level scheme of the  $^{185}\text{Re}$  transition at 594.33 nm. Lower part of the Figure shows all the hfs components along with their relative intensities.

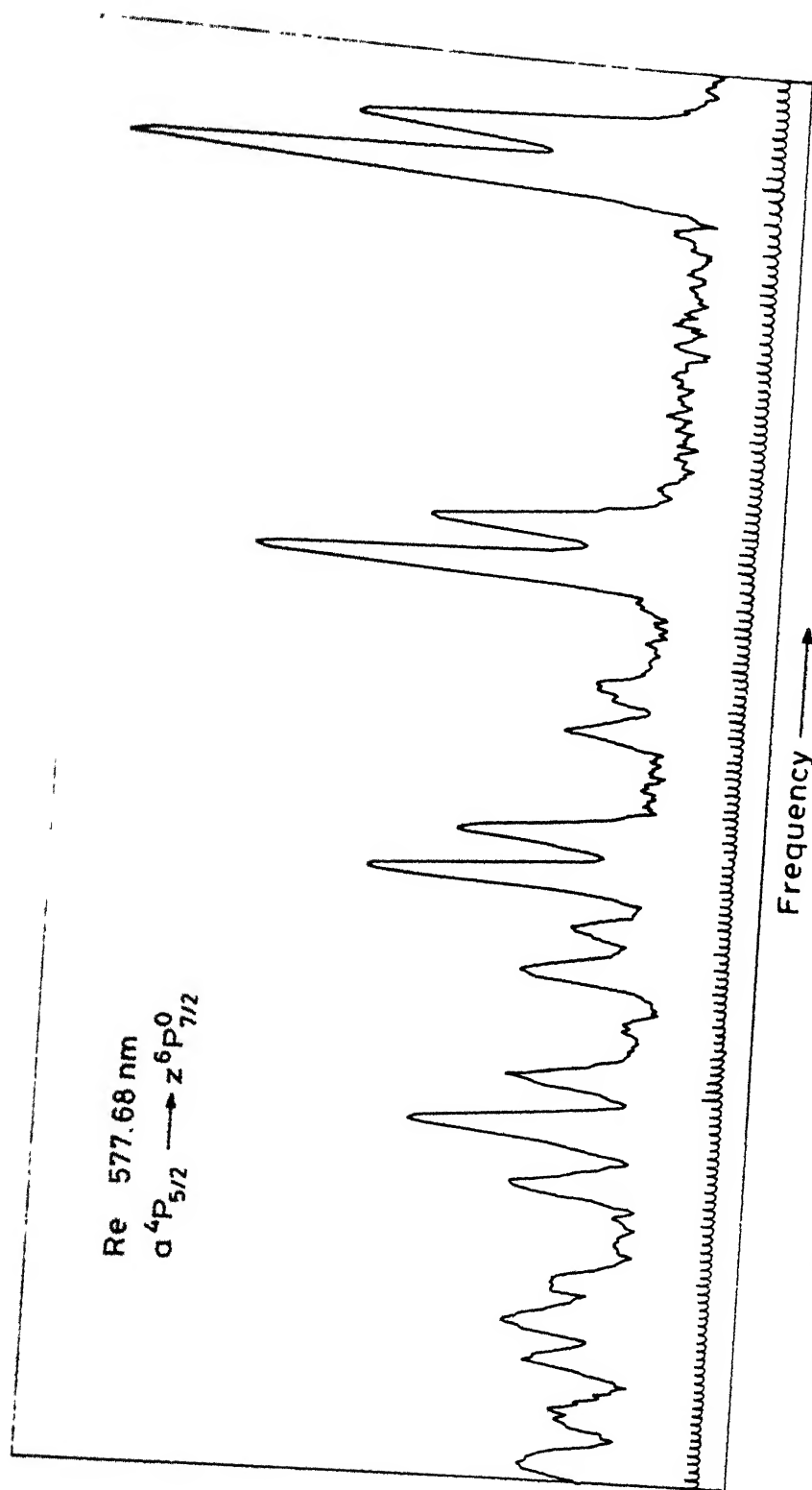
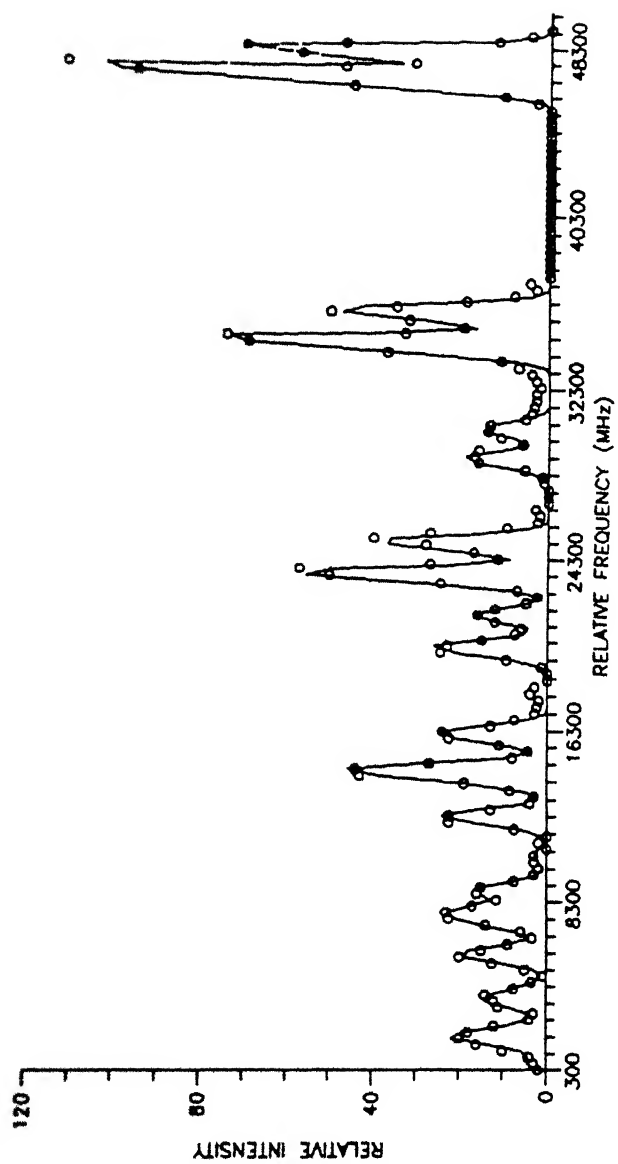


Fig. 34(a) Recorded hfs spectrum of rhenium transition at 577.60 nm.





**Fig. 34(b)** Computer fitted hfs spectrum of rhenium transition at 577.60 nm.

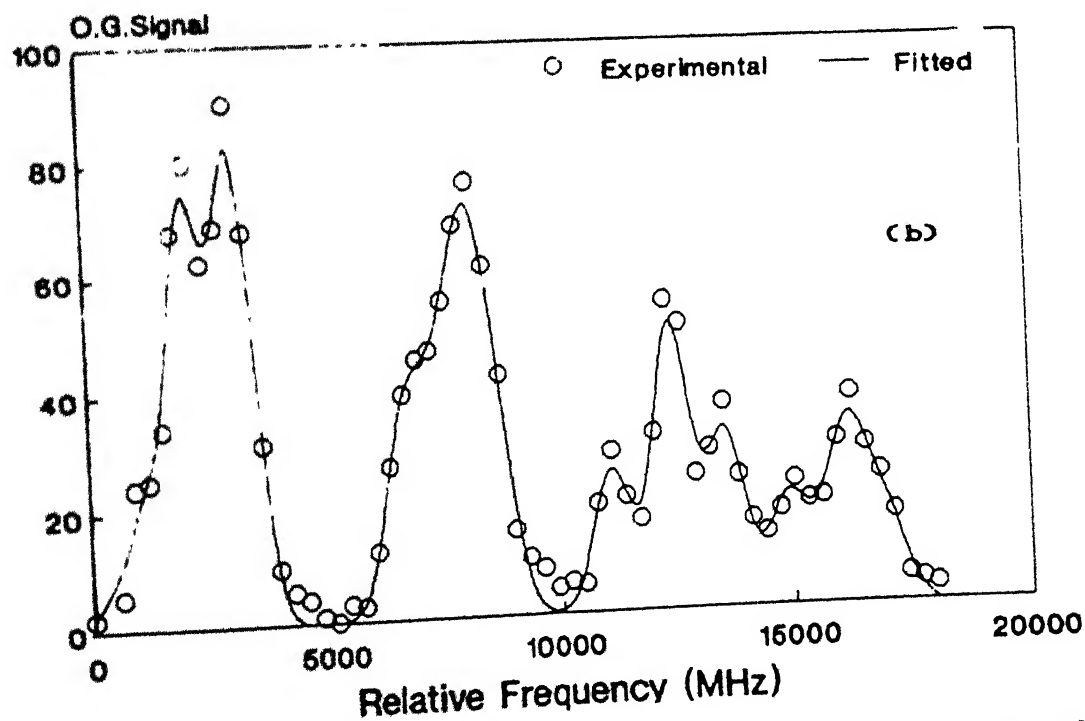
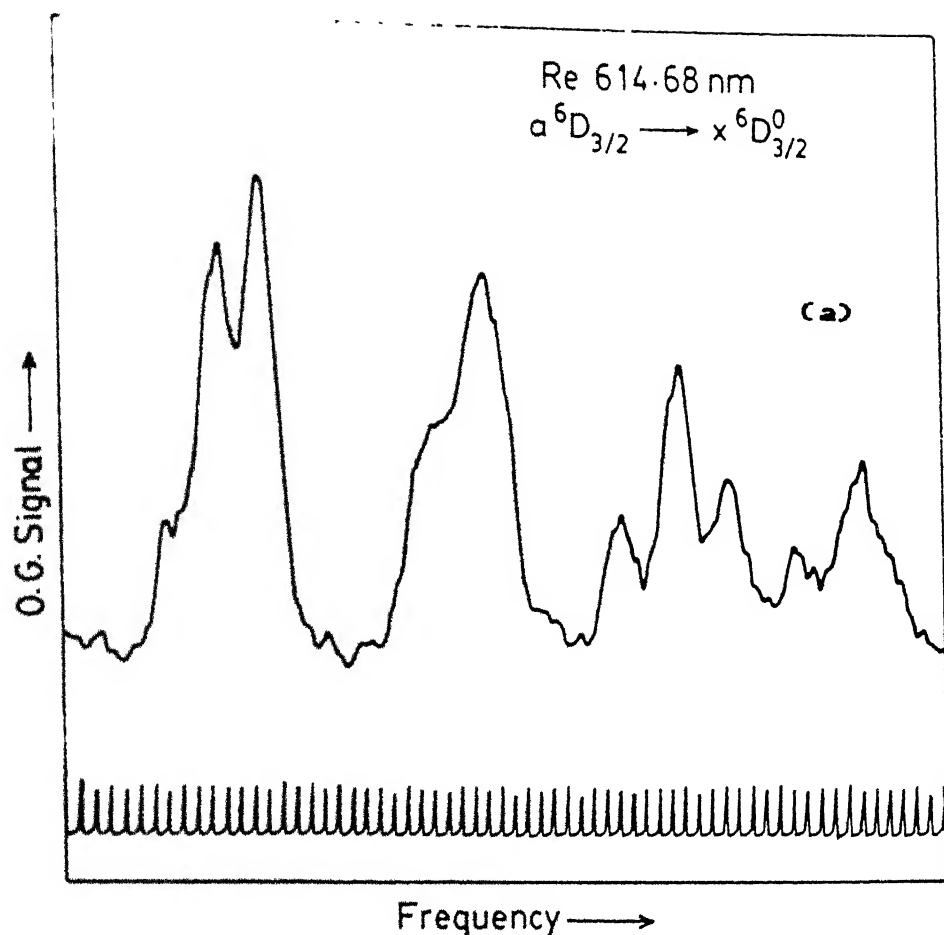


Fig. 35. Hyperfine structure of rhenium transition at 614.60 nm.  
 (a) recorded spectrum (b) computer fitted spectrum.

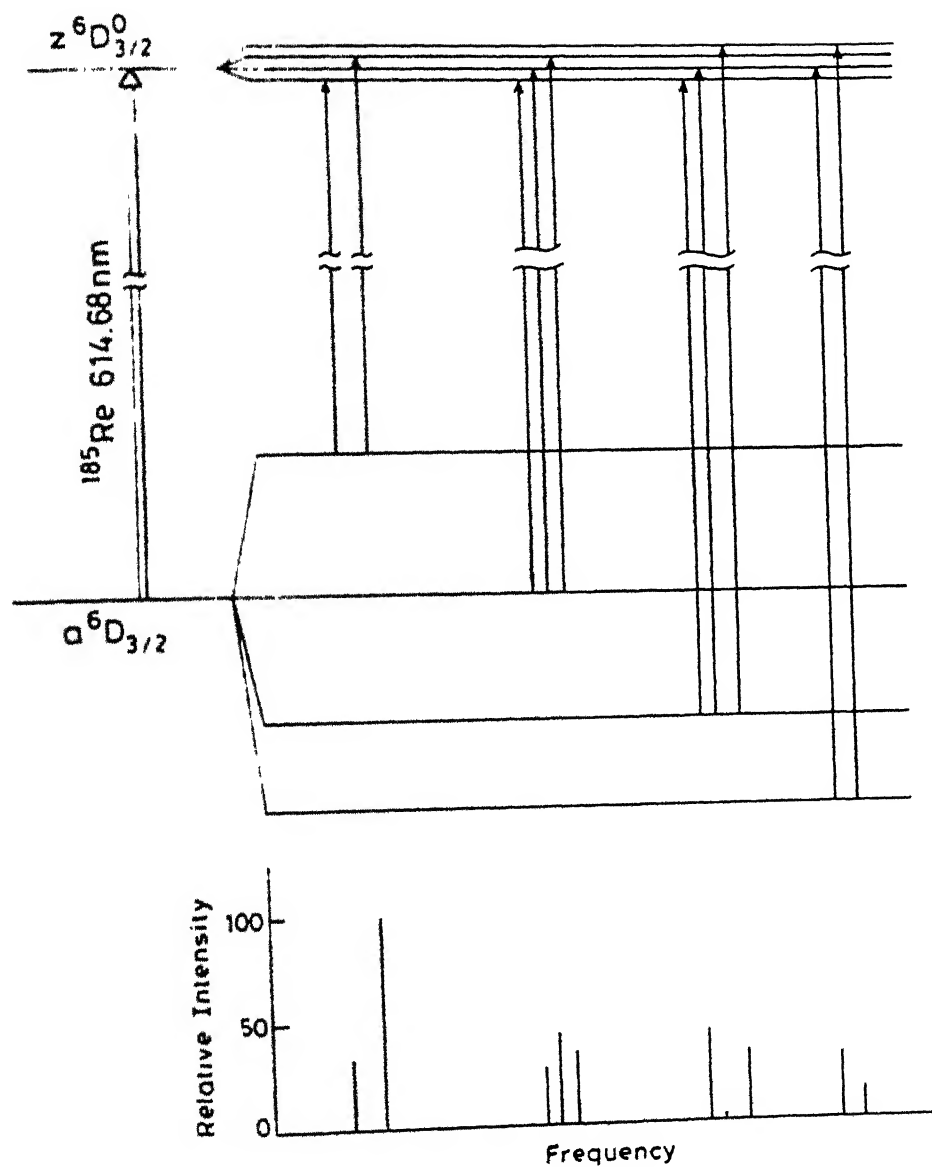


Fig. 35(c) Hfs energy level scheme of the  $^{185}\text{Re}$  transition at 614.68 nm. Lower part of the Figure shows all the hfs components along with their relative intensities.

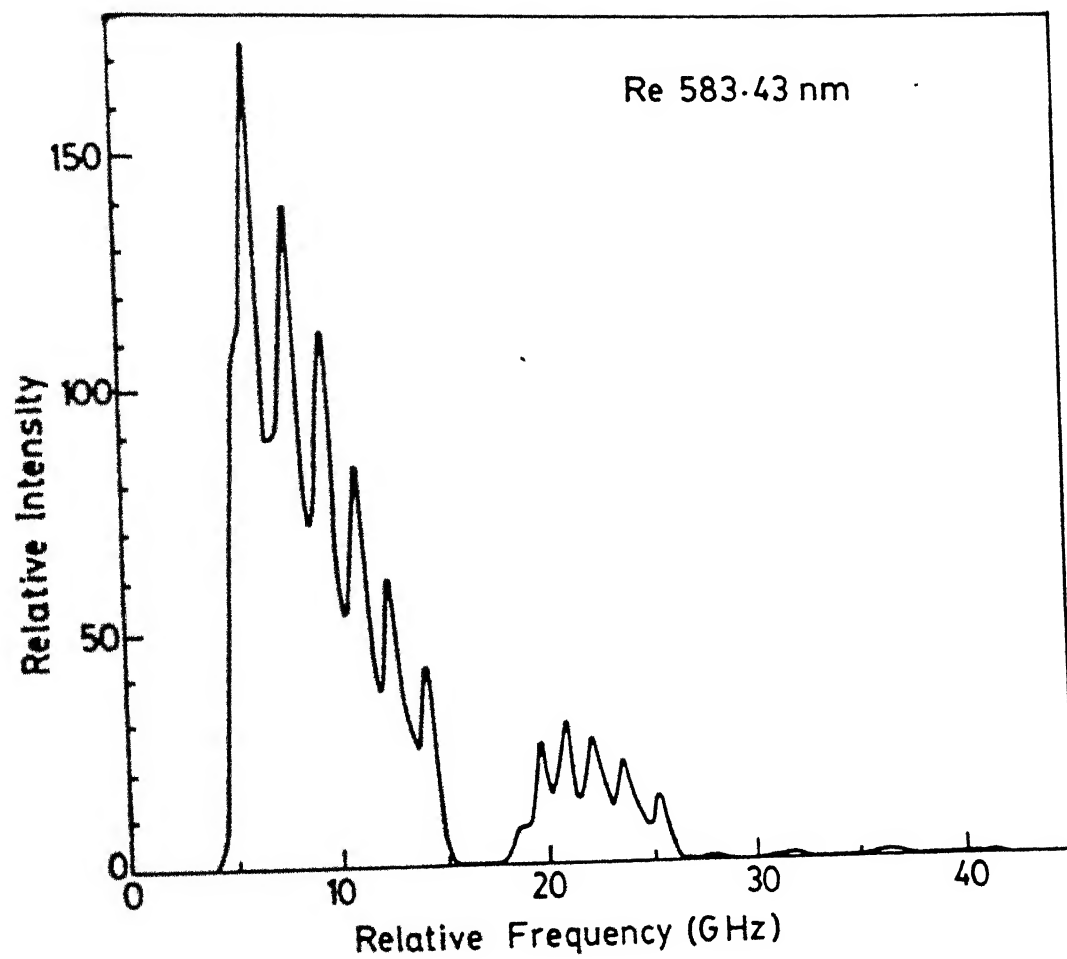


Fig. 38. Generated spectrum of rehenium transition at 583.43 nm.

583.43 nm. shown in Fig. 32(a), appear as two separate groups of peaks. The facts are that there is no other transition so close and the separation between the two group of peaks is more than the expected isotope shift. Therefore some of the components were identified by comparing their relative intensities, as given by eqns. 13 and 14, and used to calculate the isotope shift and the A's and B's for both the levels involved for both the isotopes. These constants were then used to generate the whole spectrum. The generated spectrum is shown in Fig. 36. Figure 36 shows that the two bunches belong to the same transition of both the isotopes. This grouping of peaks is a result of the large electric quadrupole moment of the nucleus and hence the large B constants. In addition, very weak components are expected on the higher frequency side of the spectrum. These weak components are not seen in the recorded spectrum because of their low intensity, of the order of the noise in the spectrum. Therefore during the analysis only this part of the spectrum was used. Our A and B constants agree with those given by Hohberg et al. [94] and hence we are justified in ignoring the spectrum on the higher frequency side.

Calculated hyperfine coupling constants, A and B, for eight levels of  $^{185}\text{Re}$  are given in Table VIII; known constants are also included for comparison. Table IX gives A and B constants for the same eight levels of  $^{187}\text{Re}$  along with already known constants, wherever applicable. It can be seen that agreement between our values and those of others is quite good. It was also

observed that the average linewidth of these spectral lines is 1000 MHz, which corresponds to an equilibrium atomic temperature 1100 K.

In conclusion, isotope shifts between  $^{185}\text{Re}$  and  $^{187}\text{Re}$ , in six transitions are reported. Hyperfine coupling constants, A and B, for eight levels belonging to the configurations of both the isotopes are reported.

TABLE VII

Rhenium transitions for which hyperfine structure and isotope shift has been studied

Sr. No.	Wavelength (nm)	Lower level	Upper Level	I.S. (MHz)	
				Ours	Others'
1	566.78	$a^6D_{5/2}$	$z^6D_{5/2}^o$	307.5	-
2	575.29	$a^4P_{5/2}$	$z^6P_{3/2}^o$	-1481	-
3	577.68	$a^4P_{5/2}$	$z^6P_{7/2}^o$	1504.0	1519
4	583.43	$a^6D_{9/2}$	$z^6P_{7/2}^o$	872.1	882
5	594.32	$a^6D_{5/2}$	$z^6D_{3/2}^o$	440	16
6	614.68	$a^6D_{3/2}$	$z^6D_{3/2}^o$	1205.7	1230

TABLE VIII

Calculated A and B Constants for various levels of  $^{185}\text{Re}$ .

Sr. No.	Level	Our Values		Others' Values	
		A(MHz)	B(MHz)	A(MHz)	B(MHz)
1	$a^6D_{5/2}$	1073.5	36.8	1072.2	20.1
2	$a^4P_{5/2}$	902.5	1738		
3	$a^6D_{9/2}$	2588.3	2415.1	2584.7	2370.4
4	$a^6D_{3/2}$	1462.9	-590.4	1456.4	-561.3
5.	$z^6D^o_{5/2}$	1256.98	635.14	1262.8	636.2
6	$z^6P^o_{3/2}$	3957.58	500.0		
7	$z^6P^o_{7/2}$	2855.4	1145.9	2819.7	1051.8
8	$z^6D^o_{3/2}$	23.5	960.5	18.3	954.8



TABLE IX

Calculated A and B parameters for various levels of  $^{187}\text{Re}$ .

Sr. No.	Level	Our Values		Others' values	
		A(MHz)	B(MHz)	A(MHz)	B(MHz)
1	$a^6D_{5/2}$	1091.7	15.6	1083.6	21.6
2	$a^4P_{5/2}$	896.5	1750		
3	$a^6D_{9/2}$	2637.2	2231.2	2611.2	2251.7
4	$a^6D_{3/2}$	1493.8	-510.8	1470.3	-531.1
5	$z^6D^o_{5/2}$	1283.4	579.9	1275.1	600.7
6	$z^6P^o_{3/2}$	4027.8	500.0		
7	$z^6P^o_{7/2}$	2885.4	915.0	2848.2	1001.8
8	$z^6D^o_{3/2}$	28.8	985.5	18.8	905.1

## CONCLUSIONS

Fine and hyperfine structure of scandium, niobium and rhenium has been studied using laser optogalvanic spectroscopy in the range 560 - 630 nm. Hyperfine structure parameters for large number of levels of these three elements are reported.

Seventeen fine structure transitions of scandium were identified out of which hyperfine structure of seven transition is studied and constants for twelve levels in the configurations  $3d^24s$  and  $3d^24p$  are reported.

Forty two fine structure transitions of niobium have been identified out of which hfs of 20 transitions is studied. Hfs parameters for 36 levels in the configurations  $4d^35s^2$ ,  $4d^45s$ ,  $4d^5$ ,  $4d^35s5p$ ,  $4d^45p$  are reported.

High resolution optogalvanic spectra of six transitions of rhenium has been recorded and isotope shift ( $^{187}\text{Re} - ^{185}\text{Re}$ ) in these six transitions is reported. Hfs parameters of eight levels in the configuration  $5d^56s^2$ ,  $5d^66s$ ,  $5d^56s6p$  and  $5d^46s^26p$ , of both the natural isotopes of rhenium are reported.

In addition equilibrium atomic temperature in the discharge is estimated from the measured Doppler width of the spectral line of these elements.

Wherever possible our results are compared with the data available in literature. Most of the levels reported here are either high lying metastable states or higher odd parity states, where very little information is available. The results presented in the thesis add to the existing results on hfs parameters for levels of scandium, niobium and rhenium. It is hoped that these results will be useful in the further theoretical analysis using effective operator formalism, for which one needs A and B parameters in as many states as possible. This will help in understanding these atoms better.

## REFERENCES

1. Demtroder W., in 'Topics in Chemistry', vol 17, Springer-Verlag, Berlin and New York (1971).
2. Demtröder W., Phys. Rep., 7, 223 (1973)
3. Lange W., Luther J. and Steudel A., "Dye Lasers in Spectroscopy", in Adv. in At. and Mol. Phys., Vol 10, (1974).
4. Mooradian A., Jaeger T. and Stokseth P., (eds.), Proc. Of the Int. Conf. on Tunable Lasers and applications, Springer Series in Optical Sciences Vol. 3 (1976)
5. Hall J.L. and Carlsten J.L. (eds.), 'Laser Spectroscopy III', Proc. of 3rd Int. Conf., Jackson Lake, 1977, Springer series in Optical sciences; Vol 7.
6. Walther H. and Rothe K.W. (eds.) 'Laser Spectroscopy IV', Proc. of 4th Int. Conf., Tegernsee 1979, Springer series in Optical Sciences Vol 21.
7. Demtröder W., 'Laser Spectroscopy', Springer Series in Chemical Physics Vol 5 (1981)
8. Michelson A., Phil. Mag. 31, 338 (1891)
9. Fabry C. and Perot A., Ann. Chem. et Phys., 12, 459 (1897)
10. Lummer O. and Gehrcke E., Ann. Phys., 10, 457 (1903)
11. Jager de C.W., Vries de H. and Vries de C., At. Data and Nuc. Data Tables, 14, 479 (1974).
12. Armstrong L., Jr., 'Theory of Hyperfine Structure in Free Atoms', Wiley - Interscience, New York (1971).
13. Lindgren I. and Rosen A.  
Case studies in Atomic Physics, IV, 97 - 298 (1974)
14. Popescu I.I., Optogalvanic Spectroscopy, in Proc. europophys. conf. on tracts in Quantum Electronics, Bucharest (1985) 391
15. Goldsmith J.E.M. and Lawler J.F., Contemp. Phys. 22, 235 (1981)
16. Hannaford P., Contemp. Phys. 24, 251 (1983)
17. Megges W.F. and Russell H.N., NBS J. Res. 17, 125 (1936)
18. Behran H.-O. and Guthohrlein G.H., J. de Physique C7-44, 149 (1983)

19. Govindarajan J. and Pramila T., J. Opt. Soc. Am. B6, 1275 (1989)
20. Fricke G., Bengtsson C., Hanstorp D., Nyberg A. and Persson J., Z. Phys., D8, 171 (1988)
21. Ranjit Singh and G.N. Rao, Phys. Scr., 40, 170 (1989)
22. Lederer C.M., Hollander J.M. and Perlman I., (eds.), 'Tables of Isotopes', 6th edn., John Wiley, NY (1968)
23. Moore C.E., 'Atomic Energy Levels, Vol I', Nat. Bur. Std., Washington D.C. USA (1971)
24. Fricke G., Kopfermann H., Penselin S. and Schlupmann Z. Physik, 148, 416 (1959)
25. Childs W.J. Phys. Rev. A4, 1767 (1971)
26. Bauche-Arnoult C.  
Proc. Roy. Soc. (London) A322, 361 (1971)
27. Gebauer H., Aldenhoven R. and Aydin R.  
Phys. Lett. 51A, 417 (1975)
28. Zeiske W., Meisel G., Gebauer H., Hofer B. and Ertmer W.  
Phys. Lett. 55A, 405 (1976)
29. Ertmer W. and Hofer B., Z. Phys. A276, 9 (1976)
30. Ranjit Singh, G.N. Rao and R.K. Thareja, "Laser Optogalvanic Spectroscopy of Sc I : Hyperfine Structure Studies"  
Submitted
31. Lederer, C.M. and Shirley, V.S., 'Tables of Isotopes', 7th. edn. Wiley, New York (1978)
32. Buttgenbach, S. and Dicke, R., Z. Phys., A275, 197 (1975)
33. Pendlebury J.M., Ring D.B. and Smith K.F., In, "La Structure Hyperfine Magnétique des Atoms et des Molecules", Eds. Lefebvre R. and Moser C., C.N.R.S., Paris (1967) p71.
34. Buttgenbach S., Meisel G., Penselin S. and Schneider K.H.  
Z. Phys. 230, 329 (1970)
35. Ranjit Singh and Rao G.N., "Hyperfine Structure of  $^{93}\text{Nb}$ ",  
Presented in Eleventh Int. Conf. on Atomic Physics, Paris, 4-7 July 1988.
36. Ranjit Singh and G.N. Rao, "Hyperfine Structure Studies of  $^{93}\text{Nb}$  Using Laser Optogalvanic Spectroscopy" submitted

37. Ranjit Singh, G.N. Rao and R.K. Thareja, "Laser Optogalvanic Spectroscopy of Nb I : Hyperfine Structure Studies"  
Submitted
38. Ranjit Singh, G.N. Rao and R.K. Thareja, "Hyperfine Structure and Isotope Shift Studies of Rhenium By Laser Optogalvanic Spectroscopy" submitted
39. Pauli, W., Naturwissenschaften, 12, 74 (1924)
40. Schuler, M., and Schmidt, T., Z. Phys., 94, 457 (1935)
41. Casimir, H.B.G., 'On the Interaction Between Atomic Nuclei and Electrons', Teyler's Tweede Genootschop, Haarlem, 1936; W.H. Freeman, San Francisco 1963.
42. Schwartz, C., Phys. Rev., 97, 380 (1955)
43. Sanders, P.G.H., and Beck, J., Proc. Roy. Soc. (London), A289, 97 (1965)
44. Childs W.J.  
Case studies in atomic collision Physics, III, 215 (1973)
45. Olsson G. and Rosén, A. Phys. Rev., A25, 658 (1982)
46. Buttgenbach, S., "Hyperfine Structure Of 4d- and 5d-elements" Springer Verlag, (1984).
47. White H E., 'Atomic Spectra', McGraw Hill, NY (1934)
48. Candler, C., 'Atomic Spectra and the Vector Model, 2nd. edn . D. Van Norstrand comp. Inc. (1964)
49. Kopfermann, H., 'Nuclear Moments', Academic Press Inc. New York (1958)
50. Cowan R. D., "The Theory of Atomic Structure and Spectra (University of California Press, 1981)
51. Bordarier Y., Judd B.R. and Klapisch M., Proc. Roy. Soc. Lon., A289, 81 (1965)
52. Schuler H. and Leyston J.E., Z. Phys., 70, 1 (1931)
53. Rosenthal J. and Breit G., Phys. Rev., 41, 459 (1932)
54. Heilig, K., and Steudel, A., Atom. Data and Nucl. data Tables, 14, 613 (1974)
55. King, W.H., 'Isotope Shifts in Atomic Spectra' New York, Plenum Press, (1984)
56. Babushkin, F.A., Sov. Phys. JETP, 17, 1118 (1963)

57. Camus P.J. (ed.), "International Colloquium on Optogalvanic Spectroscopy and its Applications", J. de Physique (Paris) 44-C7, (1983)
58. Joshi, M.M., Nature, 154, 147 (1944)
59. Foote, P.D. and Mohler, F.L., Phys. Rev., 26, 195 (1925)
60. Penning, F.M., Physica, 8, 137 (1928)
61. Penning, F.M., Z. Phys., 46, 355 (1928)
62. Kenty, C., Phys. Rev., 80, 95 (1950)
63. Meissner, K.W., and Miller, W.F., Phys. Rev., 92, 896 (1953)
64. Venkateshwarlu, V. and Ramiah, N.A., J. Opt. Soc. Japan, 9, 225 (1954)
65. Badarau, E., Popescu, I., Ghita, C. and Brit, J., Appl. Phys., 15, 1171 (1964)
66. Green, R.B., Keller, R.A., Luther, G.G., Schank, R.K. and Travis, J.J. Appl. Phys. Lett., 29, 727 (1976)
67. Rao, G.N., Govindarajan, J. and Reddy, M.N., Hyp. Int., 28, 539 (1987)
68. Smyth, K.C. and Schenck, P.K., Chem. Phys. Lett., 55, 466 (1978)
69. Pepper, D.M., IEEE. J. G. Electronics, QE-14, 971 (1978)
70. Eraz, G., Lewis, S. and Miron, E., IEEE. J. G. Electronics, QE-15, 1328 (1979)
71. Rolf, Engleman, Jr, Richard, A., Keller, and Charles, M. Miller, "Effect of Optical Saturation on Hyperfine Intensities in Optogalvanic Spectroscopy" J. Opt. Soc. Am., B2, 897 (1985)
72. Meggers W.F.  
Sci. Papers, Bur. Std., 22, 61 (1927)
73. Russell H.N., and Meggers, W.F.,  
Sci. Papers, Bur. Std., 22, 329 (1927)
74. Garton W.R.S., Tomkins F.S. and Ertol, B.  
Proc. Roy. Soc. London, A333, 1-16 (1973)
75. Neufeld Lorin and Schrenck W.G.  
Spectrochimica Acta, 3017, 45-53 (1975)
76. Ben Ahmed Z. and Verges J., Physica, 92-c, 113-121 (1977)
77. Ben Ahmed Z., Physica, 92-c, 122 (1977)

78. Raman G., Phys. Rev. 62, 523 (1942)
79. Roth C., J. Res., NBS, 73A, 497 (1969)
80. Meggers W.F., Corliss C.H., and Scribner B.F.  
Tables of Spectral Line Intensities arranged by elements'  
NBS Monograph 145 (U.S. Govt. Printing Press, Wash. D.C.  
(75))
81. Meggers, W.F., J. Wash. Acad. Sci. 14, 442 (1924)
82. Meggers, W.F. and Kiess, C.C., J. Opt. Soc. Am., 12, 432  
(1926)
83. King, A.S., Astrophys. J., 73, 441 (1931)
84. Meggers, W.F. and King, A.S., NBS J. Res. 16, (1936)
85. Meggers, W.F. and Scribner, NBS J. Res. 14, 629 (1935)
86. Harrisson, G.R. and Bitter, F., Phys. Rev., 57, 15 (1940)
87. Humphreys, C.J. and Meggers, W.F., NBS J. Res., 17, 125  
(1956)
88. "The Nuclear Moments of Columbium From Hyperfine Structure"  
Ballard, S.S., Phys. Rev., 46, 806 (1934)
89. "Hyperfine Structure and Nuclear moments of Columbium"<sup>93</sup>  
Meeks, W.W. and Fisher, R.A., Phys. Rev., 72, 451 (1947)
90. Murakawa K., Phys. Rev., 98, 1285 (1955)
91. Murakawa K., J. Phys. Soc. Japan, 13, 101 (1958)
92. Buttgenbach, S., Dicke R., Gebauer H., Herschel M. and  
Meisel G., Z. Phys., A 275, 193 (1975)
93. Schlecht R. G., White M. B. and McColun D. W., Phys. Rev.  
138, B306 (1968)
94. Armstrong L. Jr. and Marrus R., Phys. Rev. 138, B310 (1965)
95. Hohberg G., Krebs K., Schulz B. and Winkler R.  
Z. Phys., 186, 380 (1965)
96. Buchholz B. Kronfeldt H.-D. and Winkler R.  
Physica, 96C, 297 (1979)
97. Buttgenbach S., Dicke R., Golz G. and Traber F.  
Z. Phys. 302A, 281 (1981)



8A 1011

98. Burger K.H., Bughardt B., Buttgenbach S., Harzer R.,  
Hoeffgen H., Meisel G. and Traber F.  
Z. Phys. 307A, 201 (1982)
99. Klinkenberg P.F.A., Meggers W.F., Velasco R. and Catalan  
M.A., J. Res. Nat. Bur. Std., 59, 319 (1957)

**A 112548**

PHY-1990-D-SIN-LAS

**RESERVE COLLECTION**